University of California
Santa Barbara

Exotic, Topological, and Many Body Localized Quantum Phase Transitions

A dissertation submitted in partial satisfaction
of the requirements for the degree

Doctor of Philosophy
in
Physics

by

Kevin Jacob Slagle

Committee in charge:

Professor Cenke Xu, Chair
Professor Matthew Fisher
Professor David Weld

June 2016

The Dissertation of Kevin Jacob Slagle is approved.

Professor Matthew Fisher

Professor David Weld

Professor Cenke Xu, Committee Chair

June 2016

Acknowledgements

I am incredibly grateful to have had Cenke Xu as my PhD adviser. In my opinion, Cenke has been an ideal adviser and academic role model. I thoroughly enjoyed working with Cenke, and I hope I managed to absorb a fraction of his physical intuition.

I also owe great thanks to Yi-Zhuang You, who has been unbelievably helpful as a collaborator and teacher. Much of my physical understanding is the result of thorough explanations by Yi-Zhuang.

I thank Zhen Bi, Alex Rasmussen, Dominic Else, Brayden Ware, and many others for countless insightful discussions. Thank you Keith Fratus for organizing the many body journal club, which has resulted in many wonderful talks. I would also like to thank the rest of the condensed matter community at UCSB for making UCSB such an inspiring research institution.

I thank my undergraduate adviser, Anyes Taffard, for hiring me when I was a freshman, and providing me with fantastic research opportunities.

I also thank all of my friends for their support. In particular, thank you Carol Tsai for your patience and friendship. And thank you Maher Tahhan and Jay Logan for being great roommates.

And finally, I thank my family, and especially my parents, John and Gale, for their constant love and support.

Curriculum Vitæ

Kevin Jacob Slagle

Education

2016	Ph.D. in Physics (Expected), University of California, Santa Barbara.
2013	M.A. in Physics, University of California, Santa Barbara.
2011	B.S. in Physics, University of California, Irvine.
2011	B.S. in Mathematics, University of California, Irvine.

Publications

- Disordered XYZ Spin Chain Simulations using the Spectrum Bifurcation Renormalization Group
  - Kevin Slagle, Yi-Zhuang You, Cenke Xu
    arXiv:1604.1604.04283
- Many-Body Localization of Symmetry Protected Topological States
  - Kevin Slagle, Zhen Bi, Yi-Zhuang You, Cenke Xu
    arXiv:1505.05147
- Self-dual Quantum Electrodynamics on the boundary of 4d Bosonic Symmetry Protected Topological States
  - Zhen Bi, Kevin Slagle, Cenke Xu
    arXiv:1504.04373
- Exotic Quantum Phase Transitions of $(2+1)d$ Dirac Fermions
  - Kevin Slagle, Yi-Zhuang You, Cenke Xu
    Phys. Rev. B **91**, 115121 (2015)
- Classification and Description of Bosonic Symmetry Protected Topological Phases with Semiclassical Nonlinear Sigma models
  - Zhen Bi, Alex Rasmussen, Kevin Slagle, Cenke Xu
    Phys. Rev. B **91**, 134404 (2015)
- Quantum Phase Transition between the Z_2 Spin Liquid and Valence Bond Crystals on a Triangular Lattice
  - Kevin Slagle, Cenke Xu
    Phys. Rev. B **89**, 104418 (2014)
- Wave Function and Strange Correlator of Short-Range Entangled States
  - Yi-Zhuang You, Zhen Bi, Alex Rasmussen, Kevin Slagle, and Cenke Xu
    Phys. Rev. Lett. **112**, 247202 (2014)

Abstract

Exotic, Topological, and Many Body Localized Quantum Phase Transitions

by

Kevin Jacob Slagle

In this thesis we will study recent examples of exotic, topological, and many body localized quantum phase transitions. In Chapter 2 we study the quantum phase transition between the Z_2 spin liquid and valence bond solid (VBS) orders on a triangular lattice. We find a possible nematic Z_2 spin liquid intermediate phase and predict a continuous $3d$ XY* transition to the neighboring columnar and resonating-plaquette VBS phases. In Chapter 3 we demonstrate that an extended Kane-Mele Hubbard model on a bilayer honeycomb lattice has two novel quantum phase transitions. The first is a quantum phase transition between the weakly interacting gapless Dirac fermion phase and a strongly interacting fully gapped and symmetric trivial phase, which cannot be described by the standard Gross-Neveu model. The second is a quantum critical point between a quantum spin Hall insulator with spin S^z conservation and the previously mentioned strongly interacting fully gapped phase. We argue that the first quantum phase transition is related to the $\mathbb{Z}_{16}$ classification of the topological superconductor ^{3}He-B phase with interactions, while the second quantum phase transition is a topological phase transition described by a bosonic $O(4)$ nonlinear sigma model field theory with a Θ-term. In Chapter 4 we propose that if the highest and lowest energy eigenstates of a Hamiltonian belong to different SPT phases, then this Hamiltonian can't be fully many body localized. In Chapter 5 we study the disordered XYZ spin chain and its marginally many body localized critical lines, which we find to be characterized by an effective central charge $c' = \ln 2$ and continuously varying critical exponents.

Contents

Chapter 1

Introduction

Condensed matter physics involves the study of matter that is sufficiently condensed (e.g. liquids or solids) such that quantum mechanics plays an important role. The microscopic degrees of freedom (e.g. electrons) of condensed matter interact with each other and result in profoundly different emergent physics at macroscopic length scales. (E.g. Liquid water and solid ice bare little resemblance to their molecular components H_2O.) Remarkably, it turns out that distinct microscopic degrees of freedom can result in very similar macroscopic physics. (E.g. water (H_2O) and ethanol (C_2H_6O) molecules can both form liquids, and both copper and silver can be metallic.)

An important problem in theoretical condensed matter is to classify all possible kinds of emergent macroscopic physics, which are known as phases of matter (e.g. solid or liquid, metal or insulator). Another important problem is the study of the phase transitions between different phases of matter. It is again remarkable that the phase transitions also exhibit universal physics. In this thesis, we will study examples of new and exotic phase transitions where quantum mechanics, topology, and many body localization play important roles.

1.1 Spontaneous Symmetry Breaking

1.1.1 Landau Theory

Landau theory describes phases and phase transitions that result from spontaneous symmetry breaking. [1] In Landau theory, the long range physics of a system with a symmetry is described by an effective Lagrangian $\mathcal{L}$ written in terms of an order parameter ϕ (e.g. average magnetic field) which transforms non-trivially under the symmetry.

For the case of a Z_2 symmetry, $\phi \to -\phi$ and the most relevant terms in the effective Lagrangian can be written as

$$\mathcal{L} = \int_x (\partial\phi)^2 + \underbrace{r\phi^2 + g\phi^4 + v\phi^6}_{V(\phi)} + \cdots \tag{1.1}$$

where $\phi(x)$ is a real valued function. The physics of the above Lagrangian can be understood from the potential $V(\phi)$. If $V(\phi)$ has its minimum at $\phi = 0$, then $r > 0$; the Z_2 symmetry is not broken; and the system is in the trivial phase. If $r < 0$, then there are minima at $\phi = \pm\phi_0$ and the system spontaneously breaks the Z_2 symmetry.

If we take $g > 0$ and $v = 0$, and consider decreasing r from $r > 0$ to $r < 0$, then there will be a phase transition (at $r = 0$) from the trivial phase ($r > 0$) to the ordered (symmetry breaking) phase ($r < 0$). When $r < 0$, the minima of $V(\phi)$ will be at $\phi \sim \pm r^\beta$ with critical exponent $\beta = 1/2$. However, this mean field description and calculation of critical exponents is only accurate when the number of dimensions is greater than or equal to the upper critical dimension, which is 4 in this case: $d \geq d_{uc} = 4$. Below the upper critical dimension, the full renormalization group and Landau-Ginzburg-Wilson theory must be applied for an accurate description [2, 3]. Since ϕ (and therefore also the free energy) changes continuously across the phase transition, the phase transition is a continuous (2nd order) phase transition. At the critical point ($r = 0$), the system exhibits critical behavior in the form of power-law decaying connected correlators and

long range mutual information.

If however we take $r > 0$ and $v > 0$, and consider decreasing g from $g = +\infty$ to $g = -\infty$, then there will be a discontinuous (first order) phase transition from the trivial phase to the ordered phase. This will occur at some critical $g = g_c < 0$ at which there are three global minima of $V(\phi)$: $\phi = 0, \pm\phi_0$. When $g > g_c$, $\phi = 0$ is the global minima, while $\phi = \pm\phi_0$ is the global minima when $g < g_c$. Thus, ϕ (and therefore also the free energy) changes discontinuously across the phase transition, and the phase transition is discontinuous. This phase transition will not show critical behavior, but can instead exhibit metastable states and hysteresis effects. (The steam $\leftrightarrow$ water $\leftrightarrow$ ice transitions are of this kind.)

1.1.2 Correlation Functions

The spontaneous symmetry breaking is often diagnosed using long range correlation functions of order parameters. For the Lagrangian described above, the expectation value $C(|x - x'|) = \langle\phi(x)\phi(x')\rangle$ can be measured. In the trivial phase, the correlator decays exponentially with distance $C(x) \sim e^{-x/a}$ (with a non-universal length scale a), which shows that the order parameter ϕ has no long range correlations. In the symmetry breaking phase, the correlator asymptotes to a constant $C(x) \sim 1$. In the critical phase in the case of a continuous phase transition, the correlator shows long range correlations with a power-law decay $C(|x - x'|) \sim x^{-d+2-\eta}$ for some universal critical exponent η (in d spacetime dimensions).

1.1.3 Long Range Mutual Information

However, for some systems trying to determine which order parameter to investigate can be difficult. Additionally, it can also be difficult to prove that a system breaks no

symmetry since checking all order parameters can be very tedious. Ideally, one could measure a single observable to check if any symmetry is broken. This can be done using long range mutual information (LRMI) [4].

The mutual information between two non-overlapping subsystems A and B is defined to be $\mathcal{I}(A,B) \equiv S_E(A) + S_E(B) - S_E(A \cup B)$ where $S_E(A) \equiv -\operatorname{Tr} \rho_A \ln \rho_A$ is the entanglement entropy of the subsystem A, and ρ_A is the reduced density matrix of a subsystem A. For a system described by a Hamiltonian, the reduced density matrix can be calculated from the density matrix ρ by tracing out degrees of freedom not in the subsystem A: $\rho_A \equiv \operatorname{Tr}_{\overline{A}} \rho$. An inverse temperature β, the density matrix is $\rho = Z^{-1} e^{-\beta H}$ where $Z \equiv e^{-\beta H}$. Note that for a system at zero temperature with multiple degenerate ground states $|\psi_n\rangle$, ρ includes all of the ground states: $\rho = N^{-1} \sum_{n=1}^{N} |\psi_n\rangle \langle\psi_n|$.

Let $\mathcal{I}(x)$ be the long range mutual information (LRMI) between two subsystems of constant shape and size separated by a distance x. Then in a trivial phase the LRMI decays exponentially $\mathcal{I}(x) \sim e^{-x/a}$ (for some non-universal length scale a). Furthermore, $\mathcal{I}(x) \sim e^{-x/a}$ implies that there is no spontaneous symmetry breaking of any kind. In the symmetry breaking phase, the LRMI must asymptote to a constant $\mathcal{I}(x) \sim 1$ since mutual information can be used to compute a an upper bound for connected correlation functions. In the critical phase in the case of a continuous phase transition, the LRMI decays according to a power law $\mathcal{I}(x) \sim x^{-d+2-\eta'}$ which we later exemplify in Fig. 5.7.

1.2 Topological Order and Deconfined Criticality

In the previous section, we reviewed how Landau theory can describe spontaneous symmetry breaking phases and the phase transitions between such phases. However, not all phases can be fully understood in terms of spontaneous symmetry breaking. Furthermore, it is also possible for a phase transition between symmetry breaking phases

to fall outside of the Landau-Ginzburg-Wilson (LGW) paradigm.

1.2.1 U(1) Gauge Theory

An example of a phase beyond spontaneous symmetry breaking is a deconfined or topological phase. The simplest example of such a phase is a $U(1)$ gauge theory

$$\mathcal{L} = \int_x g^{-1} F_{\mu\nu}^2 \quad \text{where} \quad F_{\mu\nu} \equiv \partial_\mu A_\nu - \partial_\nu A_\mu \tag{1.2}$$

where A_μ is a real valued function (or technically a connection form). (This field theory also describes electromagnetism and $U(1)$ spin liquids [5].) This phase has long range power-law correlations and therefore also power-law long range mutual information. The phase also has a certain kind of topological order [6] which can also be observed through long range mutual information [4]. This theory has a local $U(1)$ symmetry; however the phase (with interactions) is stable to arbitrary perturbations, even those that break the local $U(1)$ symmetry [6]. If the gauge field A is compact (so that $e^{\mathrm{i}\oint A}$ is observable while $\oint A$ is not), then monopole configurations of A are allowed (e.g. $A = \frac{1}{2}\cos\theta \mathrm{d}\phi$) and the above Lagrangian also exhibits a trivial confined phase when g is large. The deconfined (small g) to confined (large g) phase transition is an example of a phase transition beyond LGW.

1.2.2 Z_2 Gauge Theory

Another phase beyond the Landau paradigm is the Z_2 gauge theory, which describes Z_2 spin liquids. This phase can be described using the following lattice Hamiltonian:

$$H = \sum_{p=\square} \prod_{\ell \in p} \sigma_\ell^z + \sum_{i=+} \prod_{\ell \in i} \sigma_\ell^x \tag{1.3}$$

where the Pauli matrices σ live on the links of a square lattice. The first term is a sum over plaquettes p of products of σ^z operators around the edges of p; the second term is a

sum over sites i of products of σ^x operators on the links neighboring the site i. This model has Z_2 topological order and has very important applications to quantum computation in the form of the surface code quantum error correction scheme [7]. The field theory for this model can be obtained from Eq. 1.2 by condensing matter with charge 2.

Because this model has no explicit local Z_2 gauge symmetry, it is very difficult to detect the topological order using correlation functions when interactions are present. This is because the naive Wilson loop composed of σ^z or σ^x operators obeys an area law in both the confined and topological phase. If there is an explicit local gauge symmetry can one easily write down a Wilson loop operator that decays according to a perimeter law in the deconfined phase. However, without an explicit local gauge symmetry, one would have to determine an "ideal" Wilson loop that corresponds to the emergent local symmetry, which is difficult.

Long range mutual information (LRMI) is again a useful alternative to correlations functions. To detect topological order, one can consider the LRMI $\mathcal{I}(x)$ between two noncontractible subsystems (of constant size and shape) separated by a distance x. In the trivial phase the LRMI decays exponentially while in the deconfined phase the LRMI asymptotes to a constant. This behavior can be understood for the case when the two subsystems are noncontractible loops. The perimeter of these loops is constant while the area enclosed by them is proportional to their separation x (since the loops are of constant size and shape). Now recall that the LRMI is an upper bound for all connected correlation functions, including the correlation function of an "ideal" Wilson loop operator (discussed in previous paragraph) along the two subregions. This "ideal" WIlson loop decays according to a perimeter (area) law in the deconfined (confined) phase. Therefore the LRMI satisfies the "area" and "perimeter" laws which correspond to exponential and power-law decaying LRMI.

1.2.3 Critical Phenomena

A phase transition can be beyond LGW even if the two neighboring phases are symmetry breaking phases. This is the case in deconfined criticality [8, 9], for which the phase transition between a ($O(3)$ symmetry breaking) Néel antiferromagnet to a (Z_4 square lattice rotation symmetry breaking) valence bold solid (VBS) was originally studied. Since neither broken symmetry is a subgroup of the other, LGW predicts that this phase transition must be first order (assuming no fine tuning or intermediate phase transitions). However, numerical evidence shows that the transition is continuous [10, 11]. The physics of the phase transitions between the Néel antiferromagnet, VBS, Z_2 spin liquid, and a spiral order can be understood using a mutual Chern-Simons theory [12, 13]. In Chapter 2 we study in detail the quantum phase transition between the Z_2 spin liquid and valence bond solid on a triangular lattice. We find a possible nematic Z_2 spin liquid intermediate phase [1] and predict a continuous $3d$ XY* transition to the neighboring columnar and resonating-plaquette VBS phases.

1.3 Symmetry Protected Topological Order

A new recently discovered class of phases is the symmetry protected topological (SPT) order [15], which generalize topological insulators and topological superconductors. SPT phases are trivial in the absence of symmetry. However, when protected by a symmetry, SPT phases are characterized by a short range entangled bulk and a boundary that is anomalous (when the symmetry in imposed) [16]. That is, a d dimensional SPT with symmetry G has a $d-1$ dimensional boundary which can not exist on a $d-1$ dimensional lattice with symmetry G. A number of methods have been used to classify SPT phases, including group cohomology [17, 18], Chern-Simons theory [19], nonlinear

[1] See [14] for possible recent DMRG numerical evidence for a nematic spin liquid.

sigma models [20], cobordisms [21], and anomalous symmetry action on the edge [16].

The classification of SPTs using nonlinear sigma models [20] is particularly convenient when phase transitions are of interest since it makes use of a well-understood field theory. The Lagrangians considered are of the form

$$S[\vec{n}] = g^{-1}\int_x (\partial_\mu \vec{n})^2 + S_{\text{top}}[\vec{n}] + \cdots \tag{1.4}$$

$$S_{\text{top}}[\vec{n}] = \frac{\mathrm{i}\Theta}{\Omega_d}\int n^*\omega \tag{1.5}$$

$$= \begin{cases} \frac{\mathrm{i}\Theta}{\Omega_2}\int_{\tau,x} \epsilon_{abc} n^a \partial_\tau n^b \partial_x n^c & d = 1+1 \\ \frac{\mathrm{i}\Theta}{\Omega_3}\int_{\tau,x,y} \epsilon_{abcd} n^a \partial_\tau n^b \partial_x n^c \partial_y n^d & d = 2+1 \end{cases} \tag{1.6}$$

where $\vec{n}(x)$ is a $d+1$ component field in d spacetime dimensions. $(\partial_\mu \vec{n})^2$ restricts $\vec{n}$ to smooth configurations and the topological Θ-term $S_{\text{top}}[\vec{n}] \in \mathrm{i}\Theta\mathbb{Z}$ is an integer multiple of $\mathrm{i}\Theta$ and depends only on the topology of $\vec{n}$. More precisely, $\frac{1}{\mathrm{i}\Theta} S_{\text{top}}[\vec{n}] \in \mathbb{Z}$ counts the number of times $\vec{n}$ wraps around the d-sphere. This can be calculated via the pullback (n^*) of the volume form (ω) of the d-sphere by the field (n) (Eq. 1.5), and expanded using Cartesian coordinates as in (1.6). $\Omega_d = \int \omega$ is the volume of a d-sphere. The "$\cdots$" in Eq. 1.4 denote extra terms that can be added to reduce the onsite symmetry from $O(d+1)$ to a subgroup of $O(d+1)$.

When g is small and the number of spacetime dimensions is $d \geq 3$, there will be spontaneous symmetry breaking and the topological term will not play a role [22]. If there is no symmetry breaking (large g) and $\Theta = 0$, then the system is in the trivial phase. If $\Theta = 2\pi$ (and g is large), then the topological term will be an integer multiple of $2\pi\mathrm{i}$ so that $e^{S_{\text{top}}[\vec{n}]} = 1$, which makes the role of the topological term subtle. If no symmetry is enforced, then $\Theta = 2\pi$ is in the same phase as $\Theta = \pi$. However, with certain symmetries and spacetime dimensions d, $\Theta = 2\pi$ can be in a nontrivial symmetry protected topological phase. When $\Theta = \pi$ (and g is large), then the system can be in a

critical phase.

In Chapter 3 we use determinant quantum Monte Carlo simulations to study an extended Kane-Mele Hubbard model on a bilayer honeycomb lattice. This model hosts a quantum spin hall (QSH) SPT phase. We show that the phase transition between the QSH to the trivial phase is naturally described by a nonlinear sigma model with a topological Θ-term (Eq. 1.4). We also show that this model hosts a new exotic quantum phase transition between a weakly interacting gapless Dirac fermion phase and a strongly interacting fully gapped and symmetric trivial phase. This phase transition can not be described using LGW theory nor the standard Gross-Neveu model.

1.4 Many Body Localization

It has recently been discovered that in the presence of strong disorder an interacting system that isn't coupled to a heat bath can fail to thermalize [23]. That is, such a quantum system will not reach thermal equilibrium, and is therefore said to be many body localized (MBL).

More precisely, an MBL system does not satisfy the eigenstate thermalization hypothesis (ETH) [24], which attempts to explain and make precise the notion of thermalization. In a nutshell, a system is thermal and satisfies ETH if for any initial state $|\psi\rangle$, all local observables approach their thermal expectation values

$$\rho_A(t) \simeq \rho_A(\beta) \tag{1.7}$$

$$\text{where} \quad \rho_A(t) \equiv \mathrm{Tr}_{\overline{A}} |\psi(t)\rangle \langle\psi(t)|$$

$$\rho_A(\beta) \equiv \mathrm{Tr}_{\overline{A}}\, \rho(\beta)$$

$$\rho(\beta) \equiv \frac{e^{-\beta H}}{\mathrm{Tr}\, e^{-\beta H}}$$

$$\langle\psi|H|\psi\rangle = \mathrm{Tr}\, H\rho(\beta) \tag{1.8}$$

after a large time t and for large system sizes. $\rho_A(t)$ is the reduced density matrix of the time evolved state $|\psi(t)\rangle$ over a finite subsystem A. $\rho_A(\beta)$ is the reduced thermal density matrix over the same subsystem A evaluated at the inverse temperature β which corresponds to the thermal energy of $|\psi\rangle$ (Eq. 1.8).

A Hamiltonian is said to be fully many body localized (MBL) if all eigenstates in the many-body spectrum are localized [25] and therefore violate ETH (Eq. 1.7). It is believed that any fully MBL Hamiltonian H can be diagonalized by some finite local unitary transformation U:

$$\begin{aligned} H_{\text{eff}} &= UHU^\dagger \\ &= \sum_i h_i^{(1)} \tau_i^z + \sum_{ij} h_{ij}^{(2)} \tau_i^z \tau_j^z + \sum_{ijk} h_{ijk}^{(3)} \tau_i^z \tau_j^z \tau_k^z + \cdots \end{aligned} \tag{1.9}$$

where the τ_i^z are local integrals of motion (LIOM). The fact that U is a finite local unitary transformation means that U can be written as a finite time evolution of a time dependent local Hamiltonian with a bounded spectrum. This implies that the LIOM $U\tau_i^z U^\dagger$ must be local operators (with exponentially decaying tails). This implies that the eigenstates of an MBL Hamiltonian display an area law entanglement, as opposed to the volume law seen in excited states of thermal systems. Furthermore, the $h_{ijk\ldots}^{(n)}$ decay exponentially with n and distance $\max(|i-j|, |i-k|, |j-k|, \ldots)$. This implies that in an MBL system, the time evolution of a direct product state displays an entanglement entropy which increases only logarithmically with time [26, 27, 28], instead of linearly with time as in thermal systems. This implies that an MBL system can't efficiently spread entanglement, and thus can't act as its own heat bath.

In Chapter 4 we demonstrate a possible obstruction to making a system fully MBL. The obstruction occurs when the lowest and highest energy states of a Hamiltonian belong to different SPT phases. In this case, we find that there is a phase transition in the energy spectrum, at which the energy eigenstates are delocalized.

In Chapter 5 we study in detail the disordered XYZ spin chain and its marginally MBL critical phase, which is a kind of non-thermal critical phase that can occur at a phase transition between two MBL phases. A marginal MBL phase doesn't obey Eq. 1.9 with the same restrictions for the unitary transformation U and coefficients $h^{(n)}_{ijk\ldots}$. Marginal MBL phases instead show long range correlations, as demonstrated in Chapter 5. In the XYZ spin chain, we find critical lines which are characterized by an effective central charge $c' = \ln 2$ and continuously varying critical exponents.

Chapter 2

Quantum Phase Transitions between the Z_2 Spin Liquid and Valence Bond Solids

In this chapter we study the quantum phase transition between the Z_2 spin liquid and valence bond solid (VBS) orders on a triangular lattice. With a fully isotropic triangular lattice, the transition from a columnar or resonating-plaquette VBS order can be either first order or there could be two transitions with an intermediate phase. If the transition splits into two, then the Z_2 spin liquid will first experience a first order $q = 3$ Potts transition to a new nematic Z_2 spin liquid that breaks the $2\pi/3$ lattice rotation symmetry (but retain translation symmetry unlike the VBS states). The second transition will then take this new nematic Z_2 spin liquid to a columnar or resonating-plaquette VBS state through a second order $3d$ XY* transition. On a distorted triangular lattice, the degeneracy between some of the different columnar VBS orders is lifted, and the phase transition can reduce to a single $3d$ XY* transition.

2.1 Introduction

Tremendous progress has been made in the last two years in searching for spin liquid states in quantum frustrated spin models by various numerical methods [29, 30, 31, 32, 33]. Using the topological entanglement entropy [34, 35], the Z_2 topological liquid phase was identified in the phase diagram of frustrated spin and quantum boson models on the square lattice [30] and Kagome lattice [29, 31]. Although the Z_2 liquid phase itself does not break any symmetry, it was confirmed numerically that a Z_2 spin liquid phase can be very close in energy to a valence bond solid (VBS) state which breaks translation symmetry [29]. Thus it is conceivable that under weak perturbations the Z_2 spin liquid can be driven into a VBS phase. This liquid-VBS quantum phase transition is what we will discuss in the current chapter. In previous works, this liquid-VBS transition was thoroughly studied on the square lattice [36, 37], honeycomb lattice [37], and Kagome lattice [38]. The universality class of the liquid-VBS transition in general depends on the nature of the VBS pattern. On the square and honeycomb lattice, the quantum phase transitions between a Z_2 liquid and simple VBS phases such as the columnar, resonating-plaquette, and staggered VBS phases have all been well-understood [37, 39]. However, on the triangular lattice, starting from a Z_2 liquid phase, previous studies only obtained the transition into a $\sqrt{12} \times \sqrt{12}$ VBS pattern with a large unit cell [40, 41, 42, 43, 44] [1], while a direct transition between the Z_2 liquid and the simple columnar or resonating-plaquette VBS patterns was never understood in previous theoretical analysis. This is precisely the gap that we will fill in this paper.

We choose to study spin systems on the triangular lattice because the spin-1/2 organic materials with a triangular lattice are the best experimental candidates for a spin liquid [45, 46, 47, 48, 49, 50, 51, 52, 53, 54], and some of the organic materials in the same

[1] This VBS pattern has 12 sites in one unit cell on the triangular lattice [43]. However, in terms of the dual quantum Ising model on the honeycomb lattice, this pattern has 48 sites per unit cell [41].

family indeed have a columnar VBS order [55]. Our analysis predicts that on an isotropic triangular lattice, the Z_2 liquid to the 12-fold degenerate columnar/plaquette VBS order can be either first order or there could be two transitions with an intermediate phase (Fig. 2.5). The possibility of having either a single first order transition or two continuous transitions with an intermediate phase has been observed previously in Fe-pnictide materials [56, 57, 58, 59, 60]. In the case of two transitions, the Z_2 liquid first undergoes a first order $q = 3$ Potts transition to a new nematic Z_2 spin liquid which breaks the 120° lattice rotation symmetry. A second transition will then take this nematic Z_2 spin liquid to a columnar or plaquette VBS state through a $3d$ XY* transition. On a distorted triangular lattice, the VBS pattern becomes either 2-fold or 4-fold (depending on the details of the distortion), and the liquid-VBS transition can reduce to one single 3d XY* transition. All of these 3d XY* transitions should have a very large anomalous dimension of the VBS order parameter, which can be tested by future numerical simulations.

2.2 Model

Motivated by the recent discovery of the Z_2 spin liquid on the square and Kagome lattices, we expect that the same Z_2 spin liquid can be realized with a certain spin-1/2 Hamiltonian on the triangular lattice as well. In order to analyze a spin liquid, it is standard to introduce the slave particles: $\vec{S}_i = \frac{1}{2} f^\dagger_{i,\alpha} \vec{\sigma}_{\alpha\beta} f_{i,\beta}$ where $f_{i,\alpha}$ can be either a bosonic or fermionic spin-1/2 excitation, but either choice is subject to a local constraint, $\sum_\alpha f^\dagger_{i,\alpha} f_{i,\alpha} = n_i = 1$, in order to match the slave particle Hilbert space with the spin Hilbert space. This local constraint introduces a continuous gauge symmetry (U(1) for bosonic spinons and SU(2) for fermionic spinons), which at low energy can be broken down to a Z_2 gauge symmetry by the mean field state of $f_{i,\alpha}$. The low energy physics of this state is described by a pure Z_2 gauge field. In this paper we assume that the Z_2

spin liquid itself respects all symmetries of the lattice, which is possible on the triangular lattice [61].

In both the Z_2 spin liquid and VBS phases, the spin excitation $f_{i,\alpha}$ is fully gapped. Therefore we can "integrate out" the spin excitations and focus on the spin singlet channel of the system. The spin singlet channel of the system should be described by the standard Z_2 gauge theory on the triangular lattice:

$$H = \sum_{\triangle,\triangledown} -K \prod_{<ij>\in\triangle,\triangledown} \sigma_{ij}^z - \sum_{<ij>} h\sigma_{ij}^x + \cdots \tag{2.1}$$

where σ^z and σ^x are ordinary Pauli matrices and $< ij >$ denotes the *link* on the triangular lattice between sites i and j. $\sigma^x = -1$ roughly corresponds to a valence bond while $\sigma^x = +1$ indicates the absence of a bond. σ^z is therefore the operator that creates/annihilates a bond. The first term in Eq. 2.1 is a ring product of σ^z on every triangle plaquette on the lattice; we will keep $K > 0$ so that the Hamiltonian (Eq. 2.1) favors the ring product to be $+1$ on every plaquette. The ellipsis in Eq. 2.1 include all the terms that are allowed by the Z_2 gauge symmetry and lattice symmetry. In particular, we will add terms that are a product of σ^x operators along a string of neighboring links. The Hamiltonian Eq. 2.1 is invariant under the local Z_2 gauge transformation: $\sigma_{ij}^z \to \eta_i \sigma_{ij}^z \eta_j$ where $\eta_i = \pm 1$. The Hilbert space of this system is also subject to a local constraint, which is analogous to the familiar Gauss law constraint of an ordinary U(1) gauge field: $\vec{\nabla} \cdot \vec{E} = \sum_\alpha f_{i,\alpha}^\dagger f_{i,\alpha} = n_i = 1$. Once the U(1) gauge symmetry is broken down to Z_2, the gauge constraint reduces to

$$\prod_{j=1\cdots 6 \text{ around } i} \sigma_{ij}^x = (-1)^{n_i} = -1 \tag{2.2}$$

where $j = 1 \cdots 6$ are the six nearest neighbors of site i on the triangular lattice. Physically, this constraint forces each site to only share an odd number of bonds. In addition, $h > 0$ will favor only a single bond per site over three or five bonds. Together, the gauge

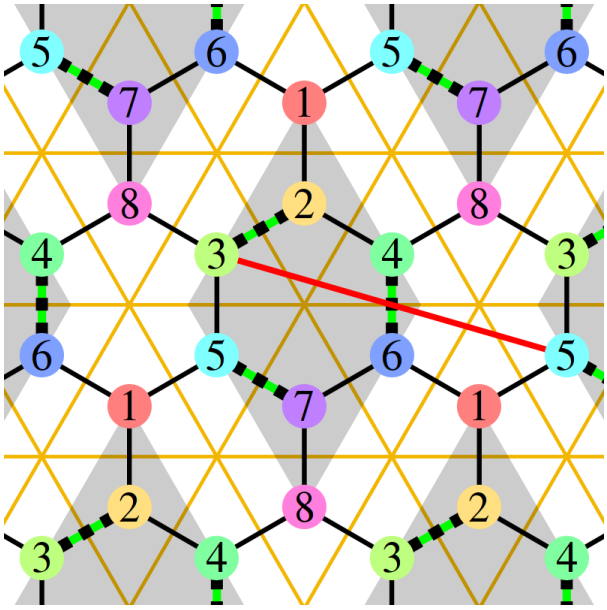

Figure 2.1: The dual honeycomb lattice on which Eq. 2.4 is defined. $\eta = 1$ on the solid black links, while $\eta = -1$ on the dashed green-black links. Every unit cell (gray diamond) has eight sites $1 \cdots 8$. In order to obtain the columnar VBS order, we consider the quantum Ising model defined on this honeycomb lattice with Ising couplings between sites up to 7th nearest-neighbor. (One pair of 7th neighbor sites is shown in red.)

constraint and $h > 0$ therefore roughly implement a "hard dimer constraint" (one site shares exactly one bond).

The VBS phase is a confined phase of the slave particle f_α; and in 2+1d Z_2 gauge theory, the confinement is driven by the condensation of vison excitations. A vison is a plaquette where $\prod \sigma^z = -1$. A vison is not a local excitation of σ^z and σ^x. Therefore, in order to describe its dynamics and hence its condensation using a Landau-Ginzburg-Wilson (LGW) framework, we need to go to the dual picture where the vison becomes a local excitation. In the dual language, quantities are defined on the triangular lattice

plaquettes, which form a honeycomb lattice (Fig. 2.1). The duality mapping is

$$\tau^x_{q=\triangle} = \prod_{<ij> \text{ around } \triangle} \sigma^z_{ij}$$

$$\sigma^x_{ij} = \eta_{pq}\tau^z_p\tau^z_q \quad \text{where } p,q \text{ share } < ij > \tag{2.3}$$

The dual Hamiltonian is a quantum Ising model on the honeycomb lattice:

$$H = \sum_{<p,q>} -K\tau^x_p - h\eta_{pq}\tau^z_p\tau^z_q + \cdots \tag{2.4}$$

Here p and q denote the sites of the dual honeycomb lattice (plaquettes of the triangular lattice). In this dual representation, τ^a are operators while $\eta_{pq} = \pm 1$ are pure numbers. τ^x_p is the vison density ($\tau^x_p = -1$ means there is one vison at the dual site p), and τ^z_p creates/annihilates a vison on the dual site p. The ellipsis in Eq. 2.4 can contain arbitrary further neighbor Ising couplings allowed by the PSG (described below).

Because of the constraint Eq. 2.2, η_{pq} must also satisfy a constraint: $\prod_{pq\in\text{hexagon}} \eta_{pq} = -1$, which makes the dual quantum Ising model a fully frustrated one. Here we choose $\eta_{pq} = -1$ on the dotted links in Fig. 2.1, while $\eta_{pq} = +1$ otherwise. The choice of η_{pq} we have made on the dual lattice is just a "gauge" choice, which apparently has to break the lattice symmetry; hence each unit cell on the dual lattice contains eight sites $(1 \cdots 8)$. Due to the reduced lattice symmetry in the dual theory, the correct lattice symmetry transformation for the dual vison τ^z must be combined with a nontrivial Z_2 gauge transformation of η_{pq} to recover the full symmetry of the original triangular lattice; this combined transformation is called the projective symmetry group (PSG) [62]. The dual quantum Ising model has to be invariant under the PSG.

The liquid-VBS phase transition corresponds to the Ising disorder-order phase transition in the dual Hamiltonian (Eq. 2.4), which is driven by the condensation of τ^z_p.

Because Eq. 2.4 is a fully frustrated quantum Ising model, τ^z can condense at nonzero momenta in the dual Brillouin zone (BZ). If Eq. 2.4 only has nearest neighbor hopping (which is the case studied in [41]), then there are four different minimum modes in the BZ (Fig. 2.2a), and the vison condensate corresponds to a $\sqrt{12} \times \sqrt{12}$ VBS pattern with a large unit cell [40, 41, 43]. The PSG guarantees that this liquid-VBS transition belongs to a $3d$ O(4)* universality class.

2.3 Landau-Ginzburg Analysis

Our goal is to study the quantum phase transition between the Z_2 liquid and the simple columnar/plaquette VBS order on the triangular lattice (Fig. 2.3). With nearest neighbor Ising couplings only, the dual Hamiltonian (Eq. 2.4) will not produce the columnar/plaquette VBS order. We have to turn on further neighbor couplings in Eq. 2.4 that are allowed by the PSG. We have thoroughly explored the possible phases of Eq. 2.4. A negative 2nd neighbor Ising coupling on the dual lattice will destabilize the original order in Fig. 2.2a at the cost of a ring degeneracy. This ring degeneracy is not broken until seventh neighbor couplings are added. With the seventh neighbor couplings, the minima of Eq. 2.4 are then stabilized by six different minimum modes (Fig. 2.2b) with momenta:

$$\vec{Q}_1 = \vec{Q}_2 = (\frac{\pi}{2\sqrt{3}}, \ -\frac{\pi}{6})$$

$$\vec{Q}_3 = \vec{Q}_4 = (\frac{\pi}{2\sqrt{3}}, \ +\frac{\pi}{6})$$

$$\vec{Q}_5 = \vec{Q}_6 = (0, \ \frac{\pi}{3}) \tag{2.5}$$

Each of these momenta correspond to two orthogonal modes; there are therefore six minimum modes. To analyze the low energy physics, we expand the Ising operator τ^z

about these six minimum modes:

$$\tau^z_{r,n} = \sum_{a=1}^{6} \psi_a(r) v_{a,n} e^{i\vec{Q}_a \cdot \vec{r}} \tag{2.6}$$

r takes on values at the center of the unit cell diamonds (Fig. 2.1) and $n = 1 \cdots 8$ denotes the eight sites in each unit cell. ψ_a with $a = 1 \cdots 6$ are the real fields corresponding to the six low energy modes and will play the role of our order parameters. The eight component vectors $v_{a,n}$ (given in Appendix 2.A) are the wave functions of τ^z_n at each momentum $\vec{Q}_a$. The action of the PSG on $\tau^z_{a,n}$ will induce the action of the PSG on $\psi_a(r)$. ψ_a will therefore carry a six dimensional representation of the PSG which will enable us to calculate the lowest order symmetry allowed Lagrangian.

The PSG is generated by the following transformations (assume the lattice constant of the original triangular lattice is $\sqrt{3}$):

$$\begin{aligned}
T_1 &: \quad x \to x + \sqrt{3}, && \psi_a \to T_{1,ab}\psi_b \\
T_2 &: \quad x \to x + \tfrac{\sqrt{3}}{2},\ y \to y + \tfrac{3}{2}, && \psi_a \to T_{2,ab}\psi_b \\
P_x &: \quad y \to -y, && \psi_a \to P_{ab}\psi_b \\
R_{\pi/3} &: \quad \text{rotation by } \pi/3 && \psi_a \to R_{ab}\psi_b \\
TR &: \quad t \to -t, && \psi_a \to \psi_a
\end{aligned} \tag{2.7}$$

$R_{\pi/3}$ is a rotation by $\pi/3$ around a hexagon center. The PSG representation matrices $(T_{1,ab}, T_{2,ab}, P_{ab}, R_{ab})$ are given in Appendix 2.A. The low energy physics of the dual Hamiltonian (Eq. 2.4) can be completely described by ψ_a and its effective Lagrangian,

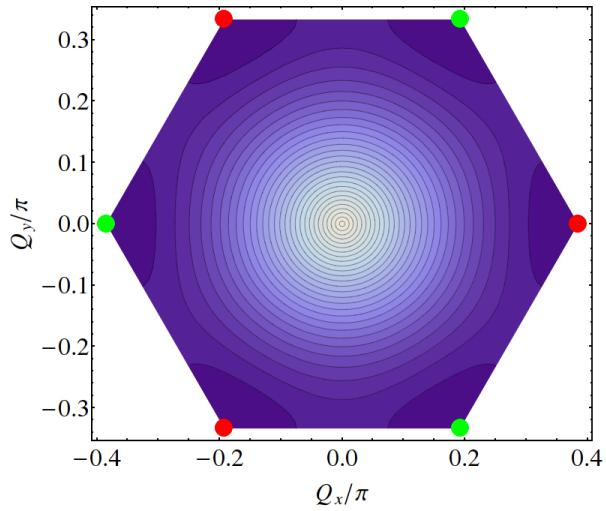

(a)

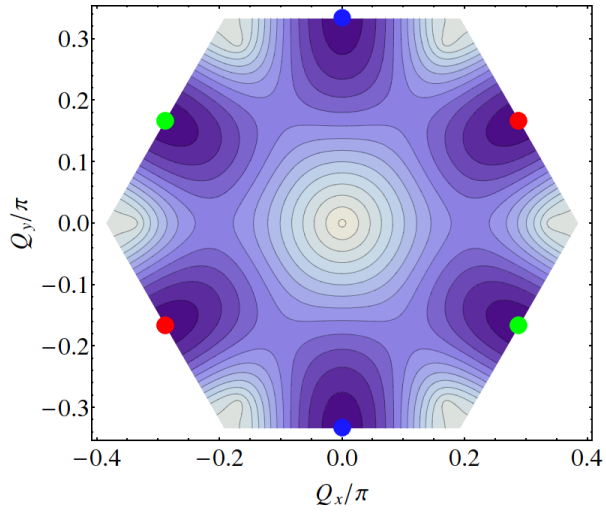

(b)

Figure 2.2: The contour plot of the lowest band in the band structure of the dual quantum Ising model (Eq. 2.4). Darker regions correspond to lower energy. (a), the band structure with only nearest neighbor Ising coupling (the case studied in [41]) which has four degenerate minimum modes. (b), the band structure with further neighbor Ising couplings (up to 7th neighbor) which has six degenerate minimum modes which are stable against perturbations and weak symmetry reduction. In both (a) and (b), each colored dot indicates a degenerate minima with two different modes (i.e. two orthogonal eigenvectors).

which must be invariant under the PSG. The PSG allowed Lagrangian reads

$$\mathcal{L} = \sum_{a=1}^{3} \left(|\partial_\mu \Psi_a|^2 + r\,|\Psi_a|^2 \right) + g \left(\sum_{a=1}^{3} |\Psi_a|^2 \right)^2$$

$$+ u \sum_{a=1}^{3} |\Psi_a|^4 + v \sum_{a=1}^{3} |\Psi_a|^2 |\Psi_{a+1}|^2 \cos(2\theta_a) \sin(2\theta_{a+1})$$

$$+ v_8 \sum_{a=1}^{3} |\Psi_a|^8 \cos(8\theta_a) + O(\Psi^6) \tag{2.8}$$

where $\Psi_a = |\Psi_a| e^{i\theta_a}$. The complex fields Ψ_a are defined as $\Psi_1 = \psi_1 + i\psi_2$, $\Psi_2 = \psi_3 + i\psi_4$, $\Psi_3 = \psi_5 + i\psi_6$ with $\Psi_{a+3} = \Psi_a$. The first three terms in $\mathcal{L}$ (Eq. 2.8) are invariant under an enlarged $O(6)$ rotation of ψ_a, while the u, v, and v_8 terms break this $O(6)$ symmetry down to a discrete symmetry. There are other 6th and 8th order terms that are allowed by the PSG, however they are unimportant to both the critical points and ordered phases considered in this paper. We always assume that g is the dominant 4th order term in $\mathcal{L}$ (Eq. 2.8). Under this assumption, there is a competition between u and v, and in the ordered phase ($r < 0$) these coefficients will determine the VBS pattern (see Fig. 2.4 for a phase diagram).

For example, if $u < -|v|/2$, then only one of the three $\langle \Psi_a \rangle$ will be nonzero. The v term is therefore irrelevant in this case and the sign of the 8th order v_8 term is necessary to fully determine $\langle \Psi_a \rangle$ in the ordered phase. The negative and positive v_8 correspond to the columnar and plaquette VBS orders on the triangular lattice respectively, both of which are 12 fold degenerate. For example, $\Psi_3 = e^{i\pi n/4}$ and $\Psi_1 = \Psi_2 = 0$ for $n = 0, 1, 2, 3$ are four examples of columnar VBS orders. These examples correspond to four VBS patterns with bonds (links with $\langle \sigma^x \rangle \sim -1$) aligning in the horizontal direction (Fig. 2.3*d*,*f*). Eight more examples are given by taking Ψ_1 or Ψ_2 to be nonzero instead of Ψ_3. Note

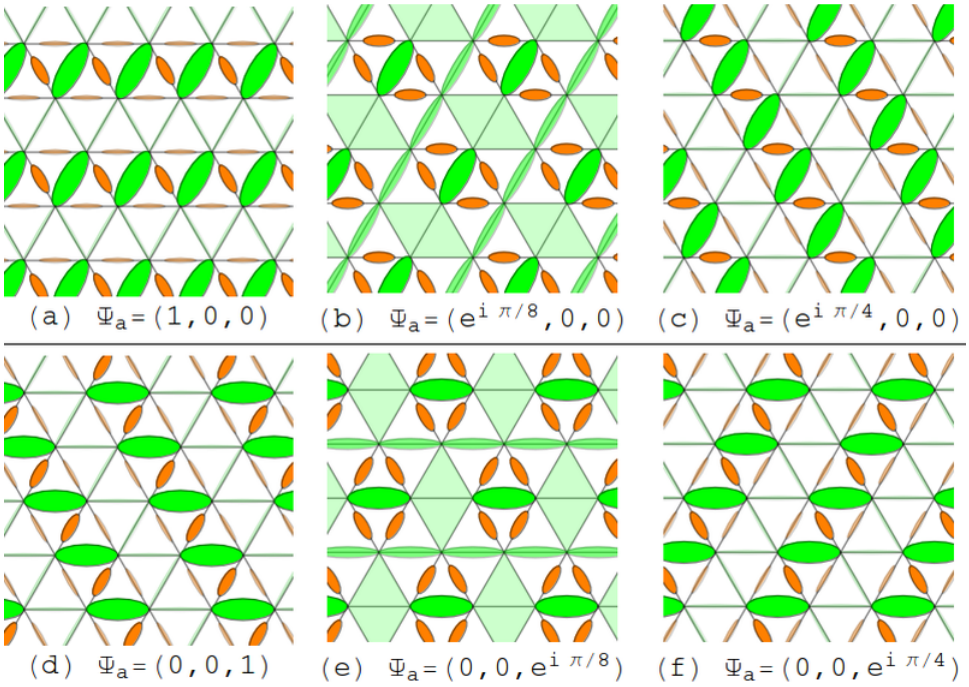

Figure 2.3: Plot of $\langle \sigma^x \rangle$ on the triangular lattice based on the ground state of our Lagrangian $\mathcal{L}$ (Eq. 2.8) with $u < -|v|/2$. Green bonds indicate valence bonds with $\langle \sigma^x \rangle < 0$ while orange bonds indicate links with $\langle \sigma^x \rangle > 0$. (a, c, d, f) show columnar VBS order while (b, e) show resonating-plaquette VBS order. In (b) and (e), the resonating-plaquettes are the diamonds highlighted in green.

that although taking $n = 4, 5, 6, 7$ in $\Psi_3 = e^{i\pi n/4}$ would give different condensations of Ψ, they are actually physically equivalent to $n = 0, 1, 2, 3$. This is because although τ^z and Ψ_a differ, σ^x is equivalent in these two cases since the vison fields τ^z and Ψ_a are only defined up to an arbitrary Z_2 gauge transformation $\Psi_a \to -\Psi_a$.

2.4 RG Analysis

Now let us study the nature of the quantum phase transition of $\mathcal{L}$ (Eq. 2.8). All of the 6th and 8th order terms will clearly be irrelevant at any critical points and can therefore be safely ignored. A standard ϵ-expansion in $d = 4 - \epsilon$ dimensions of the remaining terms

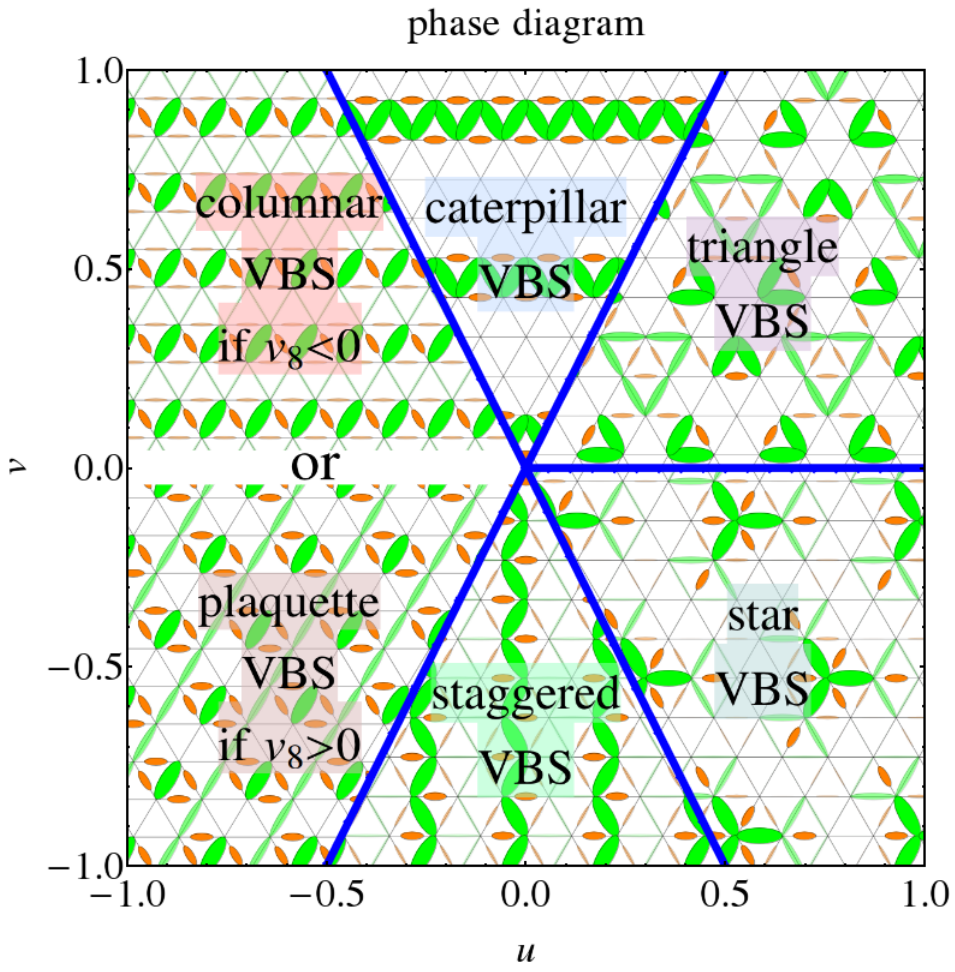

Figure 2.4: Phase diagram of our Lagrangian $\mathcal{L}$ (Eq. 2.8) in the ordered phase where $r < 0$. Green bonds indicate valence bonds with $\langle \sigma^x \rangle < 0$ while orange bonds indicate links with $\langle \sigma^x \rangle > 0$.

gives us the following β-functions:

$$-\beta_r = 2r - \frac{4}{3}rg - \frac{2}{3}ru$$

$$-\beta_g = g\epsilon - \frac{7}{3}g^2 - \frac{4}{3}gu - \frac{1}{6}v^2$$

$$-\beta_u = u\epsilon - 2gu - \frac{5}{3}u^2 + \frac{1}{12}v^2$$

$$-\beta_v = v\epsilon - 2gv - \frac{2}{3}uv \tag{2.9}$$

To simplify the equations, the above β-functions and the table of fixed points below are calculated using rescaled coefficients as in the following rescaled (and schematic) version of $\mathcal{L}$ (Eq. 2.8):

$$\mathcal{L}_{\text{RG}} = \frac{1}{2}\left(|\partial\Psi_a|^2 + r\,|\Psi_a|^2\right)$$

$$+ \frac{\Omega_d^{-1}}{4!}\left(g\,|\Psi_a^2|^2 + u\,|\Psi_a|^4 + v\,[\cdots]\right) \tag{2.10}$$

where $\Omega_d = \frac{d\pi^{d/2}}{\Gamma\left(\frac{d}{2}+1\right)}(2\pi)^{-d}$ is the surface area of a d dimensional ball, divided by $(2\pi)^d$. The above β-functions have four fixed points which are given in the following table

fixed points	r	g	u	v
gaussian	0	0	0	0
Ising	$-\frac{1}{5}\epsilon$	0	$\frac{3}{5}\epsilon$	0
Wilson-Fisher	$-\frac{2}{7}\epsilon$	$\frac{3}{7}\epsilon$	0	0
cubic	$-\frac{3}{11}\epsilon$	$\frac{3}{11}\epsilon$	$\frac{3}{11}\epsilon$	0

However, expansion of the $\beta-$functions around these fixed points shows that v is relevant at each of these fixed points. This implies that none of the ϵ-expansion fixed points can harbor a second order phase transition without fine tuning. Thus, there is likely a

run-away flow which suggests that the transitions described by the dual Lagrangian $\mathcal{L}$ (Eq. 2.8) are first order. [2] In the next section, we will describe why this does not appear to be the complete story for the columnar or plaquette VBS phase transitions.

2.5 Intermediate Phase

So far, we have assumed that there is only one phase transition when a VBS state is driven into a Z_2 liquid state. However, it is possible that there are two transitions with an intermediate phase in between that breaks less symmetry than the VBS phase. Without v and v_8, $\mathcal{L}$ (Eq. 2.8) has an emergent $U(1)^3 \times S_3$ symmetry in these phases. The three copies of $U(1)$ rotate the phases of the three Ψ_a while S_3 will permute the three Ψ_a. With a run-away flow under RG, the S_3 and U(1) symmetry can break separately. Since we are mainly interested in the case with only one of the Ψ_a condenses (the case with negative u) which corresponds to the columnar or plaquette VBS order, there could be an intermediate nematic phase which only breaks the S_3 symmetry. We introduce an additional complex nematic order parameter σ to describe the S_3 symmetry breaking (in addition to the three Ψ_a which will describe $U(1)^3$ symmetry breaking). Thus, the full

[2] In principle there is a chance that higher order $\epsilon-$expansion can lead to a different result, but we will proceed under the assumption that the first order result is qualitatively correct.

Landau-Ginzburg dual Lagrangian is

$$\widetilde{\mathcal{L}} = \sum_{a=1}^{3} \left(|\partial_\mu \Psi_a|^2 + r\,|\Psi_a|^2 \right) + g \left(\sum_{a=1}^{3} |\Psi_a|^2 \right)^2$$

$$+ u \sum_{a=1}^{3} |\Psi_a|^4 + v\,[\cdots] + v_8\,[\cdots]$$

$$+ |\partial_\mu \sigma|^2 + \tilde{r}\,|\sigma|^2 + \tilde{g}\,|\sigma|^4 - \tilde{u}_3(\sigma^3 + c.c.)$$

$$- \tilde{u} \left(\sigma^* \sum_{a=1}^{3} e^{-2\pi i a/3} |\Psi_a|^2 + c.c. \right) + \cdots \tag{2.11}$$

with $\tilde{u}_3, \tilde{u} > 0$ so that in the ordered phase only one of Ψ_a condenses.

We will now do a mean field analysis of $\widetilde{\mathcal{L}}$ (Eq. 2.11), tentatively neglecting the v and v_8 terms. $\widetilde{\mathcal{L}}$ can then be minimized by $\Psi_1 = \Psi_2 = 0$ with $\Psi_3 = \psi \geq 0$ and $\sigma \geq 0$ real valued. With this substitution, $\widetilde{\mathcal{L}}$ simplifies to

$$\widetilde{\mathcal{L}}_{\mathrm{MF}} = (r - 2\tilde{u}\,\sigma)\,\psi^2 + \tilde{r}\,\sigma^2 + (g+u)\,\psi^4 - 2\tilde{u}_3\,\sigma^3 + \tilde{g}\,\sigma^4 \tag{2.12}$$

The mean field phase diagram of $\widetilde{\mathcal{L}}_{\mathrm{MF}}$ (Eq. 2.12) is shown in Fig. 2.5.

The nature of the phase transition as $r + \tilde{r}$ is varied roughly depends on the sign of $r - \tilde{r}$. If $r \approx \tilde{r}$, then $r + \tilde{r}$ will drive the system through a first order transition from a Z_2 spin liquid to a columnar or plaquette VBS. However, if $r \ll \tilde{r}$ then mean field predicts a second order transition, while the RG analysis in the previous section implies that the v term in Eq. 2.8 will drive this transition first order. On the other hand, if $r \gg \tilde{r}$ then σ will want to order before Ψ_a which will give rise to an intermediate phase. Starting from the disordered phase (Z_2 spin liquid), as $r + \tilde{r}$ decreases there will be a phase transition to an intermediate ordered phase with $\langle \sigma \rangle \sim \left\langle \sum_{a=1}^{3} e^{-2\pi i a/3} |\Psi_a|^2 \right\rangle \neq 0$.

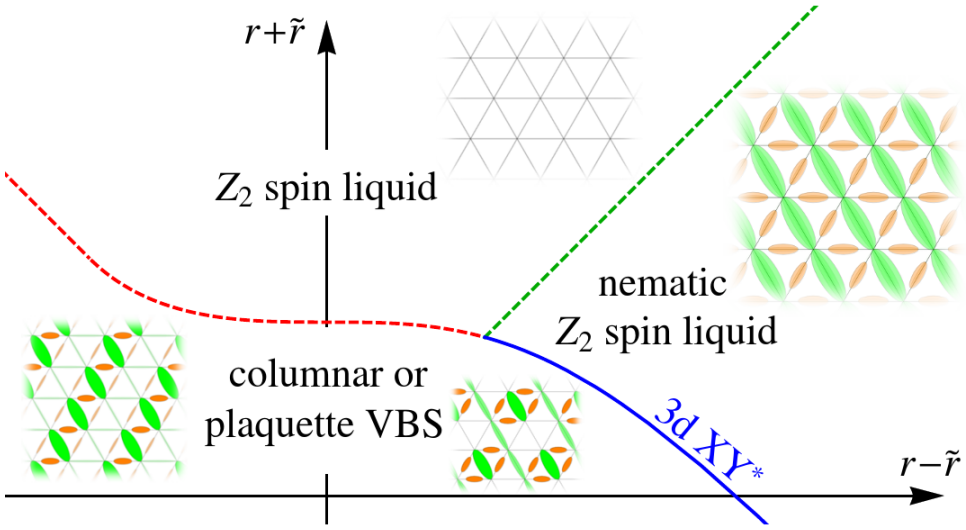

Figure 2.5: Phase diagram of $\widetilde{\mathcal{L}}$ (Eq. 2.11) and $\widetilde{\mathcal{L}}_{\rm MF}$ (Eq. 2.12) when $u < 0$. Solid lines and dotted lines stand for second and first order transitions respectively. The nature of the phase transition as $r + \tilde{r}$ is varied roughly depends on the sign of $r - \tilde{r}$. For example, if $r \gg \tilde{r}$, then starting in the Z_2 spin liquid phase, as $r + \tilde{r}$ decreases there will be a first order transition to an intermediate phase, and then a second order 3d XY* transition to a VBS phase.

This phase transition will spontaneously break the S_3 symmetry but keep the $U(1)^3$ symmetry, and the $\tilde{u}_3$ term in Eq. 2.12 will drive the transition to a first order $q = 3$ Potts transition. Physically, this intermediate phase will be a nematic Z_2 spin liquid that breaks the $2\pi/3$ lattice rotation symmetry. As $r + \tilde{r}$ is decreased further, there will be another phase transition which will break the remaining $U(1)$ symmetry. This phase transition is described by the following theory:

$$\mathcal{L}_3 = |\partial_\mu \Psi_3|^2 + r\,|\Psi_3|^2 + g\,|\Psi_3|^4 + g_6\,|\Psi_3|^6$$

$$+ v_8\,|\Psi_3|^8 \cos(8\theta_3) + O(\Psi^8) \tag{2.13}$$

If we view Ψ_3 as an order parameter, this transition is in the 3d XY universality class because v_8 is strongly irrelevant.

We have yet to discuss the effects of the topological nature of the Z_2 liquid on any

second order phase transitions to a VBS phase. These effects can be understood by noting that any physical order parameter must be bilinear of ψ_a. This is required because if $\psi_a \to -\psi_a$ then $\tau_z \to -\tau_z$ (Eq. 2.6) but σ^x and σ^z will remain invariant. Thus there is a global Z_2 gauge redundancy in the definition of ψ_a and so only quantities that are quadratic in ψ_a will be gauge invariant. For example, the columnar and plaquette VBS order parameters are $V_a \sim \Psi_a^2$. Being quadratic in ψ, this order parameter will have an enormous anomalous dimension η where

$$\langle V_a(x)\ V_a(x')\rangle \sim \frac{1}{|x-x'|^{1+\eta}} \tag{2.14}$$

Note that η must be greater than 1 ($\eta = 1$ in a free field theory with a bilinear order parameter), which is much larger than any ordinary Wilson-Fisher fixed point. Therefore, a 3d XY transition in the dual theory is referred to as a 3d XY* transition in the original theory in order to denote the difference. Thus, the above 3d XY* transition should have the same dynamical exponent $z = 1$ and critical exponent ν as an ordinary 3d XY transition, but with a much larger anomalous dimension $\eta \sim 1.49$ [33] for the VBS order parameter.

2.6 Anisotropic Triangle Lattices

All of the previous discussions were under the assumption that the triangular lattice is fully isotropic. In real materials, a triangular lattice is usually distorted. For example, in the triangular lattice spin-1/2 material Cs_2CuCl_4 [63, 64], the Heisenberg coupling is much stronger along one of the three directions. Now let us break the $\pi/3$ rotation symmetry but keep the translation (T_1,T_2), reflection $y \to -y$ (P_x), and inversion $\vec{r} \to -\vec{r}$ ($R_{\pi/3}{}^3$) symmetries. This is precisely the symmetry of the material Cs_2CuCl_4. The locations of the minima in the BZ are stable against this symmetry reduction. However,

although Ψ_1 and Ψ_2 are still degenerate, they are no longer degenerate with Ψ_3; namely the 12 fold degeneracy between different columnar VBS orders will be lifted.

If Ψ_3 is the lowest energy mode (*i.e.* the spin coupling along the horizontal links on the triangular lattice is stronger than the other two directions), then the PSG allowed Lagrangian is precisely Eq. 2.13. Again, depending on the sign of v_8, the ground state of the VBS phase (the phase with $r < 0$) is either a columnar (Fig. 2.3*d*,*f*) or plaquette (Fig. 2.3*e*) VBS, both four-fold degenerate. The liquid-VBS phase transition still belongs to the well-studied 3d XY* transition.

If Ψ_1 and Ψ_2 are the lowest energy modes, then the low energy effective Lagrangian reads

$$\begin{aligned}\mathcal{L}_{12} &= \sum_{a=1,2} \left(|\partial_\mu \Psi_a|^2 + r\,|\Psi_a|^2\right) + g\left(\sum_{a=1,2} |\Psi_a|^2\right)^2 \\ &+ u \sum_{a=1,2} |\Psi_a|^4 + v\,|\Psi_1|^2|\Psi_2|^2 \cos(2\theta_1)\sin(2\theta_2) \\ &+ v'\left(|\Psi_1|^4\cos(4\theta_1) - |\Psi_2|^4\cos(4\theta_2)\right) \end{aligned} \tag{2.15}$$

Again we focus on the case with $u < -|v|/2$ when exactly one of $\langle\Psi_a\rangle$ is nonzero. (This eliminates the role of the v term in the ordered phase.) In this case, for either sign of v', the vison condensate is a four-fold degenerate columnar VBS state (Fig. 2.3*a*,*c*).

Now let us further reduce the symmetry. For example, if the P_x ($y \to -y$) symmetry is broken while inversion is still preserved (this is the symmetry of most organic spin liquid materials), then the columnar VBS order has only a two-fold degeneracy which only breaks translation symmetry. Now the PSG allowed Lagrangian reads

$$\mathcal{L}_3' = |\partial_\mu \Psi_3|^2 + r\,|\Psi_3|^2 + g\,|\Psi_3|^4 + v\,|\Psi_3|^4\cos(4\theta_3) \tag{2.16}$$

For either sign of v, there is a two-fold degenerate columnar VBS order. In this case the

liquid-VBS transition is still the 3d XY* transition because it is well-known that the Z_4 anisotropy $\cos(4\theta)$ on a 3d XY fixed point irrelevant [65, 66].

Close to the liquid-VBS critical point, since v_8 in Eq. 2.13 and v in Eq. 2.16 are both irrelevant, Eq. 2.13 and Eq. 2.16 have an emergent $U(1)$ global symmetry. Thus we can view the VBS order as a superfluid phase that spontaneously breaks this $U(1)$ symmetry; therefore the liquid-VBS transition can also be viewed as a liquid-superfluid phase transition. If we approach this critical point from the superfluid (VBS) side, then this transition is driven by the proliferation of vortex excitations of the superfluid phase. In 2+1d space-time, a superfluid phase is dual to a bosonic QED: a scalar boson (vortex field) coupled to a 2+1d U(1) gauge field. Therefore this liquid-VBS phase transition is dual to a Higgs transition:

$$\mathcal{L}_{dual} = |(\partial_\mu - i2a_\mu)^2\Phi| + r'|\Phi|^2 + g'|\Phi|^4 + \frac{1}{e^2}f_{\mu\nu}^2 \tag{2.17}$$

where Φ is a complex field that annihilates a pair of vortices. After condensation ($r' < 0$) Φ breaks the $U(1)$ gauge field to a Z_2 gauge field. Hence the condensate of vortex pairs has a Z_2 topological order, which is precisely the topological order of the Z_2 spin liquid state we started with.

2.7 Conclusion

In summary, in this chapter we studied the quantum phase transition between Z_2 liquid and columnar VBS orders on both the isotropic and distorted triangular lattices. The critical theories proposed in this chapter can be checked by future numerical simulations once a Z_2 spin liquid phase is identified on the triangular lattice. It would also be interesting to study the direct quantum phase transition from the magnetic order to the columnar VBS orders on the triangular lattice, which can be viewed as a triangular lat-

tice generalization of the deconfined quantum critical point [8, 9]. This transition would be driven by condensation of skyrmions or vortices of the magnetic order. Eventually we also plan to understand the global phase diagram around the Z_2 spin liquid, which probably involves a noncollinear spiral spin order, the columnar/plaquette VBS order discussed in this current paper, and a collinear spin order. A similar global phase diagram was studied in [12] for the case with four vison minima in the BZ, and we plan to generalize this to our current case with columnar VBS order. We expect to understand this global phase diagram for both spin-1/2 and spin-1 systems on the triangular lattice. We will leave these subjects to future study.

2.8 Permissions and Attributions

The content of this chapter is the result of a collaboration with Cenke Xu, and has previously appeared in [67]. The authors would like to thanks Leon Balents for pointing out that there could be an intermediate phase between a Z_2 spin liquid and VBS (Fig. 2.5). CX is supported by the Alfred P. Sloan Foundation, the David and Lucile Packard Foundation, the Hellman Family Foundation, and NSF Grant No. DMR-1151208.

2.A Appendix

In this appendix we present more details about the dual frustrated quantum Ising model. With a 7th neighbor Ising coupling, in a finite region of the phase diagram, the minima of the vison band structure are stabilized at six different minimum modes

(Fig. 2.2*b*) with momenta

$$\vec{Q}_1 = \vec{Q}_2 = (\frac{\pi}{2\sqrt{3}}, \ -\frac{\pi}{6})$$

$$\vec{Q}_3 = \vec{Q}_4 = (\frac{\pi}{2\sqrt{3}}, \ +\frac{\pi}{6})$$

$$\vec{Q}_5 = \vec{Q}_6 = (0, \ \frac{\pi}{3}) \tag{2.18}$$

To analyze the low energy physics, we can expand the Ising operator τ^z at these six minima:

$$\tau^z_{r,n} = \sum_{a=1}^{6} \psi_a(r) v_{a,n} e^{i\vec{Q}_a \cdot \vec{r}} \tag{2.19}$$

where r takes on values at the center of the unit cell diamonds (Fig. 2.1). In this equation, $v_{a,n}$ are six eight-component vectors:

$$v_1 = \begin{pmatrix} +1 \\ +f \\ +f \\ -f \\ +1 \\ +1 \\ +1 \\ +f \end{pmatrix}, \quad v_2 = \begin{pmatrix} -f \\ -1 \\ +1 \\ +1 \\ +f \\ -f \\ +f \\ +1 \end{pmatrix}, \quad v_3 = \begin{pmatrix} +1 \\ +1 \\ +1 \\ +f \\ +1 \\ +f \\ -f \\ +f \end{pmatrix}$$

$$v_4 = \begin{pmatrix} -f \\ +f \\ +f \\ +1 \\ -f \\ -1 \\ +1 \\ +1 \end{pmatrix}, \quad v_5 = \begin{pmatrix} +1 \\ -1 \\ +f \\ -1 \\ -f \\ -1 \\ -f \\ +f \end{pmatrix}, \quad v_6 = \begin{pmatrix} -f \\ +f \\ -1 \\ -f \\ +1 \\ -f \\ -1 \\ +1 \end{pmatrix} \tag{2.20}$$

where $f = \sqrt{2} - 1$.

The low energy modes ψ_a carry a six dimensional representation of the PSG of the system. The entire PSG of the system is generated by the transformations in Eq. 2.7.

The representation matrices are

$$T_1 = \begin{pmatrix} -1 & 0 & 0 & 0 & 0 & 0 \\ 0 & +1 & 0 & 0 & 0 & 0 \\ 0 & 0 & 0 & +1 & 0 & 0 \\ 0 & 0 & +1 & 0 & 0 & 0 \\ 0 & 0 & 0 & 0 & 0 & +1 \\ 0 & 0 & 0 & 0 & -1 & 0 \end{pmatrix} \qquad T_2 = \begin{pmatrix} 0 & +1 & 0 & 0 & 0 & 0 \\ -1 & 0 & 0 & 0 & 0 & 0 \\ 0 & 0 & +1 & 0 & 0 & 0 \\ 0 & 0 & 0 & -1 & 0 & 0 \\ 0 & 0 & 0 & 0 & 0 & -1 \\ 0 & 0 & 0 & 0 & -1 & 0 \end{pmatrix}$$

$$P_x = \begin{pmatrix} 0 & 0 & \frac{1}{\sqrt{2}} & \frac{1}{\sqrt{2}} & 0 & 0 \\ 0 & 0 & \frac{1}{\sqrt{2}} & -\frac{1}{\sqrt{2}} & 0 & 0 \\ \frac{1}{\sqrt{2}} & \frac{1}{\sqrt{2}} & 0 & 0 & 0 & 0 \\ \frac{1}{\sqrt{2}} & -\frac{1}{\sqrt{2}} & 0 & 0 & 0 & 0 \\ 0 & 0 & 0 & 0 & \frac{1}{\sqrt{2}} & \frac{1}{\sqrt{2}} \\ 0 & 0 & 0 & 0 & \frac{1}{\sqrt{2}} & -\frac{1}{\sqrt{2}} \end{pmatrix} \qquad R_{\pi/3} = \begin{pmatrix} 0 & 0 & 0 & -1 & 0 & 0 \\ 0 & 0 & +1 & 0 & 0 & 0 \\ 0 & 0 & 0 & 0 & 0 & +1 \\ 0 & 0 & 0 & 0 & -1 & 0 \\ 0 & +1 & 0 & 0 & 0 & 0 \\ -1 & 0 & 0 & 0 & 0 & 0 \end{pmatrix} \tag{2.21}$$

Chapter 3

Exotic Quantum Phase Transitions of Strongly Interacting Topological Insulators

Using determinant quantum Monte Carlo (d-QMC) simulations, we demonstrate that an extended Hubbard model on a bilayer honeycomb lattice has two novel quantum phase transitions. The first is a quantum phase transition between the weakly interacting gapless Dirac fermion phase and a strongly interacting fully gapped and symmetric trivial phase, which cannot be described by the standard Gross-Neveu model. The second is a quantum critical point between a quantum spin Hall insulator with spin S^z conservation and the previously mentioned strongly interacting fully gapped phase. At the latter quantum critical point the single particle excitations remain gapped, while spin and charge gap both close. We argue that the first quantum phase transition is related to the $\mathbb{Z}_{16}$ classification of the topological superconductor ^{3}He-B phase with interactions, while the second quantum phase transition is a topological phase transition described by a bosonic O(4) nonlinear sigma model field theory with a Θ-term.

3.1 Introduction

—

The interplay between topology and interactions can lead to very rich new physics. For bosonic systems, it is understood that strong interactions can lead to many symmetry protected topological (SPT) phases [17, 18] that are fundamentally different from the standard Mott insulator and superfluid phases. In addition to producing various topological orders, for fermionic systems strong interactions can also reduce the classification of free fermion topological insulators and superconductors [68, 69, 70, 71, 72, 73, 74, 75, 76]. That is, interactions can drive free fermion topological superconductors to a trivial phase; namely the edge states of the free fermion topological superconductor can be gapped out without degeneracy by a symmetry preserving short range interactions without going through a bulk quantum phase transition. The most famous example is the ^{3}He-B topological superconductor protected by time-reversal symmetry, whose boundary is described by a $(2+1)d$ Majorana fermion χ with the Hamiltonian $H = \int d^2x\ \chi^\intercal(i\sigma^z\partial_x + i\sigma^x\partial_y)\chi$. Without interactions, ^{3}He-B has a $\mathbb{Z}$ classification; therefore for arbitrary copies of ^{3}He-B, its boundary remains gapless as long as time-reversal symmetry is preserved [77, 78, 79]. In other words any fermion-bilinear mass term $\chi_a^\intercal\sigma^y\chi_b$ at the boundary would break the time-reversal symmetry. However, once interactions are turned on, the classification of ^{3}He-B is reduced to $\mathbb{Z}_{16}$; *i.e.*, with 16 copies of ^{3}He-B, its boundary can be gapped out by interactions while preserving the time-reversal symmetry [74, 75]. In other words, the boundary is fully gapped by interactions with $\langle\chi_a^\intercal\sigma^y\chi_b\rangle = 0$, for $a, b = 1\cdots 16$.

Although the classification of interacting ^{3}He-B has been understood, the following question remains: if the interactions are tuned continuously, can there be a direct second order quantum phase transition between the weakly interacting gapless boundary and the strongly interacting fully gapped nondegenerate boundary state? Even if such a second

order phase transition exists, its field theory description is unknown because the standard field theory that describes a phase transition of interacting Dirac or Majorana fermions is the Gross-Neveu model [80], which corresponds to the order-disorder phase transition of a bosonic field ϕ_{ab} that couples to a fermion bilinear mass operator: $\phi_{ab}\chi_a^\intercal\sigma^y\chi_b$ [1]. Therefore in the Gross-Neveu model, the gap of the Majorana fermion is induced by a nonzero expectation value of a fermion bilinear mass: $\langle\chi_a^\intercal\sigma^y\chi_b\rangle \neq 0$, which would break the time-reversal symmetry at the boundary of ^{3}He-B.

In this paper we will demonstrate that such a novel direct second order transition indeed exists, which is fundamentally different from the standard Gross-Neveu theory. But instead of studying the boundary of a $3d$ system (which is numerically challenging), we will just study a $2d$ lattice model, whose low energy field theory Lagrangian is identical to the boundary of 16 copies of ^{3}He-B, although its fields transform very differently under symmetry groups (the exact boundary field theory of ^{3}He-B cannot be realized in $2d$). We will demonstrate that in this $2d$ lattice model there is indeed a direct second order quantum phase transition between 16 flavors of gapless $(2+1)d$ Majorana fermions (8 copies of Dirac fermions) and a fully gapped phase that does not break the symmetry of the lattice model. This shows that the fermion gap does not correspond to any fermion bilinear mass.

We will also study another exotic quantum phase transition between the weakly interacting quantum spin Hall (QSH) insulator with spin S^z conservation and spin topological numer 2, and the fully gapped and symmetric phase in the strong interaction limit mentioned in the previous paragraph. In the noninteracting limit, the phase transition between the topological insulator and trivial insulator is driven by closing the Dirac mass gap, which requires that the single particle excitation is gapless at the critical

[1] In the original Gross-Neveu model introduced in Ref. [80], ϕ_{ab} is always an identity matrix. Here we use a generalized definition of the Gross-Neveu model.

point. However, in this paper we demonstrate that, with interaction, at this quantum phase transition the spin and charge gap both close, while the single particle excitation remains gapped. Therefore, this quantum phase transition only involves bosonic degrees of freedom, which allows this quantum phase transition to be described by a bosonic field theory. We propose that the field theory for this transition is an O(4) nonlinear sigma model field theory with a Θ-term. The QSH insulator and the trivial phase correspond to $\pi < \Theta \leq 2\pi$ and $0 \leq \Theta < \pi$ respectively, while the quantum critical point corresponds to $\Theta = \pi$.

3.2 Model Hamiltonian

—

The Hamiltonian we study is an interacting spin-1/2 fermion system defined on a bilayer honeycomb lattice (Fig. 3.1):

$$\begin{aligned} H &= T + T' + W \\ T &= -t \sum_{\langle ij \rangle} \sum_{\ell,s} \left(c^\dagger_{i\ell s} c_{j\ell s} + h.c. \right) \\ T' &= i\lambda \sum_{\langle\langle ij \rangle\rangle} \sum_{\ell} \nu_{ij} c^\dagger_{i\ell} \sigma^z c_{j\ell} \\ W &= \frac{U}{2} \sum_{i,\ell} (n_{i\ell} - 1)^2 \\ &\quad + J \sum_i \left[\boldsymbol{S}_{i1} \cdot \boldsymbol{S}_{i2} + \frac{1}{4}(n_{i1} - 1)(n_{i2} - 1) - \frac{1}{4} \right] \end{aligned} \tag{3.1}$$

where $s = \uparrow, \downarrow$ and $\ell = 1, 2$ denote the spin and layer index. $T + T'$ corresponds to two layers of the Kane-Mele model[81], and W describes both the on-site and the inter-layer interactions. We will set $t = 1$ as the energy unit throughout this paper. We also define $n_{i\ell} = n_{i\ell\uparrow} + n_{i\ell\downarrow}$, $S^\mu_{i\ell} = \frac{1}{2} c^\dagger_{i\ell} \sigma^\mu c_{i\ell}$, and $n_{i\ell s} = c^\dagger_{i\ell s} c_{i\ell s}$. $\langle\langle i, j \rangle\rangle$ stands for a next-nearest-neighbor lattice link. $\nu_{ij} = \pm 1$ depending on whether the hopping path defined by the

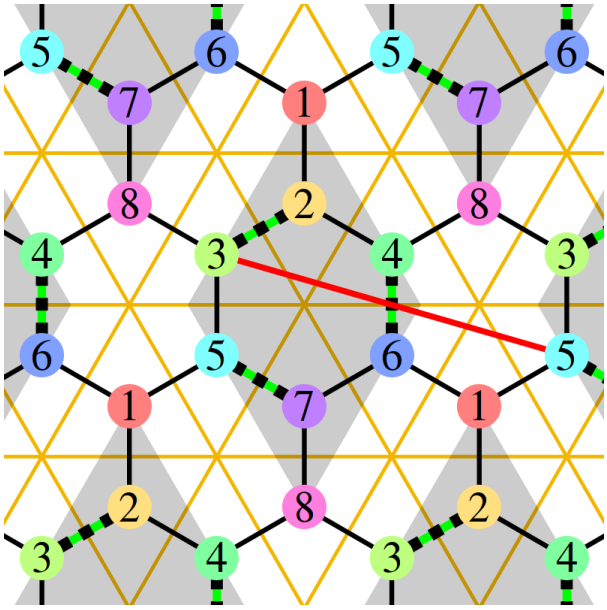

Figure 3.1: The bilayer honeycomb lattice. In each layer, t and λ are the nearest- and next-nearest-neighbor hopping. The Hubbard interaction U acts on each site, and the Heisenberg interaction J acts across the layers.

nearest-neighbor bonds connecting sites i and j bends to the right or to the left. With only the T term, the low energy limit of this model is described by 8 flavors of $(2+1)d$ massless Dirac fermions (or 16 Majorana fermions) in its Brillouin zone.

In the noninteracting limit, *i.e.* $U = J = 0$, a nonzero λ will cause the T' term to gap out T and drive the system into a QSH phase with spin topological numer $C_s = \pm 2$ which corresponds to the quantized spin Hall conductance $\sigma_H^{\text{spin}} = \frac{e}{2\pi} C_s$. The U term in the Hamiltonian W is a Hubbard repulsion while the J term consists of an antiferromagnetic Heisenberg spin interaction between the two layers and a density-density interaction. In this paper we will fix $J/U = 2$ (with positive U and J). The interaction tends to gap out the charge fluctuations and couples the spins across the layers into the singlet state on each site. Then in the strong interacting limit, the ground state is simply a product

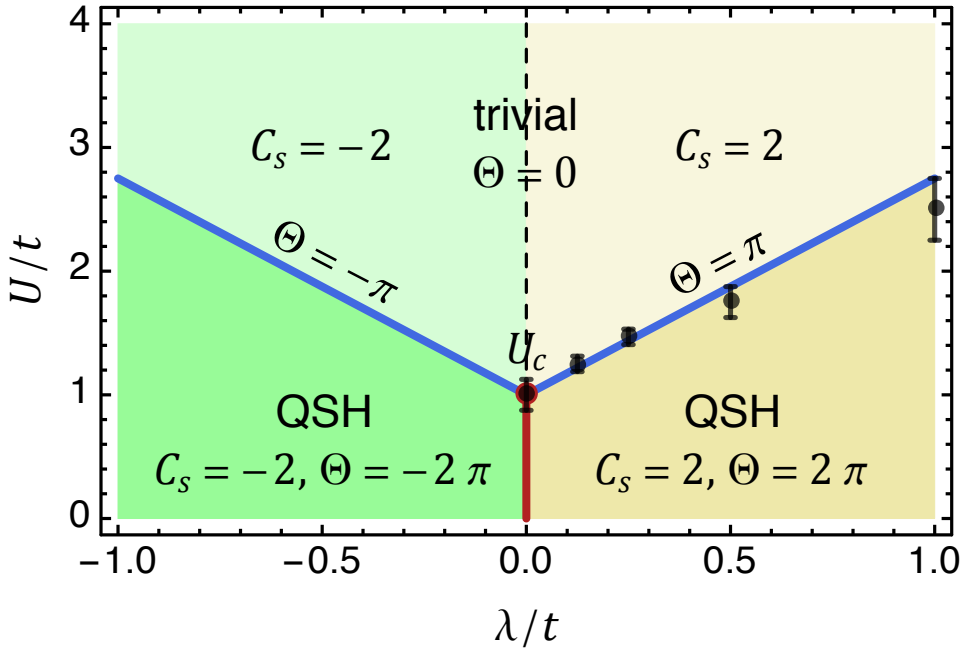

Figure 3.2: (Color online.) A schematic phase diagram of the bilayer honeycomb model. The red line is the phase boundary between the two QSH phases of opposite spin Hall conductivity, where both the single particle and the spin/charge gaps are closed. The blue line is the phase boundary between the QSH phase $\Theta = \pm 2\pi$ and the trivial gapped phase $\Theta = 0$, where the single particle gap remains open but the spin/charge gaps are closed. U_c is the tricritical point, above which the topological number defined in Eq. 3.6 changes inside the trivial phase (without gap closing) through the dashed line, also see Fig. 3.3.

state of inter-layer spin singlets,

$$|\Psi\rangle = \prod_i (c^\dagger_{i1\uparrow} c^\dagger_{i2\downarrow} - c^\dagger_{i1\downarrow} c^\dagger_{i2\uparrow})|0\rangle, \tag{3.2}$$

which is a trivial gapped state that respects all of the symmetry. Obviously this strongly interacting trivial state should not have any spin Hall response, thus it must be separated from the weak interacting QSH states by phase transitions. The phase diagram of this model is depicted in Fig. 3.2. Note that the spin topological number C_s shown in the phase diagram is calculated from the single-particle Green's function (to be discussed later in Eq. 3.6), and in the strong interacting regime, C_s is no longer related to the spin Hall conductance σ_H^{spin}. In fact, $\sigma_H^{\text{spin}} = 0$ holds for the entire trivial insulating phase

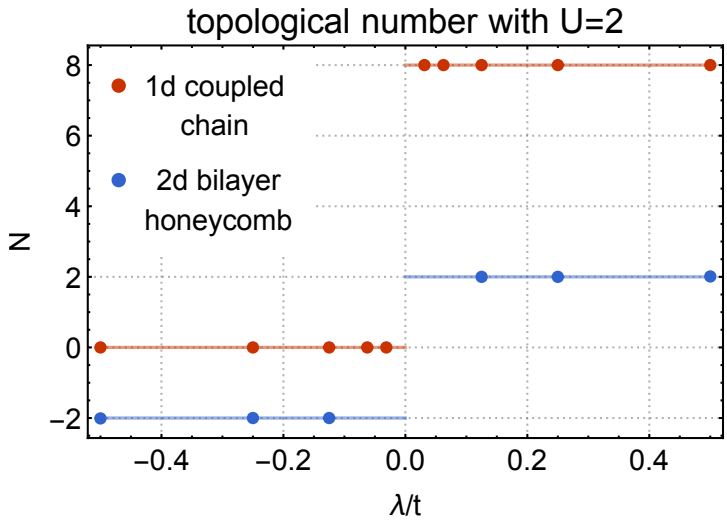

Figure 3.3: The topological number defined in Eq. 3.6 as a function of λ for both models at $U = 2$. The topological number was calculated at the dots using DQMC data via the methods discussed in the Topological Number Calculation Methods appendix. This demonstrates that this topological number Eq. 3.6 is nonzero even in the strongly interacting trivial phase.

despite of $C_s = \pm 2$.

It is also worth mention that if we fix the ratio $J/U \ll 1$ and increase the interaction gradually, then an intermediate antiferromagnetic (AF) phase could set in between the trivial phase and the QSH phase, because a nearest neighbor AF interaction $\sim t^2/U$ could be generated through superexchange. However we will leave this intermediate AF phase for future investigation, and focus on the $J/U = 2$ case where the trivial and the QSH phases are separated by only one single phase transition which turns out to be more exotic.

3.3 Phases and Excitation Gaps

—

Before we present our results for the $2d$ model, we will first consider a $1d$ system

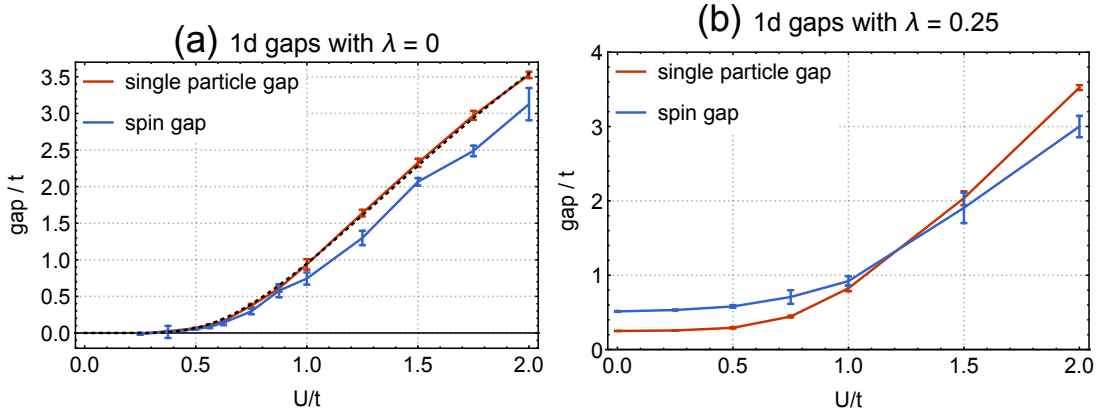

Figure 3.4: Single particle and spin gap for the 1d coupled chain model with $J/U = 2$. **(a)** When $\lambda = 0$, the system is gapped out immediately by an infinitesimal interaction with a gap of the form $e^{a-b/U}$ for small U (dotted black line with $a = 2.60$ and $b = 2.65$). **(b)** When $\lambda = 0.25$, there are no phase transitions when $\lambda \neq 0$ and $U > 0$.

composed of two coupled chains. In this $1d$ system, T' becomes

$$T'_{1\mathrm{d}} = -\frac{\lambda}{2}\sum_{i,\ell,s}(-)^i\left(c^\dagger_{i+1,\ell,s}c_{i,\ell,s} + h.c.\right) \tag{3.3}$$

In the noninteracting limit, $\lambda < 0$ corresponds to 4 copies of the Su-Schrieffer-Heeger model of polyacetylene[82] or 8 copies of the Kitaev's $1d$ topological superconductor[2] with a nontrivial boundary state, while $\lambda > 0$ corresponds to a trivial state [68]. We are interested in connecting the $\lambda < 0$ SPT phase to the $\lambda > 0$ trivial phase without a phase transition. (This demonstrates the already known fact that $\lambda < 0$ and $\lambda > 0$ are actually in the same phase under interaction [68].) Fidkowski and Kitaev demonstrated how to do this in one dimension using an interaction term [68] which corresponds to W but with a simpler J term: $+J\boldsymbol{S}_{i,1}\cdot\boldsymbol{S}_{i,2}$. We modify Fidkowski and Kitaev's interaction term slightly so that it can be simulated by quantum Monte Carlo (QMC) without a sign problem [83]. This modification will not change the qualitative results of the model.

Our results are depicted in Fig. 3.4(a) and Fig. 3.4(b). With $\lambda = 0$, the system is

[2]Eq. 3.3 has four flavors of complex fermions, which can be written as 8 flavors of Majorana fermion chains up to a basis transformation, i.e. 8 copies of Kitaev's 1d topological SC.

gapped out immediately with infinitesimal interaction, because as was computed explicitly, the four fermion term is marginally relevant at $\lambda = 0$. The gap we measure scales exponentially with $1/U$, which is consistent with the renormalization group calculation. With finite λ, there is no phase transition at finite U, see Fig. 3.4(b); namely the entire phase diagram of this $1d$ system is one trivially gapped phase except for the isolated gapless point $\lambda = U = J = 0$.

Now let us move on to the honeycomb lattice. It is well-known that a weak short range interaction is irrelevant for a massless $(2+1)d$ Dirac/Majorana fermion, which implies that the interaction can gap out the fermion only when it is strong enough. Thus along the $\lambda = 0$ axis in Fig. 3.2, a semimetal-insulator phase transition is expected at finite U/t. Indeed, our numerical results suggest that with increasing U/t, there is one continuous phase transition at finite $U_c/t \sim 1$ where the single particle gap opens up gradually from zero, and the single particle gap increases monotonically afterwards. In the large U/t limit, this model is exactly soluble, and the ground state is a trivial direct product of on-site spin singlets between the two layers as in Eq. 3.2. Therefore in the large U/t limit this gapped phase does not correspond to any fermion quadratic mass term. But it is still possible that some other symmetry breaking order parameters may emerge for intermediate U/t. To verify that this is not the case, we performed a mean field analysis where we focus on the order parameters that minimize the energy of the interaction term at the mean field level. The details of this mean field analysis are presented in the Mean-Field Energy of Order Parameters appendix. We identify three order parameters that could potentially minimize the interaction energy: the antiferromagnetic spin density wave (SDW) order, the interlayer spin singlet Cooper pairing, and the interlayer exciton excitation. Among them, the SDW order and the exciton order can be rotated to each other under an $SO(5)$ symmetry emerged at $J = 2U$ point (see the appendix Continuous Symmetries). So we only need to check the SDW and the pairing orders. Our numerical

results suggest that none of these order parameters emerge and stabilize in the entire phase diagram (spin and charge gap open up continuous from the same critical point as the single particle gap). Thus we conclude that there can indeed be a continuous quantum phase transition between the gapless Dirac/Majorana fermion phase in the weak interacting limit and the fully gapped symmetric trivial phase in the strong interaction limit.

Since the quantum phase transition is continuous, there must be a field theory description for this phase transition. Furthermore, this field theory must be described by a Lagrangian with 16 flavors of $(2+1)d$ Majorana fermions with four-fermion short range interactions, but its physics and universality class must be fundamentally different from the standard Gross-Neveu model. The same field theory Lagrangian must be applicable to the interaction driven mass gap at the boundary of 16 copies of the ^{3}He-B phase. The only difference is that, at the $2d$ boundary of ^{3}He-B a fermion bilinear mass term is prohibited by time-reversal symmetry only, while in our $2d$ lattice model crystalline symmetry is required to prevent fermion bilinear mass terms.

We also note that a similar phase transition between gapless Dirac fermions and a symmetric gapped phase was recently also studied in high energy physics communities[84].

Now let us consider the case with finite λ. In the noninteracting limit, a finite λ term will drive the system into a quantum spin Hall insulator with spin topological numer $C_s = 2$; *i.e.* the Chern number for spin-up (spin-down) fermion is $+2$ (-2) (see Eq. 3.6 for definition). Because our system has S^z conservation, this state is still a nontrivial topological insulator with stable boundary states. While increasing U/t, there must be a quantum phase transition between this topological insulator and the strongly coupled trivial gapped state (blue line in the phase diagram Fig. 3.2). In the noninteracting limit, the transition between a topological insulator and trivial insulator is driven by closing the Dirac fermion gap. In Fig. 3.5(b) we can see that there is indeed a quantum

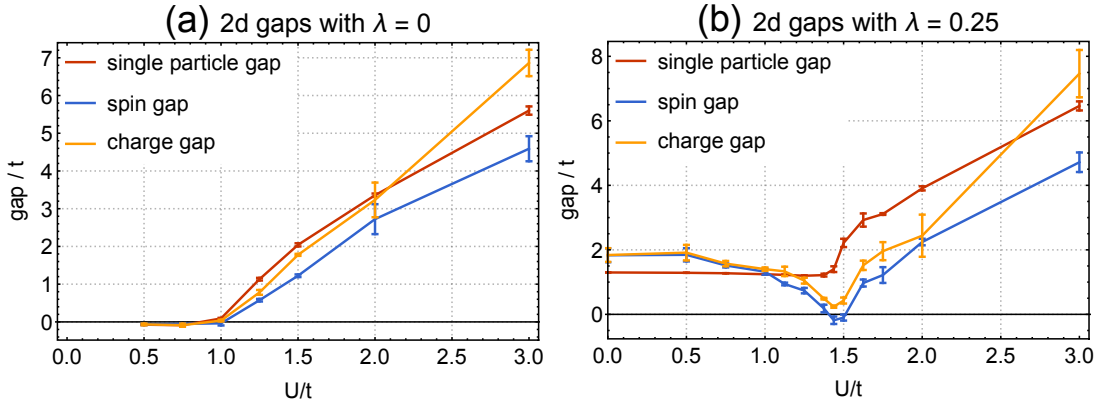

Figure 3.5: Single particle gap, spin gap (gap for spin-1 excitation), and charge gap (gap for charge-2 excitation) on the bilayer honeycomb lattice with $J/U = 2$. **(a)** When $\lambda = 0$, there is a single continuous phase transition from a semimetal to a trivial insulator at $U_c \sim 1$, whose field theory also describes the phase transition of the boundary of 16 copies of the ^{3}He-B phase. **(b)** When $\lambda = 0.25$, only the spin and charge gap close at the continuous phase transition from an SPT to a trivial insulator (which is at $U_c \sim 1.5$ for $\lambda = 0.25$). We propose that this phase transition is described by a bosonic O(4) nonlinear sigma model field theory with a Θ-term [Eq. 3.5]. These gaps are calculated as explained in the Gap Calculation Methods appendix. This involves calculating gaps in finite systems of sizes up to 9x9 unit cells (with 4 sites each) and extrapolating to the infinite size limit. Error bars on all figures denote one standard deviation (*i.e.* $\approx 68\%$ confidence).

phase transition at finite U/t; but at this quantum critical point the single particle gap does not close, while our data suggests that the gaps for the SDW fluctuation ($\hat{N}^x \sim (-1)^{i+\ell} c^\dagger_{i,\ell} \sigma^x c_{i,\ell}$, $\hat{N}^y \sim (-1)^{i+\ell} c^\dagger_{i,\ell} \sigma^y c_{i,\ell}$) and the pairing fluctuation ($\hat{\Delta} \sim c^\intercal_{i,1} \mathrm{i}\sigma^y c_{i,2}$) (referred to as the spin and the charge gaps respectively) both vanish at the critical point. A similar unconventional phase transition was also found in 1D systems in Ref. [85], where the gaps also closed in the collective spin/charge excitations rather than in the single particle excitations. This implies that in the low energy limit this quantum phase transition only involves bosonic degrees of freedom, allowing the fermionic excitations to be integrated out from the field theory.

Close to the quantum critical point, we can define a four component unit vector $\boldsymbol{n}$ with $\boldsymbol{n}^2 = 1$, which couples to the fermions as follows:

$$n_1 \hat{N}^x + n_2 \hat{N}^y + n_3 \mathrm{Re}(\hat{\Delta}) + n_4 \mathrm{Im}(\hat{\Delta}). \tag{3.4}$$

We propose that the phase diagram for $\lambda \neq 0$ can be described by the following effective bosonic field theory:

$$S = \int \mathrm{d}^2 x \mathrm{d}\tau \ \frac{1}{g} (\partial_\mu \boldsymbol{n})^2 + \frac{\mathrm{i}\Theta}{\Omega_3} \epsilon_{abcd} n^a \partial_x n^b \partial_y n^c \partial_\tau n^d, \tag{3.5}$$

where $\Omega_3 = 2\pi^2$ is the volume of a three dimensional sphere with unit radius. The field theory Eq. 3.5 can be derived using the same method as Ref. [86], after integrating out the fermions. The phase diagram and renormalization group flow of the $(1+1)d$ analogue of Eq. 3.5 were calculated explicitly in Ref. [87, 88, 89]; and it was demonstrated that the entire phase $0 \leq \Theta < \pi$ is controlled by the fixed point $\Theta = 0$, while the entire phase $\pi < \Theta \leq 2\pi$ will flow to the fixed point $\Theta = 2\pi$. $\Theta = \pi$ is the phase transition between the two phases. The phase diagram of Eq. 3.5 was studied in Ref. [22], and again in the disordered phases (phases with large g) $\Theta = \pi$ is the quantum phase transition between the two phases with $0 \leq \Theta < \pi$ and $\pi < \Theta \leq 2\pi$.

In Eq. 3.5, the fixed point $\Theta = 2\pi$ describes a bosonic symmetry protected topological (SPT) state with U(1)×U(1) symmetry [90], where the two U(1) symmetries correspond to charge and S^z conservation respectively. The boundary of Eq. 3.5 with $\Theta = 2\pi$ is a $(1+1)d$ O(4) NLSM with a Wess-Zumino-Witten term at level $k = 1$, which corresponds to a $(1+1)d$ conformal field theory. In the bulk theory we can define two bosonic rotor fields $b_1 \sim n_1 + in_2$ and $b_2 \sim n_3 + in_4$. b_1 and b_2 carry spin-1 and charge-2 respectively. The fixed point $\Theta = 2\pi$ in Eq. 3.5 implies that a vortex of (n_3, n_4) (2π-vortex of b_2, also π-flux seen by the fermions) carries one b_1 boson; namely a π-flux for fermions carries spin $S^z = 1$, which is precisely consistent with the QSH insulator with spin topological numer 2 [91, 92]. Thus the fixed point $\Theta = 2\pi$ has all the key properties of the QSH insulator phase. At the fixed point $\Theta = 0$, the boundary of Eq. 3.5 is trivial. The phase transition between the quantum spin Hall insulator and the trivial state can be driven by tuning the parameter Θ, where the quantum critical point corresponds to $\Theta = \pi$.

3.4 Spin Topological Number and Green's Function

—

Having mapped out the phase boundaries in the phase diagram, let us discuss the topological properties of the various phases. The gapped ground states of the bilayer honeycomb model in Eq. 3.1 belong to the fermion SPT phases protected by both the charge and the spin U(1) symmetries, which is $\mathbb{Z}$ classified (even with interaction). With this classification, each SPT state is characterized by a quantized topological number, the spin Chern number, in analogy to the TKNN integer for integer quantum Hall states, which can be constructed by the following fermion Green's function [93, 94, 95, 96, 97,

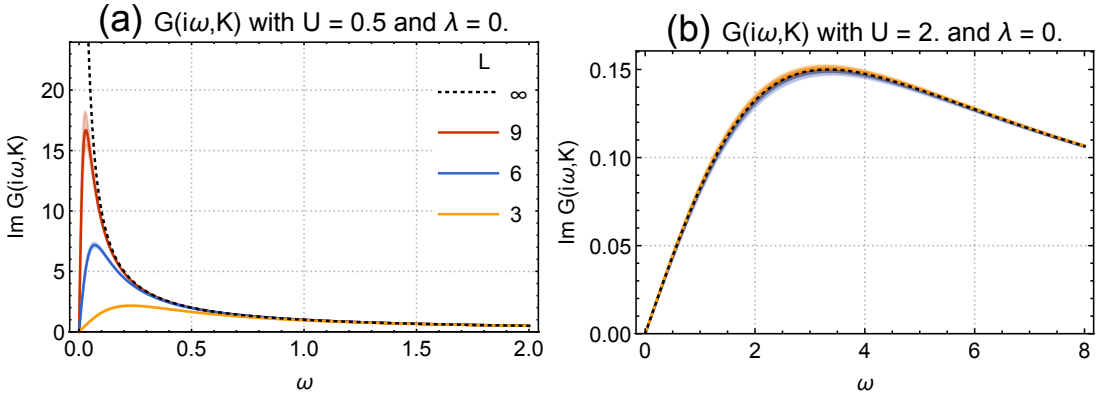

Figure 3.6: Greens function $G(\mathrm{i}\omega, K)$ as a function of frequency at the K point with $\lambda = 0$ and $J/U = 2$ on the bilayer honeycomb lattice for various system sizes. (The largest eigenvalue of $G(\mathrm{i}\omega = 0, K)$ is shown.) **(a)** In the free fermion limit when $U \ll U_c \sim 1.5$, the Green's function shows a pole at zero frequency: $G(\mathrm{i}\omega, K) \simeq 1/(\mathrm{i}\omega)$ [Eq. 3.11] (dotted black line). **(b)** In the strong interacting limit when $U \gg U_c \sim 1.5$, the Green's function follows the behavior of $G(\mathrm{i}\omega, K) \simeq (\mathrm{i}\omega)/((\mathrm{i}\omega)^2 - \Delta^2)$ (as calculated in the appendix Eq. 3.12) (dotted black line) where Δ is the quasi-particle gap. Please note that here ImG is the imaginary part of the imaginary-time Green's function, which is very different from the spectral function.

98, 99, 100] as

$$C_s = \frac{1}{48\pi^2} \int \mathrm{d}^3 k \epsilon^{\mu\nu\lambda} \mathrm{Tr}[-\sigma^z G \partial_\mu G^{-1} G \partial_\nu G^{-1} G \partial_\lambda G^{-1}], \tag{3.6}$$

where σ^z is the spin S^z matrix, $G(k) = -\langle c_k c_k^\dagger \rangle$ is the fermion Green's function in the frequency and momentum space $k = (i\omega, \boldsymbol{k})$ with $i\omega$ being the Matsubara frequency, and ∂_μ here stands for $\partial/\partial k_\mu$. In the non-interacting limit, the physical meaning of the topological number Eq. 3.6 is associated to the spin Hall conductance $\sigma_H^{\mathrm{spin}} = C_s e/2\pi$. Nevertheless, the formula Eq. 3.6 is still well-defined for interacting systems, as long as we use the full interacting fermion Green's function [93, 94, 97, 98, 99, 100]. However, for interacting systems, this topological number defined with full Green's function no longer necessarily corresponds to the spin Hall response.

In the weak interaction regime, the spin topological number for the bilayer QSH state is $C_s = \pm 2$, depending on the sign of λ. The two QSH phases are separated by a topological phase transition at $\lambda = 0$ (the red line in Fig. 3.2), where the single-particle

gap closes, and the Green's function develops poles at zero frequency and at the K and K' points in the Brillouin zone. Due to this singularity of the Green's function, the spin topological number is allowed to change across the gapless phase boundary. Above the critical point U_c, this phase transition is gapped out by interaction, but the topological number Eq. 3.6 still changes discontinuously across $\lambda = 0$, as proven in Ref. [101]. The transition of the topological number (dashed violet line in Fig. 3.2) hidden in the trivial gapped phase implies that the Green's function must have zeros (instead of poles) at zero frequency. This is based on the observation that in Eq. 3.6 G and G^{-1} are interchangeable, so the topological number can either change through the poles of G or the zeros of G (which are poles of G^{-1}) [101, 85]. When the fermions are gapped out by strong interaction, it is impossible to have poles of G at zero frequency, so the topological number Eq. 3.6 can only change through the zeros of G.

The zeros of the Green's function is a prominent property of the trivial gapped phase ($U > U_c$), in contrast to the poles along the topological phase boundary ($U < U_c$). It is found that both the poles and the zeros are located at the K and K' points in the Brillouin zone, and can be verified in our QMC simulation. Along the $\lambda = 0$ axis, the Green's function at K point $G(\omega, K)$ develops a pole as $\omega \to 0$ when $U < U_c$ [Fig. 3.6(a)]; while it approaches zero when $U > U_c$ [Fig. 3.6(b)]. In the strong interaction limit, Ref. [101] predicts that the Green's function should follow the behavior $G(\omega, K) \simeq \omega/(\omega^2 + \Delta^2)$ (where $\Delta \sim U$ is the typical scale of the quasi-particle gap), and in the zero frequency limit $G(\omega, K) \propto \omega$ approaches to zero linearly with ω. Our numerical result matches all these predictions quite well.

3.5 Summary

—

In this chapter we demonstrate that there exist two novel continuous quantum phase transitions for 16 copies of $(2+1)d$ Majorana fermions; both cases are very different from the Standard Gross-Neveu model and Ginzburg-Landau theory. However, a controlled analytical field theory calculation for the critical exponents is not known yet; we will leave this to future studies.

3.6 Permissions and Attributions

The content of this chapter is the result of a collaboration with Yi-Zhuang You and Cenke Xu, and has previously appeared in [102]. We acknowledge support from the Center for Scientific Computing at the CNSI and MRL: an NSF MRSEC (DMR-1121053) and NSF CNS-0960316. The authors are supported by the the David and Lucile Packard Foundation and NSF Grant No. DMR-1151208.

3.A Mean-Field Energy of Order Parameters

In this appendix, we will investigate the order parameters that are favored at the mean-field level. Since our model only has on-site interactions, we will only consider on-site order parameters in this appendix.

We start from the free fermion limit. In momentum space, the fermion kinetic Hamiltonian takes the following form

$$T+T'=\sum_{\boldsymbol{k}}\sum_{\ell=1,2}\begin{bmatrix}c^\dagger_{\boldsymbol{k}A\ell} & c^\dagger_{\boldsymbol{k}B\ell}\end{bmatrix}\begin{bmatrix}g(\boldsymbol{k})\sigma^z & f^*(\boldsymbol{k})\\ f(\boldsymbol{k}) & -g(\boldsymbol{k})\sigma^z\end{bmatrix}\begin{bmatrix}c_{\boldsymbol{k}A\ell}\\ c_{\boldsymbol{k}B\ell}\end{bmatrix}, \tag{3.7}$$

where A and B label the sublattice sites in each unit cell, $g(\boldsymbol{k}) = -2\lambda\big(\sin\sqrt{3}k_x - 2\sin\frac{\sqrt{3}k_x}{2}\cos\frac{3k_y}{2}\big)$, and $f(\boldsymbol{k}) = -t\big(e^{-\mathrm{i}k_y}+2e^{\mathrm{i}k_y/2}\cos\frac{\sqrt{3}k_x}{2}\big)$. Let us first switch to the

Majorana fermion basis

$$\chi_{\boldsymbol{k}} = (\underset{\text{valley}}{c}) KK' \otimes (\underset{\text{sublattice}}{c}) AB \otimes (\underset{\text{layer}}{c}) 12 \otimes (\underset{\text{spin}}{c}) \uparrow \downarrow \otimes (\underset{\text{particle-hole}}{c}) \operatorname{Re} c_{\boldsymbol{k}} \operatorname{Im} c_{\boldsymbol{k}}, \tag{3.8}$$

then expand the kinetic Hamiltonian $T+T'$ around the $K = (+\frac{4\pi}{3\sqrt{3}}, 0)$ and $K' = (-\frac{4\pi}{3\sqrt{3}}, 0)$ points in the Brillouin zone,

$$T + T' = \frac{1}{2} \sum_{\boldsymbol{k}} \chi^{\intercal}_{-\boldsymbol{k}} (v k_x \sigma^{31000} + v k_y \sigma^{02002} + m \sigma^{33032}) \chi_{\boldsymbol{k}}, \tag{3.9}$$

where $\sigma^{ijk\cdots} \equiv \sigma^i \otimes \sigma^j \otimes \sigma^k \otimes \cdots$ stands for the direct product of Pauli matrices, $v = 3t/2$, and $m = 3\sqrt{3}\lambda$. We consider all the fermion bilinear orders $\Delta^{v\alpha\ell\sigma\psi} = \chi^{\intercal} \sigma^{v\alpha\ell\sigma\psi} \chi$ that can gap out the fermions at the K and K' points to gain a kinetic energy benefit, implying that $\sigma^{v\alpha\ell\sigma\psi}$ must be a 32×32 anti-symmetric matrix that anti-commutes with both σ^{31000} and σ^{02002}. We found 136 such matrices that are qualified as the fermion mass terms.

Next we consider the interaction effect. Among the 136 potential orders, the interaction W will select out the most favorable ones. To determine the most favorable orders, we calculate the mean-field (Hartree-Fock) energy of W for the potential orders $\Delta^{v\alpha\ell\sigma\psi}$, *s.t.* the interaction term decomposes into that ordering channel as $W = w_{v\alpha\ell\sigma\psi} |\Delta^{v\alpha\ell\sigma\psi}|^2$ with the mean-field energy $w_{v\alpha\ell\sigma\psi}$. The orders that can gain an interaction energy benefit (*i.e.* $w_{v\alpha\ell\sigma\psi} < 0$ given $U, J > 0$) are concluded in Tab. 3.1: the layer-antiferromagnetic spin density wave, the inter-layer exciton order, and the inter-layer spin-singlet pairing order. When $\lambda \neq 0$, the λ term suppresses the exciton order and the z-component of the spin density wave. As a result, when $\lambda \neq 0$ we only consider the XY component of the Neel order and the pairing order, which exactly corresponds to the four component vector $\boldsymbol{n}$ defined in Eq. 3.4.

Table 3.1: Mean-field energy of the interaction favored fermion bilinear orders. When $J/U = 2$, there is an $SO(5)$ symmetry which mixes mix the spin density wave and exciton order parameters so that these order parameters transform like a vector with $n = (\Delta^{03312}, \Delta^{03320}, \Delta^{03332}, \Delta^{03200}, \Delta^{03102})$. The degeneracy of the mean-field energies of the exciton order and the pairing order is not associated to a symmetry.

$w_{v\alpha\ell\sigma\psi}$	$\Delta^{v\alpha\ell\sigma\psi}$	physical meaning
$-(J+2U)/4$	Δ^{03312} Δ^{03320} Δ^{03332}	layer-antiferromagnetic s-wave spin density wave
$-J/2$	Δ^{03102} Δ^{03200}	inter-layer s-wave exciton order
$-J/2$	Δ^{10121} Δ^{10123}	inter-layer spin-singlet s-wave superconductivity

3.B Green's Function in Both Free and Strong Interacting Limits

In this appendix, we will calculate the fermion Green's function analytically in both the free and the strong interacting limits. Suppose that in the Majorana basis, the kinetic Hamiltonian takes the most general fermion bilinear form $T + T' = \sum_{a,b} \mathrm{i} u_{ab} \chi_a \chi_b$, where a & b are the combined label of site, layer, spin, and particle-hole indices; and χ_a & χ_b are the corresponding Majorana fermion operators. The full Hamiltonian $H = T + T' + W$ also includes the interaction term $W = \sum_i \sum_{[\alpha_k]} w_{\alpha_1\alpha_2\alpha_3\alpha_4} \chi_{i\alpha_1} \chi_{i\alpha_2} \chi_{i\alpha_3} \chi_{i\alpha_4}$, where i labels the site and α_k labels the rest of the internal degrees of freedoms.

Consider the fermion Green's function, which is defined as $G_{ab} = -\langle \chi_a \chi_b \rangle$. In the free fermion limit, the Green's function can be simply obtained from the single-particle Hamiltonian via $(G^{-1})_{ab} = \mathrm{i}\omega\delta_{ab} - \mathrm{i}u_{ab}$. In momentum space (expanded around the K and K' points) and using the Majorana basis, the kinetic Hamiltonian reads (see the previous appendix section),

$$T + T' = \frac{1}{2} \sum_{\boldsymbol{k}} \chi^{\intercal}_{-\boldsymbol{k}} (v k_x \sigma^{31000} + v k_y \sigma^{02002} + m \sigma^{33032}) \chi_{\boldsymbol{k}}. \tag{3.10}$$

So in the free fermion limit, the Green's function is

$$\begin{aligned} G(\mathrm{i}\omega, \boldsymbol{k}) &= (\mathrm{i}\omega\sigma^{00000} - vk_x\sigma^{31000} - vk_y\sigma^{02002} - m\sigma^{33032})^{-1} \\ &= \frac{\mathrm{i}\omega\sigma^{00000} + vk_x\sigma^{31000} + vk_y\sigma^{02002} + m\sigma^{33032}}{(i\omega)^2 - (v^2\boldsymbol{k}^2 + m^2)}, \end{aligned} \tag{3.11}$$

where $v = 3t/2$ and $m = 3\sqrt{3}\lambda$ are determined by the hopping parameters. While in the strong interacting limit, the Green's function (at low frequency limit) has the form

$$\begin{aligned} G(\mathrm{i}\omega, \boldsymbol{k}) &\simeq \frac{\mathrm{i}\omega\sigma^{00000} + \sum_{n=0}^{\infty} g_n \left(vk_x\sigma^{31000} + vk_y\sigma^{02002} + m\sigma^{33032}\right)^{2n+1}}{(i\omega)^2 - \Delta^2} + O(\omega^2) \\ &= \frac{\mathrm{i}\omega\sigma^{00000} + \sum_{n=0}^{\infty} g_n \left(v^2\boldsymbol{k}^2 + m^2\right)^n (vk_x\sigma^{31000} + vk_y\sigma^{02002} + m\sigma^{33032})}{(i\omega)^2 - \Delta^2} + O(\omega^2), \end{aligned} \tag{3.12}$$

where g_n are coefficients and the single-particle gap $\Delta = U/2 + 3J/4$ is determined by the interaction parameters. In our QMC simulation, we set $J = 2U$, so $\Delta = 2U$ in the $U \to \infty$ limit. However for finite U in our simulation, the single particle gap Δ should generally be softer ($\Delta < 2U$). As one can see, Eq. 3.12 has the same structure on the numerator as Eq. 3.11, so they should result in the same topological number. It is also found that $g_0 = 0$ for our model; however, this does not affect the topological number.

At the K (or K') point, we set $\boldsymbol{k} = 0$. Thus from the above results, we conclude that along the $\lambda = 0$ axis ($s.t.\ m = 0$) and below $U_c \sim 1.5$, the Green's function shows a pole at zero frequency: $G(\mathrm{i}\omega, K) \simeq 1/(\mathrm{i}\omega)$ [Fig. 3.6(a)]; while above U_c, the Green's function follows the behavior of $G(\mathrm{i}\omega, K) \simeq (\mathrm{i}\omega)/((\mathrm{i}\omega)^2 - \Delta^2)$ [Fig. 3.6(b)], where Δ is the quasi-particle gap. Away from the $\lambda = 0$ axis and at zero frequency, the Green's function is expected to decay as $1/\lambda$ [Fig. 3.7] in the free fermion limit. Our numerical results are perfectly consistent with the predictions made above (see Fig. 3.6, Fig. 3.7).

3.C Continuous Symmetries

In this appendix we study the continuous symmetries of our 2d model, which allow us to simplify our analysis. A summary is given in Tab. 3.2. The symmetries of our model

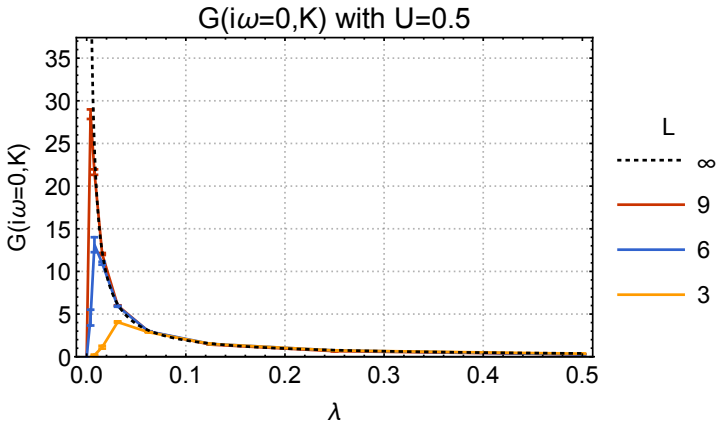

Figure 3.7: Zero frequency Greens function $G(\mathrm{i}\omega = 0, K)$ at the K point with $J/U = 2$ on the bilayer honeycomb lattice for various system sizes. (The largest eigenvalue of $G(\mathrm{i}\omega = 0, K)$ is shown.) In the free fermion limit when $U \ll U_c \sim 1.5$, the Green's function decays as $G(\mathrm{i}\omega = 0, K) \simeq 1/3\sqrt{3}\lambda$ (c.f. Eq. 3.11) (dotted black line).

are easiest to understand in a Majorana basis,

$$\chi_i = (\underset{\text{layer}}{c})\, 12 \otimes (\underset{\text{spin}}{c})\uparrow\ \downarrow \otimes (\underset{\text{particle-hole}}{c})\, \mathrm{Re}\, c_i\, \mathrm{Im}\, c_i. \tag{3.13}$$

Here we have removed the valley and sublattice indices on χ_i, since χ_i is written in the real space on each site i. One can define the following fermion bilinear operators

$$n_i^a = \chi_i^\intercal \gamma^a \chi_i, \text{ with } \boldsymbol{\gamma} = (\sigma^{312}, \sigma^{320}, \sigma^{332}, \sigma^{102}, \sigma^{200}, \sigma^{123}, \sigma^{121}) \tag{3.14}$$

where $n_i^{1,2,3}$ are the spin density wave (SDW) operators, $n_i^{4,5}$ are the exciton order operators and $n_i^{6,7}$ are the superconductivity (SC) pairing operators. In terms of these operators, the interaction term W_i can be written (up to a constant energy shift) as:

$$W_i = \frac{1}{64}\left(A \sum_{a=1,2,3} n_i^a n_i^a + B \sum_{a=4,5} n_i^a n_i^a + C \sum_{a=6,7} n_i^a n_i^a\right), \tag{3.15}$$

where $A = -\frac{2}{3}U$, $B = \frac{1}{6}(2U - 3J)$, $C = \frac{1}{3}U$. Then it becomes obvious that at $J = 2U$, we have $A = B$, such that the SDW and exciton orders are degenerated, and the interaction term has $SO(5) \times SO(2)$ symmetry. There are two other high symmetry points. When

coupling constants	symmetry
$J/U = 2, \lambda = 0$	$U(1)_{\text{charge}} \times SO(5)_{\text{layer charge, SDW} \leftrightarrow \text{exciton, spin}}$
$J/U = 2, \lambda \neq 0$	$U(1)_{\text{charge}} \times SU(2)_{\text{layer charge, z-SDW} \leftrightarrow \text{exciton}} \times U(1)_{\text{z-spin}}$
$J/U \neq 2, \lambda = 0$	$U(1)_{\text{charge}} \times U(1)_{\text{layer charge}} \times SU(2)_{\text{spin}}$
$J/U \neq 2, \lambda \neq 0$	$U(1)_{\text{charge}} \times U(1)_{\text{layer charge}} \times U(1)_{\text{z-spin}}$

Table 3.2: A summary of the symmetries of our model for various coupling constants.

$U = 0$, we have $A = C$, such that the SDW and SC orders are degenerated, and the interaction term has another $SO(5) \times SO(2)$ symmetry. When $J = 0$, we have $B = C$, such that the exciton and SC orders are degenerated, and the interaction term has $SO(4) \times SO(3)$ symmetry. All the symmetry groups can be embedded in the same $SO(7)$ group, generated by operators of the form $\sum_i \frac{1}{8}\chi_i^T \Gamma \chi_i$, where $\Gamma^{ab} = \frac{1}{2\mathrm{i}}[\gamma^a, \gamma^b]$.

Now we take into account the hopping terms. When $J/U = 2$ and $\lambda = 0$, this model has the $U(1) \times SO(5)$ symmetry. The $U(1)$ charge symmetry is generated by Γ^{67} while the $SO(5)$ symmetry is generated by Γ^{ab} (for $a, b = 1, \cdots, 5$) with rotates the SDW and exciton order parameters [Tab. 3.1] like a vector. If $J/U = 2$ but $\lambda \neq 0$ then symmetry is reduced to $U(1) \times U(1) \times SU(2)$. The $U(1)$ symmetries are total charge conservation and spin rotation about the z axis. The $SU(2)$ symmetry is generated by $\Gamma^{34}, \Gamma^{45}, \Gamma^{53}$ (which will mix the S^z SDW and exciton order parameters).

When $J/U \neq 2$ and $\lambda = 0$ the symmetry is $U(1) \times U(1) \times SU(2)$, which corresponds to separate $U(1)$ charge conservation on each layer and $SU(2)$ spin rotation. If $J/U \neq 2$ and $\lambda \neq 0$ then the $SU(2)$ spin rotation symmetry reduces to a $U(1)$ spin rotation symmetry about the z axis.

3.D QMC Methods

The numerical results presented in this paper were calculated using projector quantum Monte Carlo (QMC), which is described in detail in [103]. Projector QMC is a

kind of determinant QMC which focuses on the zero temperature ground states of non-degenerate fermion systems. Determinant QMC is a kind of auxiliary field QMC which uses a (usually discrete) Hubbard-Stratonovich transformation to decouple an interacting fermion Hamiltonian into a noninteracting Hamiltonian. All of these QMC methods are unbiased, controlled, and numerically exact numerical methods to calculate expectation values to arbitrary precision. Ground state expectation values are calculated from the imaginary time evolution of a trial wavefunction $|\Psi_T\rangle$

$$\langle A\rangle = \lim_{\Theta\to\infty} \frac{\langle\Psi_T|e^{-\Theta H/2}Ae^{-\Theta H/2}|\Psi_T\rangle}{\langle\Psi_T|e^{-\Theta H}|\Psi_T\rangle} \tag{3.16}$$

Θ is a projection parameter which projects the trial wavefunction into the ground state. In practice, one must use a finite but large value for Θ. We chose to use $\Theta = 64/t$ (where t is the hopping strength), which we found to be sufficient. As is typically done, we chose $|\Psi_T\rangle$ to be a Slater determinant in the ground state subspace of the noninteracting part of our interacting Hamiltonian ($T + T'$ from Eq. 3.1).

A Trotter decomposition is then applied to the numerator of Eq. 3.16 to separate the exponents into three parts:

$$e^{-\Theta H/2} = \left[e^{-\Delta_\tau (T+T')}e^{-\Delta_\tau H_U}e^{-\Delta_\tau H_J}\right]^{N_\tau} + O(\Delta_\tau)^2$$

where $\Delta_\tau = \Theta/2N_\tau$, H_U is the U term of H, and H_J is the J term of H [Eq. 3.1]. In our simulations we used $N_\tau \approx \Theta\sqrt{N_{\text{sweeps}}}$ so that the systematic errors due to the Trotter decomposition remain negligible compared to the statistical error resulting from the finite number of Monte Carlo sweeps performed: N_{sweeps}. A sweep has occurred after all field variables have been given the chance to update. We used between 64 and 4096 sweeps for the results shown here. All observables have been checked against exact diagonalization simulations on small lattices. The statistical error due to the finite number of sweeps is shown on all plots as error bars which denote one standard deviation (i.e. $\approx 68\%$

confidence). A Hubbard-Stratonovich transformation is then applied to the interacting fermion problem to transform it into a free fermion problem at the expense of adding (discrete) bosonic variables. We used the same Hubbard-Stratonovich as introduced in [83]. The imaginary numbers due to the Kane-Mele λ term are dealt with as described in [104].

3.E Gap Calculation Methods

In this appendix we discuss in more detail how the gaps in Fig. 3.4 and 3.5 are calculated. (We use the same approach that was used in [105].) First, we measure the rate of exponential decay in imaginary time of correlation functions for various order parameters [Fig. 3.8]. (QMC is very efficient at making this measurement.) This decay has the form $\langle Q^\dagger Q\rangle \sim e^{-\tau\Delta+c}$ for large separations in imaginary time (*i.e.* $\tau \gg \Delta^{-1}$) where Δ is the energy gap associated with the order parameter Q. We then extrapolate the finite system size gaps Δ to the gap for a system with infinite size [Fig. 3.9].

3.F Topological Number Calculation Methods

In this appendix we describe how the topological numbers displayed in Fig. 3.3 are calculated from the Greens function. In one dimension, the topological number can be written as

$$N = \frac{1}{2\pi \mathrm{i}} \int \mathrm{d}k \, \mathrm{Tr}[\Sigma G \partial_k G^{-1}] \tag{3.17}$$

where $G = G(\mathrm{i}\omega = 0, k)$ is the zero frequency Greens function and $\Sigma = \sigma^{300}$ in the basis

$$c_i = \underset{\text{sublattice}}{(\,c\,)}\, AB \otimes \underset{\text{layer}}{(\,c\,)}\, 12 \otimes \underset{\text{spin}}{(\,c\,)} \uparrow \downarrow \tag{3.18}$$

To calculate this number using DQMC, we first measure the zero frequency Greens function $G(\mathrm{i}\omega = 0)_k$ at the discrete (due to the finite lattice) momenta k. We then

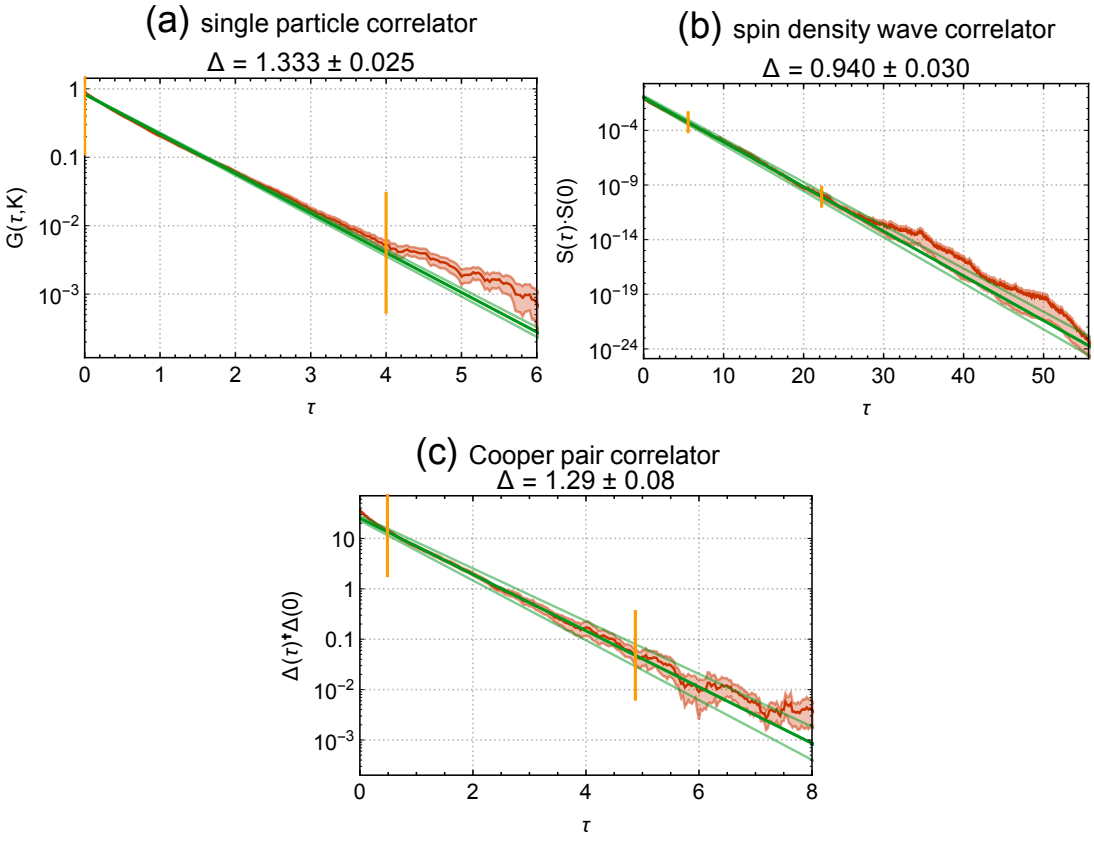

Figure 3.8: The exponential decay in imaginary time of correlation functions (red line) for various order parameters [Tab. 3.1] on a honeycomb lattice of dimension 3x3 with $U = 1.4375$, which is nearly at the critical point. The shaded red region denotes statistical errors. The thick green line indicates the fit to $e^{-\tau\Delta+c}$ while the two thin green lines denote the uncertainty of the fit. The fit was performed in the region between the vertical orange lines. The negative of the slope of the fit is the energy gap for the finite size system, which is used to make Fig. 3.9.

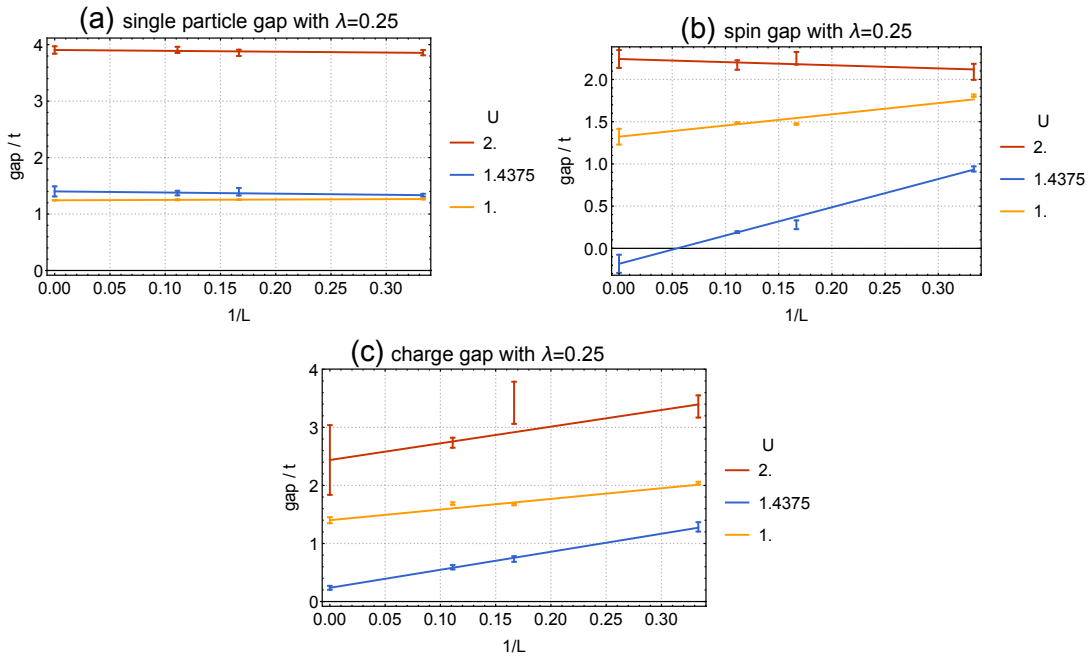

Figure 3.9: We extrapolate the gaps associated with a single particle **(a)**, spin **(b)**, and charge **(c)** [Tab. 3.1] from a system of finite spacial size to one of infinite size. Extrapolations are shown for $\lambda = 0.25$ and interaction strengths below ($U = 1$), near ($U = 1.4375$), and above ($U = 2$) the gapless critical point at $U \sim 1.5$. These results of these extrapolations are used to make Fig. 3.5b ($\lambda = 0.25$ and $J/U = 2$).

promote $G(\mathrm{i}\omega = 0)_k$ to a continuous function $G(\mathrm{i}\omega = 0, k)$ via interpolation. For example, one could choose a linear interpolation

$$G(\mathrm{i}\omega = 0, k) = \frac{k_2 - k}{k_2 - k_1} G(\mathrm{i}\omega = 0)_{k_1} + \frac{k - k_1}{k_2 - k_1} G(\mathrm{i}\omega = 0)_{k_2} \tag{3.19}$$

where k_1 and k_2 are the nearest discrete momenta to the continuous momentum k. The choice of interpolation method will not affect the topological number as long as the the lattice is large enough to sample enough momenta. This is because N is a topological number and therefore insensitive to local perturbations. (Imagine calculating the winding number of a circle around the origin by approximating the circle as a polygon.) Once $G(\mathrm{i}\omega = 0, k)$ has been attained via interpolation, it can be inserted into the equation for N [Eq. 3.17] to attain the topological number via numerical integration.

In two dimensions, the topological number can be written as

$$C_s = \frac{1}{48\pi^2} \int \mathrm{d}\omega \mathrm{d}^2 k \, \epsilon^{\mu\nu\rho} \mathrm{Tr}[\Sigma G \partial_\mu G^{-1} G \partial_\nu G^{-1} G \partial_\rho G^{-1}] \tag{3.20}$$

where $G = G(\mathrm{i}\omega, k)$ is the Greens function and $\Sigma = -\sigma^{003}$ in the same basis as above. Now, we measure $G_{\mathrm{i}\omega,k}$ at discrete Matsubara frequency ω and discrete momenta k and then interpolate it to $G(\mathrm{i}\omega, k)$. However, the measured $G_{\mathrm{i}\omega,k}$ is only reliable up to $\omega \sim 2\pi N_\tau/\Theta$. Since $G(\mathrm{i}\omega, k)$ is expected to approach zero for large ω, we choose to let our interpolation approach zero at a finite $\omega \sim 2\pi N_\tau/\Theta$ and remain at zero for larger ω. Again, this will not affect the calculated topological number as long as N_τ/Θ is sufficiently large. Finally, $G(\mathrm{i}\omega, k)$ is inserted into the equation for C_s [Eq. 3.20] using numerical integration.

Chapter 4

Many-Body Localization of Symmetry Protected Topological States

We address the following question: Which kinds of symmetry protected topological (SPT) Hamiltonians can be many-body localized? That is, which Hamiltonians with an SPT ground state have finite energy density excited states which are all localized by disorder? Based on the observation that a finite energy density state, if localized, can be viewed as the ground state of a local Hamiltonian, we propose a simple (though possibly incomplete) rule for many-body localization of SPT Hamiltonians: If the ground state and top state (highest energy state) belong to the same SPT phase, then it is possible to localize all the finite energy density states; If the ground and top state belong to different SPT phases, then most likely there are some finite energy density states which can not be fully localized. We will give concrete examples of both scenarios. In some of these examples, we argue that interaction can actually "*assist*" localization of finite energy density states, which is counter-intuitive to what is usually expected.

4.1 Introduction

Symmetry protected topological (SPT) states and many-body localization (MBL) are two striking phenomena of quantum many-body physics. A $d-$dimensional SPT state is the ground state of a local Hamiltonian whose $d-$dim bulk is fully gapped and nondegenerate, while its $(d-1)-$dim boundary is gapless or degenerate when and only when the system preserves a certain symmetry G [17, 18]. An SPT state must have "short range entanglement"; meaning that the entanglement entropy of its subsystems scales strictly with the area of the boundary of the subsystem: $\mathcal{S}_A \sim L^{d-1}$ [106], where L is the linear size of the subsystem A. MBL refers to a phenomenon of the entire spectrum of a local Hamiltonian with disorder, including all of the highly excited states with finite energy density. Localization of single particle states under quenched disorder is well-understood [107], and recent studies suggest that localization can survive under interaction [108, 109]. Here, the phrase MBL refers to systems whose all many-body eigenstates are localized, namely the entanglement entropy of all finite energy density states obey the same area law as SPT states instead of the usual volume law typically obeyed by finite energy density states.

These observations imply that in a many-body localized system, any finite energy density state actually behaves like the ground state of a local parent Hamiltonian. Indeed, it was proposed that phenomena such as stable edge states and spontaneous symmetry breaking [110, 111, 112, 106], which usually occur at the ground state of a system, can actually occur in finite energy density states of MBL systems. In fact, we can **define a MBL system as a system for which any finite energy density eigenstate is a short range entangled ground state of a local parent Hamiltonian**. And if the system preserves a certain symmetry, **then any finite energy density state of the MBL system should also obey the classification of SPT states**. Then we can view

energy density ε as a tuning parameter between SPT states. Of course, in the thermodynamic limit, because there are infinite states in an infinitesimal energy density interval $(\varepsilon, \varepsilon + d\varepsilon)$, we expect there exists many $1d$ curves in the spectrum parameterized by ε with one state $|\psi\rangle_\varepsilon$ at each ε, which is the ground state of an effective SPT Hamiltonian H_ε. And on each such curve $|\psi\rangle_\varepsilon$ is (roughly speaking) continuous in the sense that $|\psi\rangle_\varepsilon$ and $|\psi\rangle_{\varepsilon+d\varepsilon}$ are similar (despite being orthogonal), namely physical quantities averaged over the entire system change continuously with ε on this curve. In an ergodic system, the eigenstate thermalization hypothesis [24] implies that most states with similar energy density ε are similar (their reduced density matrices all behave like a thermal density matrix); in a MBL state, although states with the same energy density can in principle be very different, we still expect (assume) that the continuous curves mentioned above exist, although states in different curves can be very different.

Within one of these curves mentioned above, tuning ε is just like tuning between the ground states of local Hamiltonians. Furthermore, by tuning ε there may or may not be a phase transition. In particular, if all excited states belong to the same SPT phase for arbitrary energy density ε, then there does not have to be any quantum phase transition when tuning ε, which implies that all of the excited states have short range correlations and area-law entanglement entropy, *i.e.* all the finite energy density states are localized; on the other hand, if states with different energy density ε on the same curve belong to different SPT phases, then there must be at least one phase transition at certain critical energy on this curve when tuning ε. This phase transition behaves just like an ordinary zero temperature quantum phase transition between different quantum ground states under disorder. For $1d$ systems this "critical" energy density state could be in the "infinite-randomness" phase [113, 114, 115, 116], whose entanglement entropy scales logarithmically with the subsystem size [117], hence it is not fully localized. The existence of the "infinite-randomness" states at finite energy density have already been

observed in Ref. [118].

Due to the fact that in a generic nonintegrable Hamiltonian H, the ground state $|G\rangle$ and top state $|T\rangle$ (highest energy state of H and also ground state of $-H$) are usually the easiest states to analyze, the most convenient way to determine the existence of "critical" states in the spectrum is to check whether the ground and top states belong to the same SPT phase or not. In summary, if $|G\rangle$ and $|T\rangle$ belong to different SPT phases, and if we understand that these two SPT states are separated by one or multiple continuous phase transitions (this will depend on the type of SPT phases $|G\rangle$ and $|T\rangle$ belong to), then there must be some "critical" excited states in the spectrum which cannot be fully localized [1]. We will apply this rule to various examples in the next section.

4.2 Examples

4.2.1 Kitaev's chain: localization

We first apply our argument to the Kitaev's chain:

$$H = \sum_j -\left(t + (-)^j \delta t + \Delta t_j\right) i\gamma_j \gamma_{j+1}, \tag{4.1}$$

where γ_j are Majorana fermions and Δt_j is a random hopping parameter with zero mean and standard deviation $\sigma_{\Delta t}$. The topological superconductor phase ($\delta t > 0$) and the trivial phase ($\delta t < 0$) can both be fully localized by disorder, because for either sign of δt, the ground state $|G\rangle$ and top state $|T\rangle$ both belong to the same phase (we choose the convention that $(2j-1, 2j)$ is a unit cell). This can be seen in the clean limit with

[1] Here, the phrase "SPT states" also includes direct product states, we view direct product states as "trivial" SPT states. So far not all quantum phase transitions between SPT states have been completely studied, and it is possible that some SPT states are separated by a first order transition. Our statement only applies to the cases that $|G\rangle$ and $|T\rangle$ belong to two different SPT phases that we know are separate by a continuous phase transition, for example the transition between the topological superconductor and the trivial state of the Kitaev's chain (Sec. 4.2).

$\Delta t = 0$. In momentum space $H = \sum_k d^x(k)\tau^x + d^y(k)\tau^z$, and $\vec{d}$ is a nonzero O(2) vector in the entire $1d$ Brillouin zone with $\delta t \neq 0$. For either sign of δt, H and $-H$ have the same topological winding number $n_1 = \frac{1}{2\pi}\int dk\ \hat{d}^a \partial_k \hat{d}^b \epsilon_{ab}$; thus $|G\rangle$ and $|T\rangle$ belong to the same phase. Based on our argument, all the finite energy states with either sign of δt can be fully localized by random hopping Δt. The only states not fully localized in the two dimensional phase diagram tuned by ε and δt are located at the critical line $\delta t = 0$. The critical line $\delta t = 0$ is in a "infinite-randomness" fixed point, and it can be understood through the strong disordered real space renormalization group [115, 116, 117, 119, 120, 118].

Here we confirm the conclusions in Ref. [110, 112, 106] that the finite energy density excited states of the Kitaev's chain with $\delta t > 0$ are still "topological". Since the energy level spacing between two eigenstates vanishes in the thermodynamic limit, the best way to determine if an excited state is topological or not is to compute its entanglement spectrum (the system is defined on a periodic 1d lattice). And because the system is noninteracting, we will compute the single-particle entanglement spectrum introduced in Ref. [121] for each excited state. The single-particle entanglement spectrum for the topological phase ($\delta t > 0$) is shown in Fig. 4.1(a), where two zero energy modes can be observed in the spectrum (corresponding to the Majorana zero modes at both entanglement cuts respectively). This topologically non-trivial feature persists for all energy eigenstates in the many-body spectrum, including the ground/top states and the finite energy density states in between. However at the critical line $\delta t = 0$, as shown in Fig. 4.1(b), the zero energy modes are lifted by the long-range entanglement, and the single-particle entanglement levels become gapless around $\epsilon_E = 0$ which leads to the logarithmic scaling of the entanglement entropy.

The Kitaev's chain itself is just a free fermion model. But our argument indicates that under interaction, as long as $|G\rangle$ and $|T\rangle$ are still both in the topological superconductor

phase, all of the excited states can still be localized. Such a generalization is justified given that the non-interacting Anderson localized states can be adiabatically connected to the many-body localized states under interaction, as proven in Ref. [106].

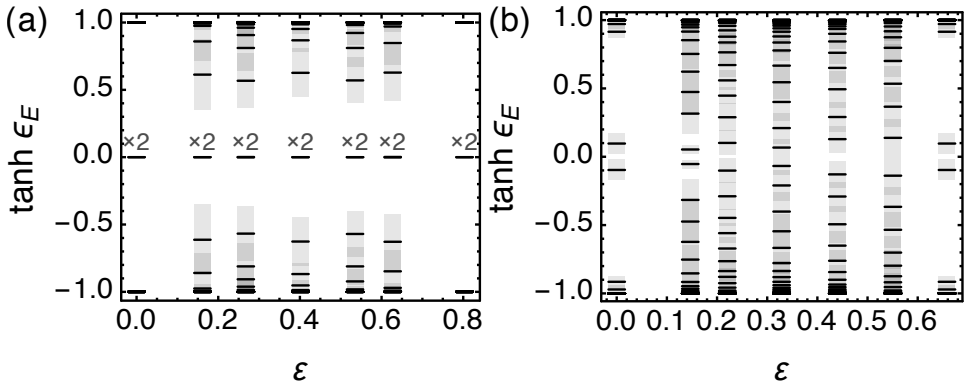

Figure 4.1: Single-particle entanglement spectrum for many-body eigenstates of the random Kitaev's chain, at (a) $\delta t = 0.5t$ and (b) $\delta t = 0$. In both cases $\sigma_{\Delta t} = 0.3t$. We take a 128-site system with periodic boundary condition, which is partitioned into two 64-site subsystems for the entanglement calculation. ϵ_E is the single-particle entanglement energy (s.t. the reduced density matrix $\rho_A = \exp(-c^\dagger \epsilon_E c)$, as shown in Ref. [121]). The spectrum of ϵ_E is shown as $\tanh \epsilon_E$, and is calculated for several many-body eigenstates: including the ground and the top states and other 5 randomly picked finite energy density states, which are arranged in order of their energy density ε. The shading denotes the standard deviation of the entanglement energy levels under a disorder average over the system. Of note are the topologically non-trivial, two-fold degenerate, zero energy modes throughout the entire spectrum ε in the topological phase (a).

4.2.2 Modified Kitaev's chain: critical states and interaction assisted localization

In this subsection we consider a modified Kitaev's chain:

$$H = \sum_j -\left(t - (-1)^j t' \sigma_j^z + \Delta t_j\right) i\gamma_j \gamma_{j+1} - h\sigma_j^z, \tag{4.2}$$

where again Δt_j is random and $t, t', h > 0$. In this model σ_j^z commutes with the Hamiltonian, which implies that any energy eigenstate will also be an eigenstate of σ_j^z. In the

clean limit, the ground state $|G\rangle$ of the system has $\sigma_j^z = 1$ everywhere, and the fermions are in the trivial phase; in contrast, $|T\rangle$ must have $\sigma_j^z = -1$ everywhere, and hence $|T\rangle$ is in the topological superconductor phase. With disorder, both states can be localized, and their entanglement entropy shows the area-law scaling (*i.e.* $\mathcal{S} \sim$ const. for $1d$) as in Fig. 4.2(a). But since the ground state and the top state belong to different SPT phases, based on our argument, there must be some finite energy density states which cannot be fully localized. In this model it is easy to visualize these delocalized excited states. An excited state of the system has a static background configuration of σ_j^z which does not satisfy $\sigma_j^z = 1$. If we consider a random configuration of σ_j^z that has the average $\overline{\sigma_j^z} = 0$, then one can simply absorb σ_j^z into the random numbers Δt_j, and the effective Hamiltonian for Majorana fermions γ_j reads $H_{\text{eff}} = \sum_j -\left(t + \Delta t_j'\right) i\gamma_j\gamma_{j+1}$, which is precisely the random hopping Majorana fermion model Eq. 4.1 tuned to the critical point $\delta t = 0$. And according to Ref. [116, 117], the ground state of H_{eff} (which is a highly excited state of the original Hamiltonian Eq. 4.2 due to the h term) has a power-law correlation after disorder average, and its entanglement entropy scales logarithmically with the subsystem size: $\mathcal{S} \sim \log \ell$ [117]. So the delocalization happens right at the energy scale $E_\sigma \equiv -h \sum_j \sigma_j^z = 0$. In deed our numerical calculation shows that as long as $E_\sigma \neq 0$, the eigen states are all localized with area-law entanglement entropy as in Fig. 4.2(a,b); but for $E_\sigma = 0$, the eigen states are delocalized with logarithmically-scaled entanglement entropy as in Fig. 4.2(c). Thus the model Eq. 4.2 cannot be fully many-body localized, which is consistent with our statement made in the introduction.

The model Eq. 4.2 has a time-reversal symmetry $T : \gamma_j \to (-)^j \gamma_j$ and $\sigma_j^z \to \sigma_j^z$. It is known that with this time-reversal symmetry and without interactions, the Kitaev's chain has $\mathbb{Z}$ classification [77, 78, 79]; that is with an arbitrary number of flavors of Eq. 4.2, $|T\rangle$ is always a nontrivial topological superconductor, while $|G\rangle$ is always a trivial phase. However under certain flavor mixing four-fermion interaction [68, 69], the

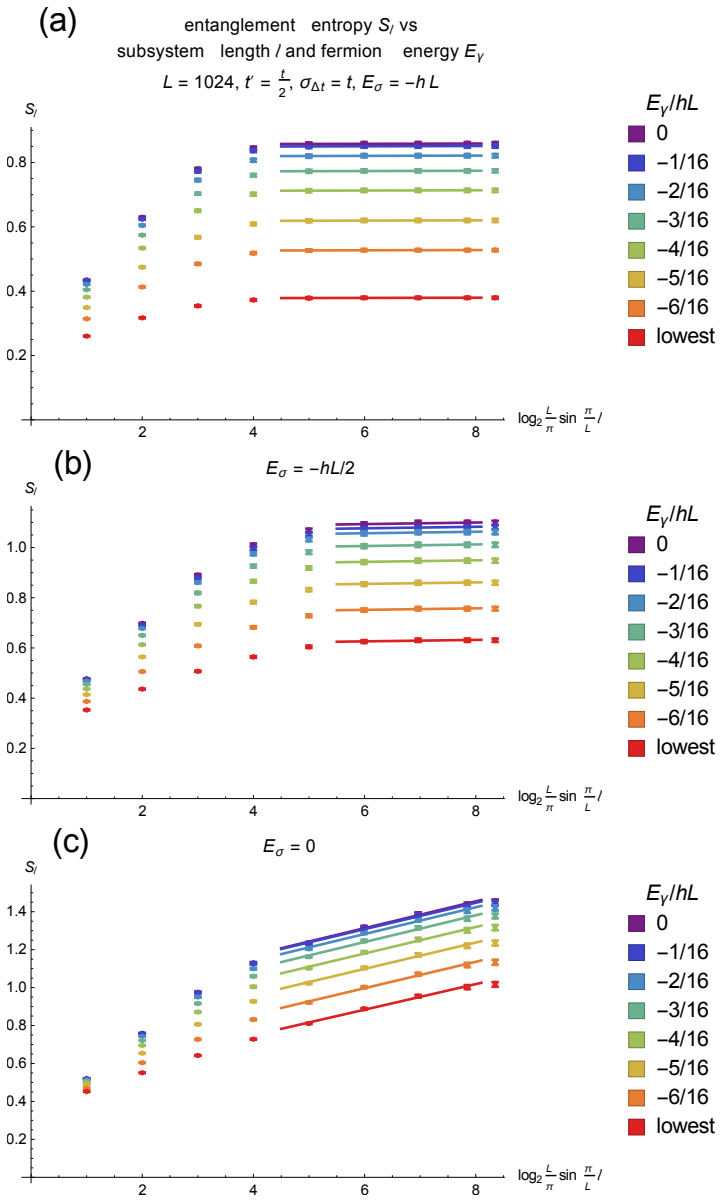

Figure 4.2: Entanglement entropy S_ℓ vs log subsystem length $\log_2 \ell$ vs fermion energy E_γ (energy of the first term in Eq. 4.2) for various boson energies $E_\sigma \equiv -h \sum_j \sigma_j^z = -hL, -hL/2, 0$ (a,b,c) (second term in Eq. 4.2). Calculations are done on a random Majorana chain with $L = 1024$ sites, and the standard deviation of Δt_j is $\sigma_{\Delta t} = t$. States with $E_\sigma = 0$ are the critical excited states which are delocalized. All states with different E_γ at $E_\sigma = 0$ have logarithmic entanglement entropy, and hence are delocalized.

classification of Kitaev's chain with time-reversal symmetry reduces to $\mathbb{Z}_8$. Namely under this four-fermion interaction, for eight copies of Eq. 4.2, $|G\rangle$ and $|T\rangle$ become the same trivial phase, which implies that there does not have to be any phase transition when increasing ε, and all of the finite energy density excited states can be fully localized under the interplay between disorder and interaction.

In model Eq. 4.2, the logarithmic entanglement entropy at the critical excited state comes from the long range effective hopping under renormalization group [115, 116, 117]. We can assume that the four-fermion interaction on each site is random, then when and only when there are $8k$ copies of Eq. 4.2, under interaction each site independently possesses a random set of many-body spectrum *without degeneracy*. Let δV be the typical energy level spacing of the interaction Hamiltonian on each site. To create entangled pairs between distant sites, the effective long-range coupling t_{eff} generated under RG must overcome the energy scale of δV to hybridize the many-body states. However the effective coupling strength actually falls rapidly with the distance[115, 116, 117] as $t_{\text{eff}} \sim te^{-\sqrt{r}}$, so the long-range coupling can only lead to exponentially small entanglement $\Delta\mathcal{S} \sim (t_{\text{eff}}/\delta V)^2 \sim (t/\delta V)^2 e^{-2\sqrt{r}}$. Therefore even with *weak* interaction, all of the eigenstates are short-range entangled area-law states, and can be fully localized. In contrast, without interaction, no matter what kind of fermion-bilinear perturbations we turn on in Eq. 4.2, as long as these terms preserve the time-reversal symmetry defined above and the topological nature of $|G\rangle$ and $|T\rangle$, there must *necessarily* be some finite energy density states which cannot be fully localized. Thus in this case *interaction actually "assists" many-body localization*, which is opposite from what is usually expected for weak interaction, in for example Ref. [122], and is also different from the strong interaction reinforced localization studied in Ref. [123, 124, 125].

Notice that this "interaction assisted localization" is only possible with $8k$ copies of the Kitaev's chain with time-reversal symmetry. With 4 copies of the Kitaev's chain, the

spectrum on each site contains two sets of two-fold degenerate states even under interaction that preserves time-reversal, then the effective long-range coupling t_{eff} generated under RG will still lead to maximal entanglement between distant sites. A detailed RG analysis about this will be given in another paper [126].

4.2.3 Bosonic SPT states, Haldane phase

Many bosonic SPT parent Hamiltonians can be written as a sum of mutually commuting local terms. For example, the "cluster model" for the $1d$ SPT with $Z_2 \times Z_2$ symmetry [112], the Levin-Gu model [127] and the CZX model [128] for the $2d$ SPT states with Z_2 symmetry, and the $3d$ bosonic SPT state with time-reversal symmetry [129] are all a sum of commuting local operators; thus their ground states are a product of eigenstates of local operators [2]. SPT Hamiltonians written in this form are very similar to the "universal" Hamiltonian of MBL state proposed in Ref. [130], which is also a sum of mutually commuting local terms, because a MBL system has an infinite number of local conserved quantities.

All of the idealized SPT models mentioned above have a Z_2 classification, and their ground and top states belong to the same SPT phase. Obviously there should be no phase transition while increasing energy density ε. This statement is still valid with small perturbations which make these models nonintegrable as long as the nature of $|G\rangle$ and $|T\rangle$ are not affected by the perturbations. Thus these models (and their nonintegrable versions) can all be fully localized by disorder.

However, some other bosonic SPT models can not be fully localized. In the following

[2]Ref. [17] actually proposed a general way of constructing parent Hamiltonians for all bosonic SPT states within the group cohomology classification. However, in Ref. [17] the local Hilbert space is labeled by group elements, which implies that for a system with continuous symmetry the local Hilbert space in Ref. [17]'s construction already has infinite dimension, and hence its excited states can also have infinite local energy density. We only discuss systems with a finite dimensional Hilbert space and finite energy density.

we will give one such example for the Haldane phase [131, 132]:

$$H = \sum_j (-1)^j (J + \Delta J_j) \boldsymbol{S}_j \cdot \boldsymbol{S}_{j+1} + \cdots \tag{4.3}$$

$\boldsymbol{S}_j$ are spin-1/2 operators. The ellipsis includes perturbations that break the system's symmetry down to a smaller symmetry (such as time-reversal or $Z_2 \times Z_2$) that is sufficient to protect the Haldane phase, but do not lead to degeneracy in the bulk spectrum, namely only the boundary transforms nontrivially under symmetry. If the random coupling ΔJ_j is not strong enough to change the sign of J, then the ground state and top state of this model correspond to two opposite dimerization patterns of the spin-1/2s. Thus one of them is equivalent to the Haldane's phase while the other is a trivial phase as long as we pick a convention of boundary. If we assume the random Heisenberg coupling ΔJ is sufficient to localize most of the excited states, then there must be an unavoidable phase transition while increasing energy density ε. According to our argument in the introduction, this phase transition should behave just like an ordinary quantum phase transition at zero temperature. It is known that the quantum phase transition between a Haldane phase and a trivial phase is a conformal field theory, and it is equivalent to a spin-1/2 chain without dimerization. With strong disorder, this quantum critical point will be driven into the infinite-randomness spin singlet phase [113, 114, 115, 116] with a power-law decaying disorder averaged spin-spin correlation function and a logarithmic entanglement entropy [117].

4.2.4 $2d$ interacting topological superconductor: critical states and interaction assisted localization

In this subsection we will discuss the nonchiral $2d$ $p \pm ip$ topological superconductor, *i.e.* $p + ip$ pairing for spin-up fermions, and $p - ip$ pairing for spin-down fermions. On a

square lattice this TSC can be written in the Majorana fermion basis:

$$H = \sum_k \chi^t_{-k}(\tau^x \sin k_x + \tau^z\sigma^z \sin k_y)\chi_k + \chi^t_{-k}\tau^y(e - \cos k_x - \cos k_y)\chi_k, \tag{4.4}$$

where $\sigma^z = \pm 1$ represents spin-up and down, while $\tau^z = \pm 1$ represents the real and imaginary parts of the electron operator. Without any symmetry, this system is equivalent to the trivial state, *i.e.* its boundary can be gapped out without degeneracy. However, when $0 < e < 2$, with a Z_2 symmetry which acts as $Z_2 : \chi \to \sigma^z\chi$, the system is a nontrivial TSC. This system can also have another time-reversal symmetry, which is unimportant to our analysis. The boundary of this system reads: $H = \int dx\ \chi^t(-i\partial_x\sigma^z)\chi$, $Z_2 : \chi \to \sigma^z\chi$. The Z_2 symmetry forbids any single particle backscattering at the boundary for arbitrary copies of the system, thus the $p \pm ip$ TSC with the Z_2 symmetry has a $\mathbb{Z}$ classification without interaction.

Without any interaction, for $n-$copies of the $p\pm ip$ TSC, $|G\rangle$ and $|T\rangle$ belong to different SPT phases. This is because for either spin-up or down fermions, the Chern number of $|G\rangle$ and $|T\rangle$ are opposite. And because the system has a $\mathbb{Z}$ classification, $|G\rangle$ and $|T\rangle$ must belong to different SPT states. Using our argument in the introduction, this implies that under disorder that preserves the Z_2 symmetry, there must be some finite energy density states which cannot be fully localized. This is not surprising, considering that even at the single particle level there are likely extended single particle states under disorder. The existence of extended single particle states is well-known in integer quantum Hall state [133], and recently generalized to quantum spin Hall insulator with a $\mathbb{Z}_2$ index [134, 135].

The situation will be very different with interactions. Once again a well-designed interaction will reduce the classification of this $p \pm ip$ TSC from $\mathbb{Z}$ to $\mathbb{Z}_8$ [70, 71, 73, 72]. Namely $n-$copies of Eq. 4.4 is topologically equivalent to $(n + 8k)-$copies. This implies

that under interaction $|G\rangle$ and $|T\rangle$ actually belong to the same phase when $n = 4k$. Thus when $n = 4k$, the phase transition in the noninteracting limit will be circumvented by interaction above a certain critical value. Thus once again interaction *assists* MBL in this case. When $n = 8$, $|G\rangle$ and $|T\rangle$ are both trivialized by interaction, namely interaction can adiabatically connect both states to a direct product of local states. When $n = 4$, Ref. [136] showed that interaction can confine the fermionic degrees of freedom, and drive four copies of the $p \pm ip$ TSC into a $2d$ bosonic SPT state with Z_2 symmetry, which as we discussed in the previous section, can also be fully many-body localized.

Please note that in the noninteracting limit the quantum phase transition between $2d$ TSC and trivial state is described by gapless $(2+1)d$ Majorana fermions, and since a weak short range four-fermion interaction is irrelevant for gapless $(2 + 1)d$ Dirac/Majorana fermions, only strong enough interaction can gap out the quantum phase transition. Thus unlike the $1d$ analogue discussed in Sec. 4.2.2, we expect that in this $2d$ system only strong enough interaction can "assist" disorder and localize all the excited states even for $n = 4k$.

4.3 Summary

In this chapter, we propose a simple rule to determine whether a local Hamiltonian with symmetry can be many-body localized. Since MBL is a phenomenon for the entire spectrum, we need to start with a lattice Hamiltonian for our analysis. Therefore the low energy field theory descriptions and classification of SPT states such as the Chern-Simons field theory [19] and the nonlinear sigma model field theory [90] will not be able to address this question. Instead, our argument is based on the nature of the ground and top states of the same lattice Hamiltonian. Our argument is general enough, that it can be applied to both free and interacting systems, bosonic and fermionic SPT systems.

And counterintuitively, we found that because interactions change the classification of fermionic topological insulators and topological superconductors, in some cases interactions actually assists localization, rather than delocalization.

4.4 Permissions and Attributions

The content of this chapter is the result of a collaboration with Zhen Bi, Yi-Zhuang You, and Cenke Xu, and has previously appeared in [137]. The authors are grateful to Chetan Nayak for very helpful discussions. The authors are supported by the the David and Lucile Packard Foundation and NSF Grant No. DMR-1151208.

Chapter 5

Disordered XYZ Spin Chain Simulations using the Spectrum Bifurcation Renormalization Group

We study the disordered XYZ spin chain using the recently developed Spectrum Bifurcation Renormalization Group (SBRG) [138] numerical method. With strong disorder, the phase diagram consists of three many body localized (MBL) spin glass phases. We argue that, with sufficiently strong disorder, these spin glass phases are separated by marginally many-body localized (MBL) critical lines. We examine the critical lines of this model by measuring the entanglement entropy and Edwards-Anderson spin glass order parameter, and find that the critical lines are characterized by an effective central charge $c' = \ln 2$. Our data also suggests continuously varying critical exponents along the critical lines. We also demonstrate how long-range mutual information introduced in [4] can distinguish these phases.

5.1 Introduction

Quantum phase transitions [139] were previously discussed as transitions between ground states of quantum many-body systems at zero temperature. The conventional wisdom is that highly excited states of a many-body system at finite energy density are typically self-thermalized following the eigenstate thermalization hypothesis (ETH) [140, 24, 141]. However, later it was realized that many-body localized (MBL) systems [142, 23, 143, 28, 144, 25] – typically systems with quenched disorder – can evade thermalization and exhibit robust quantum coherence and non-ergodic dynamics even at finite energy density. The phenomenon of many-body localization (MBL) enables quantum phase transitions to occur at a finite energy density between different MBL quantum phases [145, 146, 147, 148, 149, 150]. The corresponding quantum critical points are marginally localized [151] and are thus known as marginal MBL states (or quantum critical glasses) [152]. Similar to MBL states, marginal MBL states are also non-ergodic, and can be specified by an extensive number of quasi-local integrals of motion (LIOM) [153, 154, 155]. Unlike the typical MBL states, the marginal MBL states exhibit critical behaviors, including the logarithmic scaling of entanglement entropy (in 1D) and the power-law decay of disorder-averaged correlation functions and mutual information.

In this work, we will study the marginal MBL states in a 1D XYZ spin model using the spectrum bifurcation renormalization group (SBRG) numerical method introduced in [138]. SBRG is another version of the excited-state real space renormalization group (RSRG-X) [156, 147, 145, 149], which is specifically designed for the class of MBL models that has a bifurcating spectrum branching structure at each renormalization group (RG) step. The idea of SBRG is similar to RSRG-X, which targets the full many-body spectrum rather than just the ground state. Given a many-body Hamiltonian H with strong disorder, at each RG step, the leading energy scale term (the strongest local term) H_0 in

the Hamiltonian H is first selected, and the whole Hamiltonian H is rotated to the block diagonal basis of H_0. The block off-diagonal terms, which resonate between different H_0 eigen sectors, are treated as perturbations and are reduced to effective terms within the diagonal block via second order perturbation. The RG procedure gradually block diagonalizes the many-body Hamiltonian until it is fully diagonalized. [1] The resulting effective Hamiltonian H_{eff} can be viewed as the RG fixed point Hamiltonian for the MBL system [157, 26, 153, 158, 154], which encodes the full many-body spectrum. The RG transformations can be collected and combined into a unitary quantum circuit U_{RG} (Fig. 5.11, 5.12), which encodes the matrix product state (MPS) approximations for all eigenstates. Various physical properties of the MBL (and marginal MBL) system can be calculated based on the data of H_{eff} and U_{RG} generated by SBRG. Unlike RSRG-X, SBRG does not explicitly choose a specific eigen sector at each RG step. Instead, the spectrum branching is encoded implicitly in the flow of the Hamiltonian, such that the entire spectrum is targeted during each RG flow.

There has been a long history of using the real space renormalization group (RSRG) method to study disordered spin chains.[159, 160, 161, 162, 163] RSRG was originally proposed as a ground state targeting approach, and has been applied to the random Heisenberg,[159] transverse field Ising,[161, 163] XY and XXZ [162] spin chains. It was found that ground states of (clean) quantum critical spin chains (e.g. Ising, XX or Heisenberg) could be unstable to random exchange couplings and flow to the infinite randomness (strong disorder) fixed-point. Whether the critical phenomena of the infinite randomness fixed-point persists at finite energy density is further discussed in the context of MBL using RSRG-X and other methods [147, 149, 145, 164]. The current understanding is that the strong disorder criticality could persist to finite energy density as marginal MBL states in quantum Ising chains. [147] But for (planar) XXZ and Heisen-

[1] See Appendix 5.B for details of the SBRG method.

berg chains, the marginal MBL state is unstable towards thermalization or spontaneous symmetry breaking [149, 164], due to the extensive number of local degeneracies dictated by the symmetry group. Take the random XXZ chain for example, the symmetry group $U(1) \rtimes \mathbb{Z}_2$ is a product of the spin-Z conservation and the spin-flipping $\mathbb{Z}_2$ symmetry. Following the argument given in [165], the symmetric marginal MBL state, if possible, should be characterized by a set of quasi-LIOM, which form irreducible representations of the $U(1) \rtimes \mathbb{Z}_2$ symmetry group. However, the $U(1) \rtimes \mathbb{Z}_2$ symmetry enforces a local degeneracy between states of opposite spin-Z for every quasi-LIOM. As a result, the finite energy density eigenstates in the many-body spectrum are all exponentially degenerate. Because the extensive degeneracy is unstable to quantum fluctuations, the eigenstates must either localize to symmetry breaking spin glass states or thermalize, both of which destroy the quantum criticality.

So to explore marginal MBL phases in 1D spin systems, we must sufficiently break the symmetry to remove all local degeneracies. This motivates us to look at the XYZ spin chain, with independently random XX, YY and ZZ couplings on each bond. The symmetry is broken down to $\mathbb{Z}_2^2$, such that local degeneracies are completely removed (because $\mathbb{Z}_2^2$ has no irreducible representations beyond the one-dimensional representations). Therefore, marginal MBL states of the XYZ spin chain can be stable at finite energy density against thermalization and spontaneous symmetry breaking as long as the disorder is strong enough. Due to the discrete $\mathbb{Z}_2^2$ symmetry, at each RG step there is only one unique leading energy scale term that bifurcates the spectrum. This is precisely the type of model that SBRG was designed to target.

Apart from the above symmetry considerations, strong disorder is another key ingredient to keep the marginal MBL states from thermalizing. We introduce the standard

deviation of the logarithmic scale of the coupling strengths

$$\Gamma = \mathrm{std}(\ln |J|) \tag{5.1}$$

(where J appears as coefficients in the Hamiltonian, e.g. Eq. 5.2) to compare the strength of three often used disorder distributions: uniform, Gaussian, and the power-law distribution which will be used in this work. Physically, Γ describes how much different couplings are separated in their energy scales. Well separbated energy scales in the large Γ limit suppress the resonance between energy levels, and hence hinders thermalization. Our finite-size exact diagonalization (ED) study (Appendix 5.D) indicates that $\Gamma \simeq 1$ is not sufficient to stabilize the marginal MBL phases in the XYZ model against thermalization. Therefore, instead of drawing the coupling strengths from uniform distributions ($\Gamma = 1$) or Gaussian distributions ($\Gamma \approx 1.1$), we need to take power-law distributions (Appendix 5.C.1) whose Γ can be tuned all the way to infinity. We will typically take $\Gamma = 4$ as the initial distribution in our calculation. SBRG is well-suited to study such strong disorder spin systems, as the SBRG algorithm is asymptotically accurate in the large Γ limit.

In the following, we will first introduce the model and present the phase diagram. Then we focus on a high symmetry line in the phase diagram, and investigate the MBL spin glass phase and marginal MBL critical phase in detail. In particular, we calculate the entanglement entropy, Edwards-Anderson correlator and long-range mutual information. We found that the marginal MBL critical line is characterized by an effective central charge $c' = \ln 2$. Our data also suggest continuously varying exponents along the critical line.

5.2 XYZ Spin Chain Model

We study the XYZ spin chain with large disorder and periodic boundary conditions. The Hamiltonian is given by

$$H = \sum_{i=1}^{L} \sum_{\mu=x,y,z} J_{i,\mu}\, \sigma_i^\mu \sigma_{i+1}^\mu. \tag{5.2}$$

σ_i^μ with $\mu = 1, 2, 3$ are Pauli matrix operators on lattice site i of a 1d chain of length L. The couplings $J_{i,\mu} \in [0, J_\mu]$ are randomly drawn from a power-law distribution

$$\mathrm{PDF}(J_{i,\mu}) = \frac{1}{\Gamma J_{i,\mu}} \left(\frac{J_{i,\mu}}{J_\mu} \right)^{1/\Gamma}, \tag{5.3}$$

where $0 < \Gamma < \infty$ (see Eq. 5.1) controls the disorder strength (for details see Appendix 5.C.1). Equivalently, $J_{i,\mu}^{1/\Gamma} \in [0, J_\mu^{1/\Gamma}]$ is uniformly distributed. For later convenience, we define

$$\tilde{J}_\mu \equiv J_\mu^{1/\Gamma}, \tag{5.4}$$

and take $\tilde{J}_\mu = \tilde{J}_x, \tilde{J}_y, \tilde{J}_z$ as our primary tuning parameters (see Appendix 5.C.2 for an explanation). We will be interested in the entire energy spectrum of this model, as opposed to just the low energy states.

Beside the exact global symmetry $\mathbb{Z}_2^2$, the model also has some statistical symmetries, which are valid only in the statistical sense over the ensemble of the disordered Hamiltonians. When $J_x = J_y$ (and similarly for $J_y = J_z$ and $J_z = J_x$), the *distribution* of Hamiltonians H has a $\mathbb{Z}_2$ symmetry which swaps $J_{i,x} \leftrightarrow J_{i,y}$. When $J_x = J_y = J_z$, the distribution of Hamiltonians has an S_3 permutation symmetry which permutes $J_{i,x} \leftrightarrow J_{i,y} \leftrightarrow J_{i,z}$. For any J_μ, the distribution of Hamiltonians also has translation symmetry. Imposing these statistical symmetries can be used to easily fine tune the XYZ model to its critical phases.

In the existing literature, the RSRG-X approach [147, 149, 145, 164] has been successfully applied to analyze various marginal MBL phases in disordered spin systems.

However, it is challenging to apply the traditional closed-form RSRG-X analysis to the XYZ model, even near the free fermion soluble points (such as $J_x = J_y$ and $J_z \to 0$). At the free fermion soluble point, the spin system can be mapped to two independent Majorana chains with uncorrelated randomness, which allows the standard bond decimation RG scheme to be applied independently on each chain. However, once the fermion interactions (J_z terms) are introduced to the system, the two Majorana chains are coupled together as a ladder lattice. The independent bond decimation on both chains will quickly distort the ladder lattice and generate complicated configurations of multi-fermion interactions, which can not be tracked in closed-form. Therefore, we turn to the numerical approach of SBRG, which can keep track of all orders of multi-fermion interactions generated under the RG flow.

In the following, we will study the XYZ model by applying SBRG. We will show results for $\Gamma = 4$ initial randomness, for which SBRG agrees well with exact diagonalization on small latices (data not shown in this paper), and our approximations appear to be safe (see Appendix 5.B.1 and 5.D, and Sec. 5.3.2). We will also limit our system sizes to $L \leq 256$ because our current implementation of SBRG does not produce accurate results for larger system sizes on the critical lines of the XYZ model.

5.3 Phase Diagram

5.3.1 Spin Glass Phases

With large disorder and at finite energy density, there are three spin glass phases (Fig. 5.1). We find that if $\tilde{J}_z$ is the largest coupling constant (i.e. $\tilde{J}_z > \tilde{J}_x$ and $\tilde{J}_z > \tilde{J}_y$), then the system is in an MBL spin glass phase where the correlator $\sigma_i^z \sigma_j^z$ shows long range glassy behavior. That is, $\sigma_i^z \sigma_j^z$ develops a finite overlap with products of the local

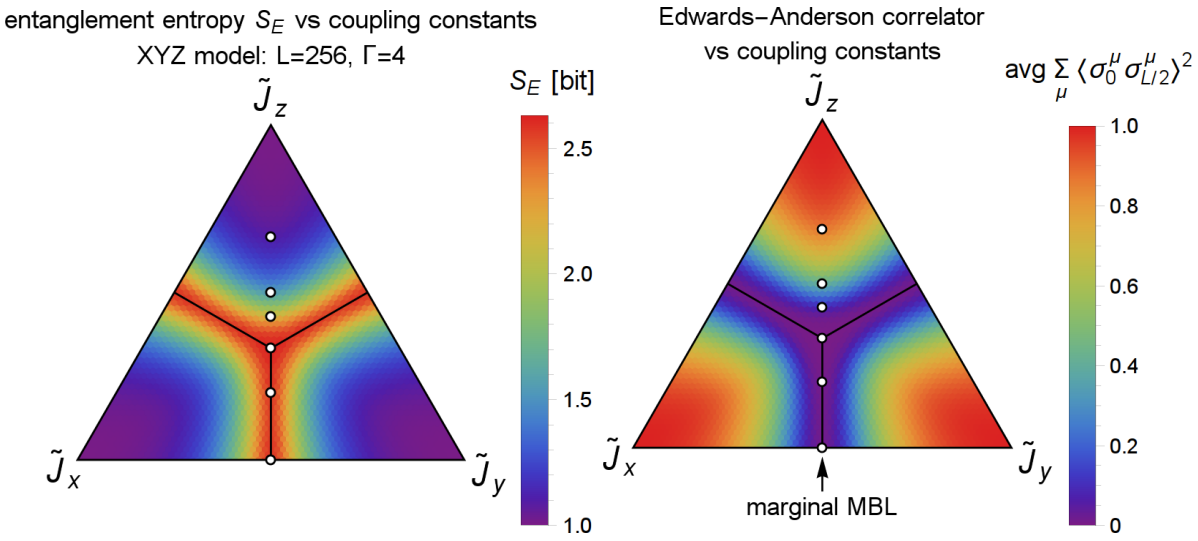

Figure 5.1: Ternary plot of the disorder and energy averaged entanglement entropy S_{E} [bit] ($\equiv S_{\mathrm{E}}/\ln 2$) (Eq. 5.6) of a subsystem of length $L/2$ (top) and Edwards-Anderson correlator (Eq. 5.9) (bottom) vs coupling constants ($0 < \tilde{J}_{x,y,z} < 1$) for the XYZ spin chain of length $L = 256$. We use this plot to sketch the phase diagram. When $\tilde{J}_z > \max(\tilde{J}_x, \tilde{J}_y)$, the system is in a $\mathbb{Z}_2$ spin glass state. When $\tilde{J}_z < \tilde{J}_x = \tilde{J}_y$, the system is in a marginal MBL phase. (The other phases are given by permutations of x, y, z.) The white dots correspond to the points in the phase diagram that are shown in Fig. 5.4, 5.5, 5.7.

integrals of motion (LIOM) τ^zs of the MBL phase (see Eq. 5.12 in Appendix 5.A), and is thus roughly conserved. This finite overlap results in an Edwards-Anderson correlator that asymptotes to a nonzero constant at large distance, which we take to be the primary signature of a spin glass phase.

5.3.2 Critical Phases

With sufficiently strong disorder, the spin glass phases appear to be separated by a critical lines (e.g. $\tilde{J}_z \leq \tilde{J}_x = \tilde{J}_y$) consisting of marginal MBL phases, which is evidenced by the fact that the entanglement entropy diverges logarithmically (Fig. 5.4) in this phase. In Fig. 5.2 we provide evidence that the critical ($\tilde{J}_z \leq \tilde{J}_x = \tilde{J}_y$) to spin glass ($\tilde{J}_z > \tilde{J}_x = \tilde{J}_y$) phase transition is continuous and occurs exactly at $J_x = J_y = J_z$ by showing evidence that the long-range spin glass Edwards-Anderson correlator is zero when $\tilde{J}_z \leq \tilde{J}_x = \tilde{J}_y$ and increases continuously for $\tilde{J}_z > \tilde{J}_x = \tilde{J}_y$. An example of how the LIOM look in this phase is shown in Fig. 5.11.

Marginal MBL vs Thermal

With sufficiently large disorder, SBRG depicts the critical phase as marginally MBL as SBRG finds a logarithmically diverging entanglement entropy in this phase. However, SBRG is not capable of describing thermalization, and so one should worry that resonance effects may thermalize the critical phase. Indeed, the instability of marginal MBL phase to thermalization has been demonstrated in other 1D spin models. [149, 164] Thus, it is crucial to check the approximations made by SBRG, in order to verify that an exact RG does not flow toward thermalization. In Appendix 5.D we do a brief exact diagonalization study to check that with strong disorder, the system is not thermal. Below, we will study the evidence against thermalization by using SBRG.

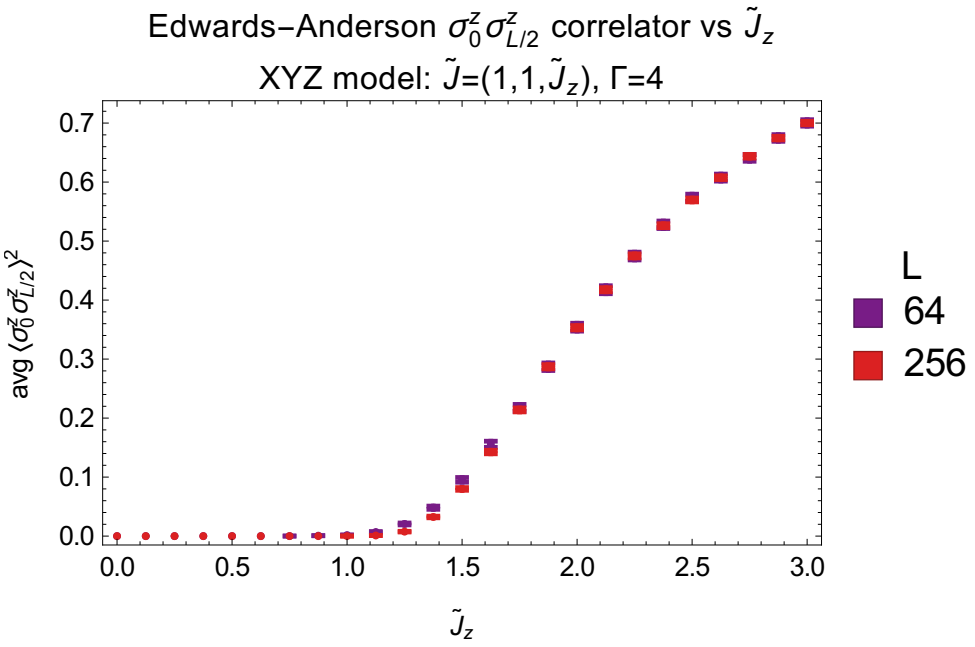

Figure 5.2: Disorder and energy averaged Edwards-Anderson correlator (Eq. 5.9) at separation $x = L/2$ vs $\tilde{J}_z$ for different system sizes L in the XYZ spin chain with $\tilde{J}_x = \tilde{J}_y = 1$. In the critical phase, the Edwards-Anderson correlator decays algebraically to zero; while in the spin glass phase, the Edwards-Anderson correlator asymptotes to a constant. Furthermore, as one tunes $\tilde{J}_z$ from the critical phase to the spin glass phase, the Edwards-Anderson correlator becomes nonzero continuously at $\tilde{J}_z = 1$, indicating that this marks the location of a continuous phase transition. (error bar details: [166])

The core approximation made by SBRG is the validity of the second order perturbation theory used by each RG step. This and other approximations are explained in detail and accounted for in Appendix 5.B.1. However, even though these approximations are controlled by strong disorder, one could still worry that errors may build up during the RG flow and cause SBRG to incorrectly depict the critical phase as a marginal MBL phase, even if the critical phase is actually thermal.

At intermediate RG steps, a cluster of n "LIOM" could resonate and become thermalized by an off-diagonal term that mixes (i.e. anticommutes with) them if the energy of the off-diagonal term ε_{mix} is larger than the smallest energy difference ΔE of the n "LIOM": i.e. if $\varepsilon_{\text{mix}} > \Delta E$. The verified assumptions Eq. 5.14 and 5.15 imply that this rarely occurs for small n. However, one might worry that large clusters of n "LIOM" could be thermalized by rare off-diagonal terms [167]. But a cluster of n LIOM will describe 2^n states, and thus typically have a smallest energy level spacing equal to $\Delta E \sim 2^{-n}$ (because our model has a small symmetry, there is no symmetry protected degeneracy in this cluster); while below we argue that off-diagonal terms at intermediate RG steps will have energies of order $\varepsilon_{\text{mix}} \lesssim e^{-\Gamma n}$, which is much smaller than $\Delta E \sim 2^{-n}$ for large disorder Γ. Thus, $\varepsilon_{\text{mix}} \ll \Delta E$ and so it seems unlikely that enough clusters of n "LIOM" could resonate to thermalize the system.

To show that $\varepsilon_{\text{mix}} \lesssim e^{-\Gamma n}$, we note that at intermediate RG steps, the energies of off-diagonal terms mixing n "LIOM" should be roughly bounded by the the largest n-body coefficient $h^{(n)}_{\text{max}}$ of the effective Hamiltonian H_{eff} (Eq. 5.12): $\varepsilon_{\text{mix}} \lesssim h^{(n)}_{\text{max}}$. And in Fig. 5.3 we show that $h^{(n)}_{\text{max}}$ decays exponentially with $\Gamma\, n$:

$$\begin{aligned} h^{(n)}_{\text{max}} &\equiv \max_{ij\ldots} |h^{(n)}_{ij\ldots}| \\ &\sim e^{-\Gamma n} \end{aligned} \tag{5.5}$$

Thus $\varepsilon_{\text{mix}} \lesssim h^{(n)}_{\text{max}} \sim e^{-\Gamma n}$.

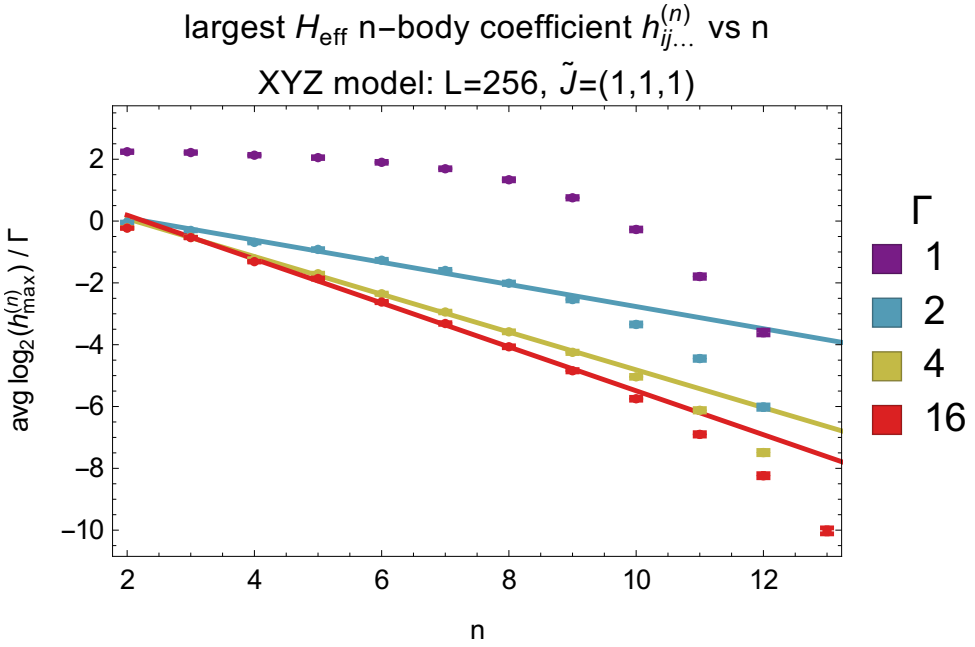

Figure 5.3: Disorder average of $\log_2(h^{(n)}_{\text{max}})/\Gamma$ vs n for different amounts of disorder Γ where $h^{(n)}_{\text{max}} \equiv \max_{ij\ldots}|h^{(n)}_{ij\ldots}|$ (Eq. 5.5) is the largest n-body coefficient $h^{(n)}_{\text{max}}$ of the effective Hamiltonian H_{eff} at the critical point $\tilde{J}_x = \tilde{J}_y = \tilde{J}_z = 1$. As the disorder Γ increases, the data converges to a single straight line. For large n, the data drops below the linear fit line. This is expected to be an artifact of dropping terms in SBRG (see Sec. 5.B.3 for details). Solving for $h^{(n)}_{\text{max}}$ gives $h^{(n)}_{\text{max}} \sim e^{-\Gamma n}$ as in Eq. 5.5, which completes our argument that the critical line is marginally MBL. (error bar details: [166])

5.4 Entanglement Entropy

The entanglement entropy is a useful tool to probe quantum phase transitions from the entanglement patterns of the many-body state, and has the nice property that one does not have to pick the right order parameter. Instead, one only has to choose a useful subsystem geometry. SBRG can efficiently calculate [138] entanglement entropies using the stabilizer rank algorithm introduced by [168].

The entanglement entropy S_{E} of a subsystem A for a wavefunction $|\psi\rangle$ is defined to be

$$S_{\mathrm{E}}(A) \equiv -\operatorname{Tr}[\rho_A \ln \rho_A] \tag{5.6}$$
$$\rho_A = \operatorname*{Tr}_{\overline{A}} |\psi\rangle \langle\psi|$$

where $\operatorname{Tr}_{\overline{A}}$ means that degrees of freedom not in A are traced out. The disorder configuration (δ) and energy (E) averaged entanglement entropy is then

$$\text{avg } S_{\mathrm{E}}(A) \equiv \frac{1}{N_\delta} \sum_\delta \frac{1}{N_E} \sum_E S_{\mathrm{E}}(A) \tag{5.7}$$

where ψ and thus ρ_A in Eq. 5.6 depend on δ and E. We average over all energy eigenstates because we're interested in the entire spectrum of states. Additionally, in the strong disorder limit, the LIOM take the form of products of Pauli matrices, and the eigenstates of these LIOM (and the Hamiltonian) all have the same entanglement entropies. However, this is only a special feature of Pauli-like LIOM in the strong disorder limit. Away from the strong disorder limit, the LIOM will be further dressed by higher order corrections, such that different eigenstates will not have identical entanglement structures. Nevertheless, the difference of entanglement entropies across the spectrum will be relatively small in the strong disorder regime. So we will neglect the spectral dependence, and consider the energy averaged entanglement entropy.

First, we will take the subsystem A to be a line segment of length ℓ. We will be interested in how the entanglement entropy scales as the subsystem length ℓ increases. Later, in Sec. 5.6 we will use more complicated subsystem geometries in order to study the long range mutual information of the XYZ model. As shown in Fig. 5.4, in the spin glass phases, the entanglement entropy S_{E} asymptotes to a constant with increasing subsystem length ℓ since it is a short range correlated phase. Furthermore, $S_{\mathrm{E}} \geq \ln 2$ due to the spin glass order. These results can be understood deep in the spin glass phase via the LIOM in Eq. 5.28 from the stabilizer rank algorithm. [168, 138] See Appendix 5.E for details.

In the critical phases, the entanglement entropy S_{E} appears to diverge logarithmically with subsystem length ℓ (Fig. 5.4):

$$S_{\mathrm{E}}(\ell) = \frac{c'}{3} \ln \ell \tag{5.8}$$
$$c' = \ln 2$$

The constant c' is the effective central charge, which is postulated to be related to the central charge c without disorder by $c' = c \ln 2$ [169] (for Ising and Heisenberg types of models). Without disorder, the XYZ model has $c = 1$ in the critical phase, and so we expect and observe $c' = \ln 2$ in our disordered model (Fig. 5.4). The logarithmically diverging entanglement entropy in Eq. 5.8 is a result of the LIOM becoming nonlocal (see Fig. 5.11). This causes more LIOM to be cut by the subsystem A and enter the entanglement entropy equation Eq. 5.29.

5.5 Edwards-Anderson Correlator

A common approach to characterize glassy order is the Edwards-Anderson correlator. The disorder and energy averaged Edwards-Anderson spin glass correlator of $\sigma_0^\mu \sigma_x^\mu$ is

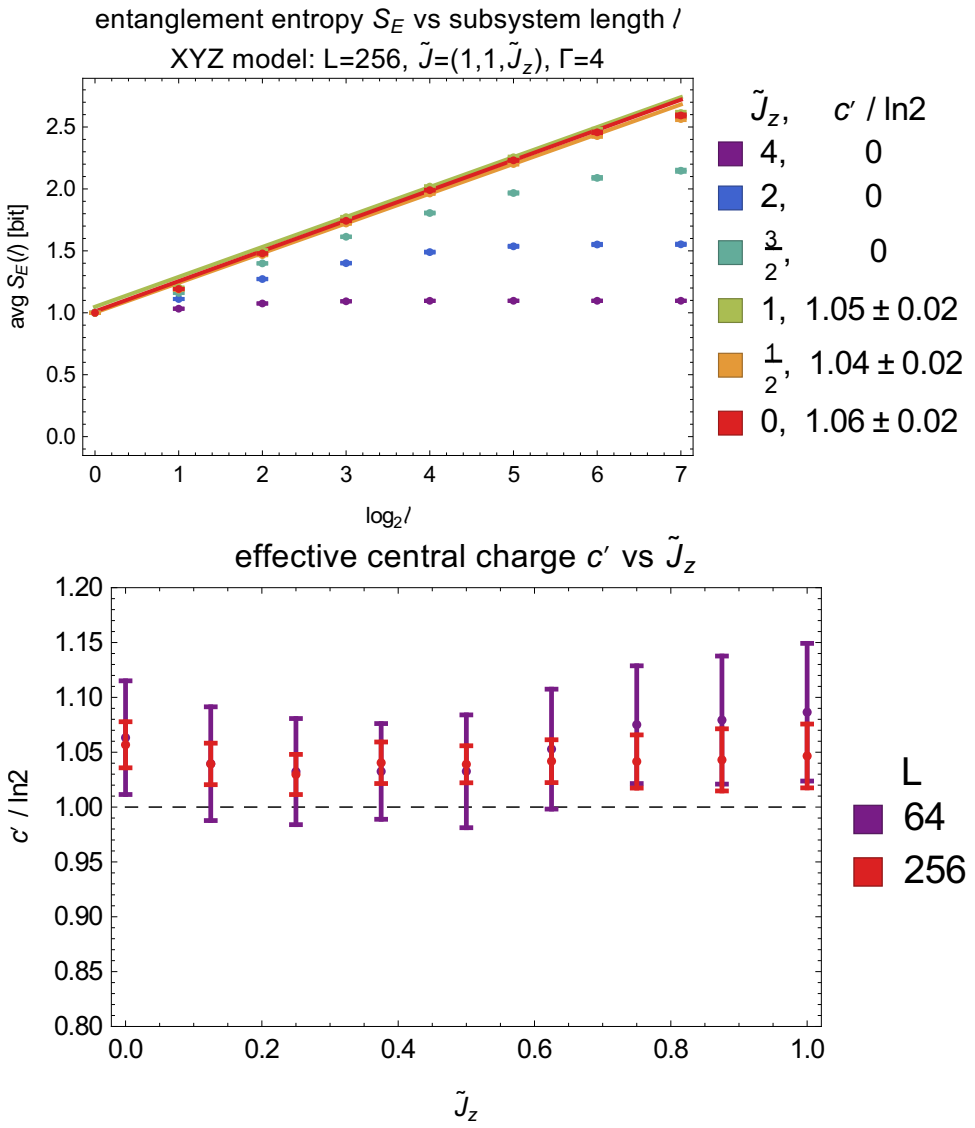

Figure 5.4: **(top)** Disorder and energy averaged entanglement entropy S_{E} [bit] ($\equiv S_{\mathrm{E}}/\ln 2$) (Eq. 5.6) vs subsystem length ℓ for different $\tilde{J}_z$ in the XYZ spin chain with $\tilde{J}_x = \tilde{J}_y = 1$ and system size $L = 256$. When $\tilde{J}_z > 1$, the system is a spin glass and the entanglement entropy follows an area law for large subsystems. When $\tilde{J}_z$ is only slightly larger than 1, e.g. $\tilde{J}_z = 3/2$, there appears to be large finite size effects. When $\tilde{J}_z \leq 1$, the system is critical and the entanglement entropy follows a log law $S_{\mathrm{E}}(\ell) \sim \frac{c'}{3} \ln \ell$, and the effective central charge c' is estimated using the slope of the fit to the $\ell = \frac{1}{2}\sqrt{L}, \sqrt{L}, 2\sqrt{L}$ data points. **(bottom)** Effective central charge c' (Eq. 5.8) vs $\tilde{J}_z$ for different system sizes L in the XYZ spin chain with $\tilde{J}_x = \tilde{J}_y = 1$. For all $\tilde{J}_z < 1$, the effective central charge appears to be consistent with $c' = c \ln 2$ [169] where $c = 1$ is the central charge without disorder. (error bar details: [166])

defined to be

$$\text{avg}\,\langle\sigma_0^\mu\sigma_x^\mu\rangle^2 \equiv \frac{1}{N_\delta}\sum_\delta \frac{1}{N_E}\sum_E \langle E|\sigma_0^\mu\sigma_x^\mu|E\rangle_\delta^2 \tag{5.9}$$

It is the average of the square of $\langle\sigma_0^\mu\sigma_x^\mu\rangle$ over disorder configurations (δ) and energies (E). σ_0^μ and σ_x^μ are Pauli matrices at lattice sites 0 and x, respectively. We average over all energy eigenstates because we're interested in the entire spectrum of states. Additionally, in the strong disorder limit, the LIOM take the form of products of Pauli matrices, and the eigenstates of these LIOM (and the Hamiltonian) all have the same Edwards-Anderson Correlators.

If $\tilde{J}_z > \tilde{J}_x$ and $\tilde{J}_z > \tilde{J}_y$, the system is in a $\sigma^z\sigma^z$ spin glass phase and the $\sigma^z\sigma^z$ Edwards-Anderson correlator (Eq. 5.9) asymptotes to a constant for large distance x (with exponentially small corrections) (Fig. 5.5). Physically, this implies that $\sigma_i^z\sigma_j^z$ has developed a finite overlap with products of the local integrals of motion (LIOM) (Eq. 5.12) of the MBL phase, and is thus roughly conserved. However, the $\sigma^x\sigma^x$ and $\sigma^y\sigma^y$ correlators decay exponentially with distance x, as expected.

When $\tilde{J}_z < \tilde{J}_x = \tilde{J}_y$, the system is in a marginal MBL critical phase between $\sigma^x\sigma^x$ and $\sigma^y\sigma^y$ spin glasses (Fig. 5.1). The spin configuration in the marginal MBL state is dominated by nested domains of $\sigma^x\sigma^x$ and $\sigma^y\sigma^y$ Ising spin glass orders. The domains have fractal structures throughout the lattice, leading to the power-law decay of $\sigma^\mu\sigma^\mu$ Edwards-Anderson correlators (μ summation not implied) with critical exponents η_{xy} and η_z (Fig. 5.6):

$$\begin{aligned}\text{avg}\,\langle\sigma_0^x\sigma_x^x\rangle^2 = \text{avg}\,\langle\sigma_0^y\sigma_x^y\rangle^2 &\sim x^{-\eta_{xy}}\\ \text{avg}\,\langle\sigma_0^z\sigma_x^z\rangle^2 &\sim x^{-\eta_z}\end{aligned} \tag{5.10}$$

Unlike the effective central charge c' (Eq. 5.8) which remains fixed, η_{xy} (η_z) appears to increase (decrease) continuously with increasing $\tilde{J}_z$. The power-law decay of $\sigma^z\sigma^z$ can

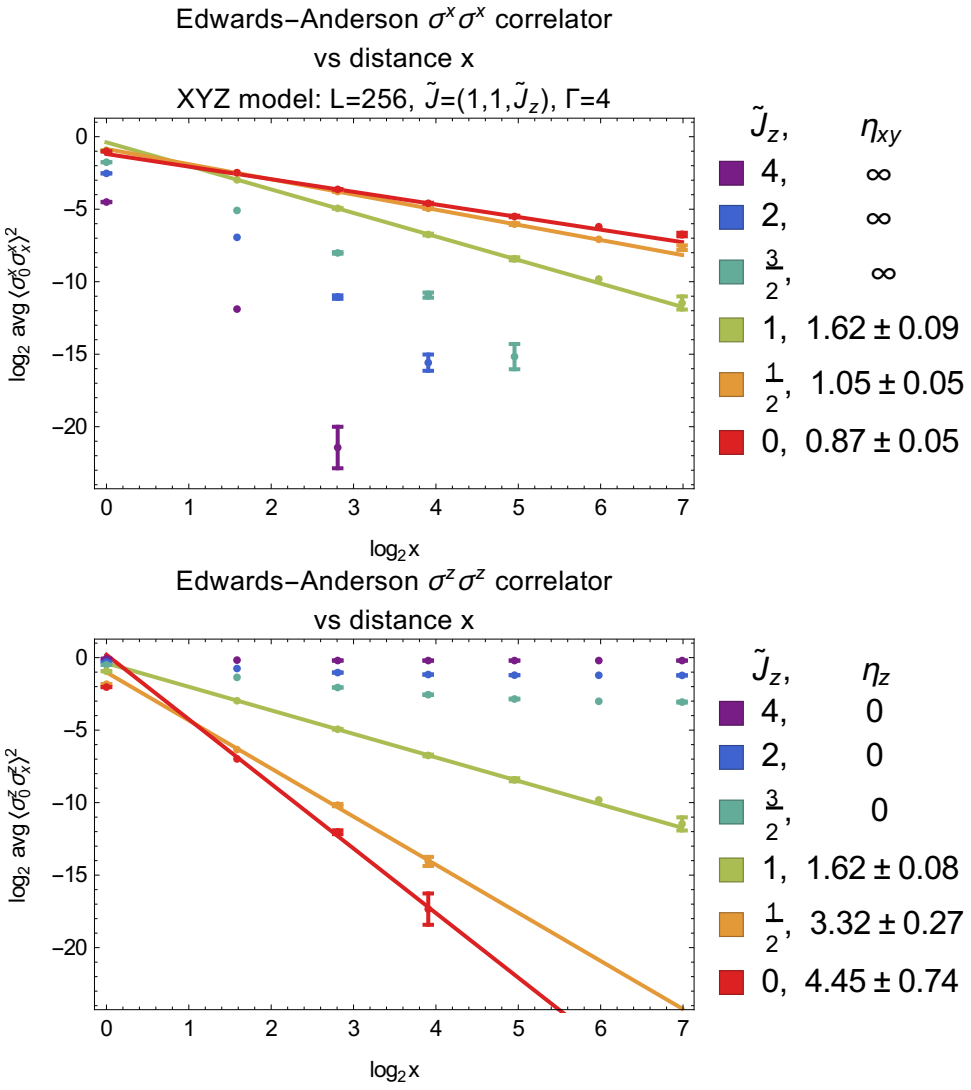

Figure 5.5: Disorder and energy averaged Edwards-Anderson $\sigma^x\sigma^x$ (top) and $\sigma^z\sigma^z$ (bottom) correlators (Eq. 5.9) vs distance x for different $\tilde{J}_z$ in the XYZ spin chain with $\tilde{J}_x = \tilde{J}_y = 1$ and system size $L = 256$. When $\tilde{J}_z > 1$, the system is a $\sigma^z\sigma^z$ spin glass phase, and the $\sigma^x\sigma^x$ correlator decays exponentially while the $\sigma^z\sigma^z$ correlator asymptotes to a constant. When $\tilde{J}_z$ is only slightly larger than 1, e.g. $\tilde{J}_z = 3/2$, there appears to be moderate finite size effects. When $\tilde{J}_z < 1$, the system is critical with power law $\sigma^\mu\sigma^\mu$ correlators (μ summation not implied) with critical exponents η_{xy} and η_z (Eq. 5.10, Fig. 5.6), which were calculated using the slope of the fit to the $x = \frac{1}{2}\sqrt{L} - 1, \sqrt{L} - 1, 2\sqrt{L} - 1$ data points. (error bar details: [166])

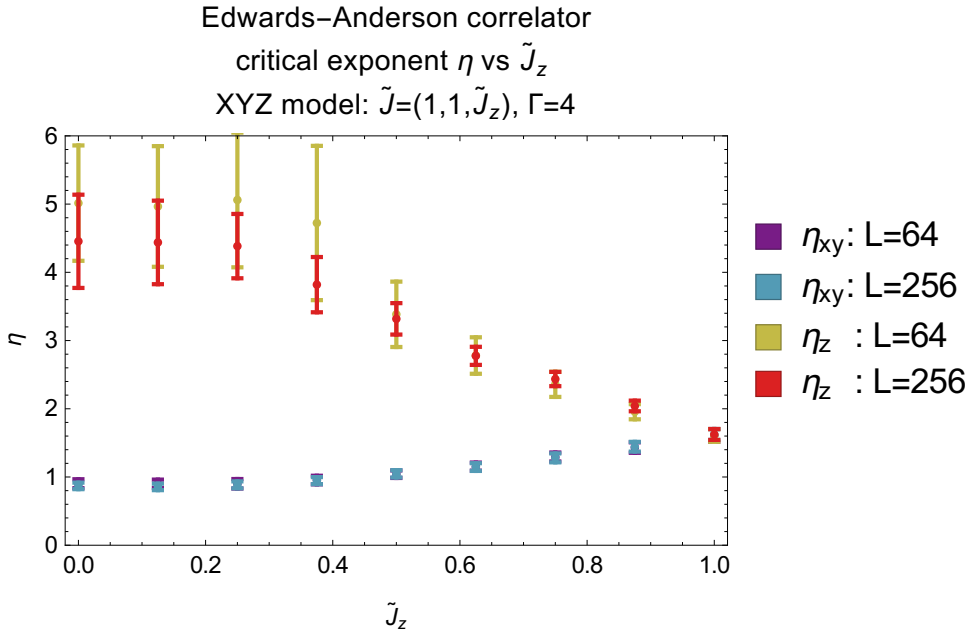

Figure 5.6: Critical exponents η_{xy} and η_z (Eq. 5.10) vs $\tilde{J}_z$ with $\tilde{J}_x = \tilde{J}_y = 1$ for the XYZ spin chain of various system sizes L. η_{xy} (η_z) appears to increase (decrease) continuously as $\tilde{J}_z$ increases. At least for $\tilde{J}_z > 1/2$, we do not expect the continuously varying exponents to be a result of finite size effects because η shows very little system size dependence in the above plot. The critical exponents were calculated as shown in Fig. 5.5. (error bar details: [166])

be understood in the limit $J_z = 0$, where the system can be mapped to two independent free random Majorana fermion chains.

5.6 Long Range Mutual Information

In Sec. 5.4 we used the entanglement entropy to diagnose the critical phase as a marginal MBL phase due to its logarithmically diverging entanglement entropy (Eq. 5.8). However, only studying the asymptotics of the entanglement entropy $S_{\mathrm{E}}(\ell)$ for large connected subsystem has some limitations. For example, $S_{\mathrm{E}}(\ell)$ can not firmly distinguish a trivial phase from a spin glass, since both just asymptote to a constant. Instead of studying the entanglement entropy of just a single connected subsystem, it has been proposed to study the long range mutual information (LRMI) between two disconnected subsystems with large separation [4]. The mutual information $\mathcal{I}$ between two non-overlapping subsystems A and B is defined to be

$$\mathcal{I}(A, B) = S_{\mathrm{E}}(A) + S_{\mathrm{E}}(B) - S_{\mathrm{E}}(A \cup B) \tag{5.11}$$

We will take subsystems A and B to be lines of length ℓ with separation given by x as shown in Fig. 5.7 (bottom). We will be interested in the $L = \infty$ limit of the asymptotics of the LRMI $\mathcal{I}_\ell(x)$ as the separation x tends to infinity while the subsystem length ℓ is held fixed. Since the mutual information is also an upper bound of correlation functions, in principle, the mutual information should decay slower than any correlation function.

In a direct product state with no spin glass order (which doesn't exist in the XYZ model), far apart regions share little entanglement, and thus the LRMI should decay exponentially. In a spin glass phase there is long range glassy order, and the LRMI asymptotes to a constant (Fig. 5.7). Thus, LRMI can easily distinguish a trival phase from a spin glass phase. This fact could be very useful in more complicated models where

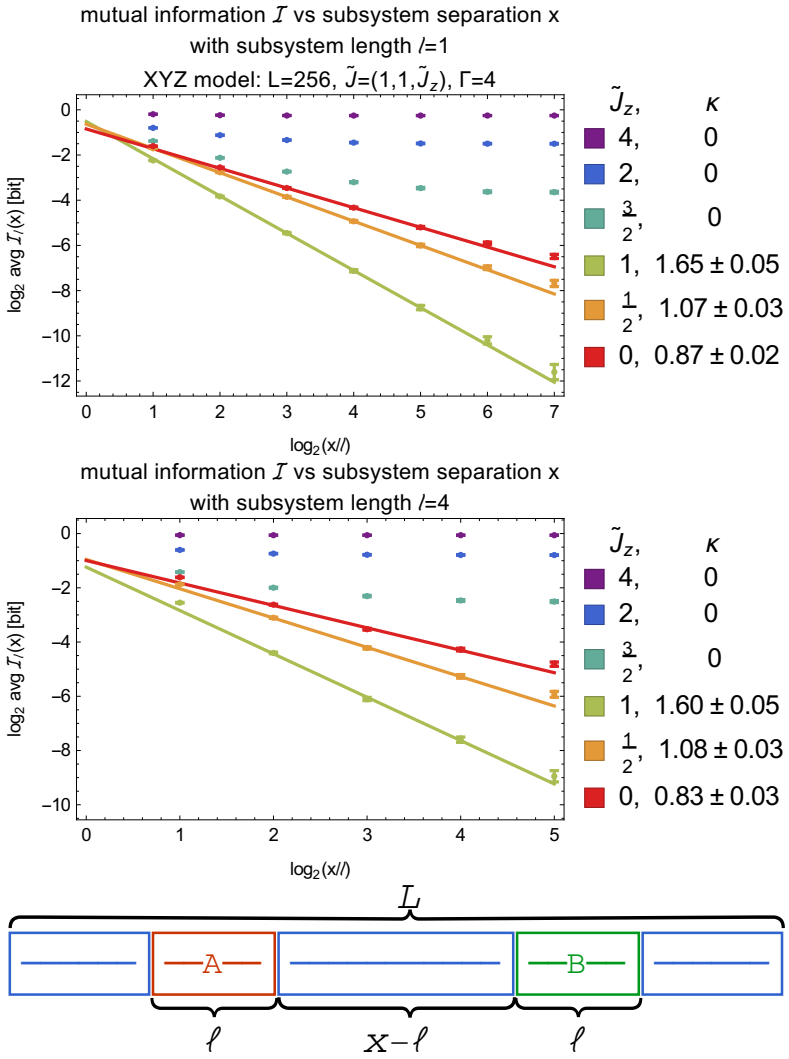

Figure 5.7: Disorder and energy averaged long range mutual information (LRMI) $\mathcal{I}$ of two subsystems (of length $\ell = 1$ (top) and $\ell = 4$ (middle)) vs subsystem separation x for different $\tilde{J}_z$ in the XYZ spin chain with $\tilde{J}_x = \tilde{J}_y = 1$ and system size $L = 256$. Subsystem length ℓ and separation x are defined as shown in the bottom diagram. When $\tilde{J}_z > 1$, the system is in a spin glass phase, and the LRMI asymptotes to a constant. When $\tilde{J}_z$ is only slightly larger than 1, e.g. $\tilde{J}_z = 3/2$, there appears to be moderate finite size effects. When $\tilde{J}_z \leq 1$, the system is in a marginal MBL phase, and the LRMI decays according to a power law with a critical exponent κ: $\mathcal{I}_\ell(x) \sim (x/\ell)^{-\kappa}$. The critical exponent κ does not appear to depend on the subsystem length ℓ, but it does appear to increase continuously with $\tilde{J}_z$, unlike the effective central charge c' which remains fixed (Fig. 5.4). If the above plots were drawn on top of each other, the critical $\tilde{J}_z \leq 1$ data would very nearly overlap, which implies that changing ℓ just rescales x as one would expect in a scale invariant system: $\mathcal{I}_\ell(x/\ell) \approx \mathcal{I}_{\ell'}(x/\ell')$. (error bar details: [166])

finding the right order parameter is difficult. Finally, in a critical phase in any dimension, the LRMI is expected to decay according to a power law with some critical exponent κ: $\mathcal{I}_\ell(x) \sim (x/\ell)^{-\kappa}$. In the XYZ model, a power law is indeed observed (Fig. 5.7). Since the mutual information should not decay faster than the correlation functions, we at least expect $\kappa \leq \min(\eta_{xy}, \eta_z)$, which is also verified within the numerical error. The critical exponent κ does not seem to depend on the subsystem length ℓ; but κ does appear to increase continuously with $\tilde{J}_z$, unlike the effective central charge c' which remains fixed. Thus, the LRMI can efficiently tell if a phase is a trivial, spin glass, or marginal MBL critical phase; and works as expected in the XYZ model (Fig. 5.7).

5.7 Conclusion

In conclusion, we have studied the XYZ spin chain with independently random XX, YY, and ZZ couplings on each bond. Unlike the random XXZ or Heisenberg models, the XYZ model breaks the continuous spin rotational symmetry down to the discrete $\mathbb{Z}_2^2$ symmetry, such that the quantum phase transitions between different symmetry-breaking spin glass phases can persist to finite energy density as marginal MBL critical lines. We use the SBRG numerical method to calculate the entanglement entropy, Edwards-Anderson correlator, and long-range mutual information. In the MBL spin glass phase, the entanglement entropy follows the area-law scaling and quickly saturates to a value of $S_{\mathrm{E}} \geq \ln 2$. Both the Edwards-Anderson correlator and the long-range mutual information exhibit long-range behavior, demonstrating spin glass order. Along the marginal MBL critical line, the entanglement entropy follows the logarithmic scaling $S_{\mathrm{E}}(\ell) = (c'/3) \ln \ell$, with a fixed effective central charge $c' = \ln 2$. Both the Edwards-Anderson correlator and the long-range mutual information decays in a power-law, and the critical exponents varies continuously along the marginal MBL line.

5.8 Permissions and Attributions

The content of this chapter is the result of a collaboration with Yi-Zhuang You and Cenke Xu, and has previously appeared in [170]. We acknowledge helpful discussions with David Huse and Andrew Potter. In particular, Appendix 5.D resulted from comments from David Huse. The authors are supported by David and Lucile Packard foundation and NSF Grant No. DMR-1151208.

5.A Many Body Localization

A Hamiltonian is said to be fully many body localized (MBL) if all eigenstates in the many-body spectrum are localized [25]. It is believed that there exists a finite local unitary transformation U that can diagonalize the MBL Hamiltonian H:

$$\begin{aligned} H_{\text{eff}} &= UHU^\dagger \\ &= \sum_i h_i^{(1)}\tau_i^z + \sum_{ij} h_{ij}^{(2)}\tau_i^z\tau_j^z + \sum_{ijk} h_{ijk}^{(3)}\tau_i^z\tau_j^z\tau_k^z + \cdots \end{aligned} \tag{5.12}$$

where the τ_i^z are the LIOM. The fact that U is a finite local unitary transformation means that it can be written as a finite time evolution of a time dependent local Hamiltonian with bounded spectrum. This implies that the LIOM $U\tau_i^z U^\dagger$ must be local operators (with exponentially decaying tails). This implies that the eigenstates of an MBL Hamiltonian display an area law entanglement (Fig. 5.4), as opposed to the volume law seen in excited states of thermal systems. An example of such a U can be inferred from Fig. 5.12. Furthermore, the $h_{ijk\ldots}^{(n)}$ decay exponentially with n (Fig. 5.3) and distance $\max(|i-j|, |i-k|, |j-k|, \ldots)$. This implies that in an MBL system, the time evolution of a direct product state displays an entanglement entropy which increases only logarithmically with time [26, 27, 28], instead of linearly as in thermal systems. This implies

that an MBL system can't efficiently spread entanglement, and thus can't act as its own heat bath.

5.A.1 Marginal MBL

If one observes a phase transition between two fully MBL phases, then it's possible that the critical point between them is a marginal MBL phase. A margin MBL phase doesn't obey Eq. 5.12 with the same restrictions for the unitary transformation U and coefficients $h^{(n)}_{ijk\ldots}$. For example, the LIOM in the original bases $U\tau^z_i U^\dagger$ become nonlocal [138], which implies that U can't be a finite local unitary transformation. In SBRG, the unitary transformation U that is found is nonlocal and requires a time evolution that diverges logarithmically with the system size, as can be inferred from Fig. 5.11.

5.B Spectrum Bifurcation Renormalization Group

In this work, we use the recently developed Spectrum Bifurcation Renormalization Group (SBRG) [138] to simulate the XYZ model. SBRG is similar to RSRG-X [147], and behaves similarly to RSRG-X for the models on which RSRG-X can be applied. However, SBRG differs in that it (approximately) computes the commuting local integrals of motion (LIOM) (also know as localized-bit [158] stabilizers) of a Hamiltonian, and therefore targets the entire spectrum at once; while RSRG-X targets a specific eigenstate energy at a time. That is, given an arbitrary local Hamiltonian H written in terms of physical spins σ^μ_i, SBRG computes the unitary transformation U to a set of LIOM Pauli operators τ^μ_i such that H can be written as the sum of products of commuting τ^z_i operators with coefficients $(h^{(1)}_i, h^{(2)}_{ij}, h^{(3)}_{ijk}, ...)$ as in Eq. 5.12. The unitary transformation U is encoded using alternating C_4 transformations (see end of Appendix 5.B.1) and small Schrieffer-Wolff perturbations (Eq. 5.16).

With this information, SBRG can efficiently compute many quantities of interest such as Edwards-Anderson spin glass order parameters, the energy spectrum, entanglement entropies, and other LIOM properties. One advantage of SBRG is that it can handle Hamiltonian terms which are arbitrary local products of sigma matrices. This should be contrasted with other real space RG schemes (such as RSRG-X [147]) which require a specific Hamiltonian that is of closed form under RG. For example, next nearest neighbor terms often are not allowed to be created by the RG step of other methods. This flexibility allows SBRG to be applied to a large class of spin systems in all dimensions, including systems with topological order and symmetry protected topological order.

However, the price paid for this generality is that the Hamiltonian is not of closed form under RG, which results in exponentially many terms generated by the RG flow. Many of these terms will need to be dropped in order to preform computations efficiently. In this work, up to 256 addition off-diagonal terms are allows to be added during each RG step. This approximation seems to work well for systems with large disorder and deep in the fully MBL phase; but in marginal MBL phases, very large system sizes can become problematic. However, for the XYZ chain, it appears that reasonably accurate simulations can still be performed for systems of roughly 256 spins in the marginal MBL phase, and at least 10,000 spins deep in the MBL phase.

5.B.1 RG Step and Approximations

In SBRG, the Hamiltonian of a system is written as a linear combination of tensor products of pauli matrices:

$$H = \sum_{[\mu]} h_{[\mu]} \sigma^{[\mu]} = \sum_{[\mu]} h_{[\mu]} \otimes_i \sigma^{\mu_i} \tag{5.13}$$

As described in Appendix A2 of [138], for each RG step, the term $h_3 \sigma^{[\mu_3]}$ with the largest coefficient h_3 is chosen to be the next local integral of motion (LIOM) since it describes

the leading energy scale. However, $\sigma^{[\mu_3]}$ doesn't yet commute with the Hamiltonian H. The Hamiltonian can be split into three parts

$$H = h_3\sigma^{[\mu_3]} + \Delta + \Sigma$$

where Δ commutes with $\sigma^{[\mu_3]}$ while Σ anticommutes with $\sigma^{[\mu_3]}$. In order to make $\sigma^{[\mu_3]}$ into a LIOM, we must eliminate Σ. First assume that

$$|\Sigma| \ll h_3 \tag{5.14}$$

$$\max_{\Delta_0 \in \Delta, [\Sigma, \Delta_0] \neq 0} |\Delta_0| \ll h_3 \tag{5.15}$$

where $|\Sigma| \equiv \sqrt{2^{-L}\ \mathrm{Tr}(\Sigma \cdot \Sigma^\dagger)}$ and $\max_{\Delta_0 \in \Delta, [\Sigma, \Delta_0] \neq 0} |\Delta_0|$ is the absolute value of the largest pauli matrix coefficient of all terms in Δ that don't commute with Σ. Fig. 5.8 provides evidence that these assumptions are valid. (RSRG-X depends on a similar set of assumptions.) With these assumptions, a Schrieffer-Wolff transformation can be performed in order to eliminate the off-diagonal component Σ to order $O(h_3^{-2})$:

$$\begin{aligned} S &= \exp\left(-\frac{1}{2h_3}\sigma^{[\mu_3]}\Sigma\right) \\ &= 1 - \frac{1}{2h_3}\sigma^{[\mu_3]}\Sigma - \frac{1}{8h_3^2}\Sigma^2 + O(h_3^{-3}) \end{aligned} \tag{5.16}$$

$$\begin{aligned} H \to H' &= S^\dagger H S \\ &= h_3\sigma^{[\mu_3]} + \Delta + \frac{1}{2h_3}\sigma^{[\mu_3]}\Sigma^2 \\ &+ \frac{1}{2h_3}\sigma^{[\mu_3]}[\Sigma, \Delta] + O(h_3^{-2}) \end{aligned} \tag{5.17}$$

The first approximation (Eq. 5.14) allows the unitary S to be expanded and implies that the third term in H is small: $\frac{1}{2h_3}\sigma^{[\mu_3]}\Sigma^2 \sim O(h_3^{-1})$. Although the first three terms of H' (Eq. 5.17) commute with $\sigma^{[\mu_3]}$, the final term ($\frac{1}{2h_3}\sigma^{[\mu_3]}[\Sigma, \Delta]$) does not. This term must be removed since it's $O(h_3^{-1})$, which is the leading order in the new terms that are generated by the RG step. However, this term can be ignored since another unitary

transformation can eliminate it at the expense of only $O(h_3^{-2})$ terms:

$$\begin{aligned} H' \to H'' &= U^\dagger H U \\ &= h_3 \sigma^{[\mu_3]} + \Delta + \frac{1}{2h_3}\sigma^{[\mu_3]}\Sigma^2 + O(h_3^{-2}) \end{aligned} \tag{5.18}$$

The second approximation (Eq. 5.15) is used to to claim that the last term in Eq. 5.17 is indeed $O(h_3^{-1})$.

Thus, $\sigma^{[\mu_3]}$ is a LIOM of H'' at order $O(h_3^{-2})$ if we can assume Eq. 5.14 and 5.15. In Fig. 5.8 we show that these appear to be safe and controlled approximations for sufficiently large Γ in the critical phase. (The approximations are even better in the spin glass phase.) The first approximation (Eq. 5.14) gets better under RG flow, while the second (Eq. 5.15) does not show a clear trend. If the second approximation is actually getting worse under RG, this might suggest that the critical phase in the XYZ model is actually thermal.

Now that $\sigma^{[\mu_3]}$ commutes with the Hamiltonian, we may want to perform a change of basis $\sigma^{[\mu_3]} \to \tau_j^3$. Any integer j can be used as long as it hasn't been used before. E.g. j could be chosen to indicate the RG step number, or the rough position of $\sigma^{[\mu_3]}$ on the lattice. In practice, it is convenient to use the same Hilbert space for σ and τ. This can be done by rotating $\sigma^{[\mu_3]} \to \sigma_j^3$ using a unitary transformation composed of one or two C_4 transformations $\exp\left(\frac{i\pi}{4}\sigma^{[\mu]}\right)$ as described in [138].

5.B.2 Edwards-Anderson Correlator via SBRG

Given a Hamiltonian H, SBRG calculates the Schrieffer-Wolff transformation $S_{\text{tot}} = \prod S_j$ (Eq. 5.16) that rotates (Eq. 5.20) the Hamiltonian into a basis with LIOM $\sigma_j^{[\mu_3]}$. Before applying S_{tot}, $\sigma_j^{[\mu_3]}$ are only approximate LIOM of H.

We want to calculate the energy averaged Edwards-Anderson correlator of an operator

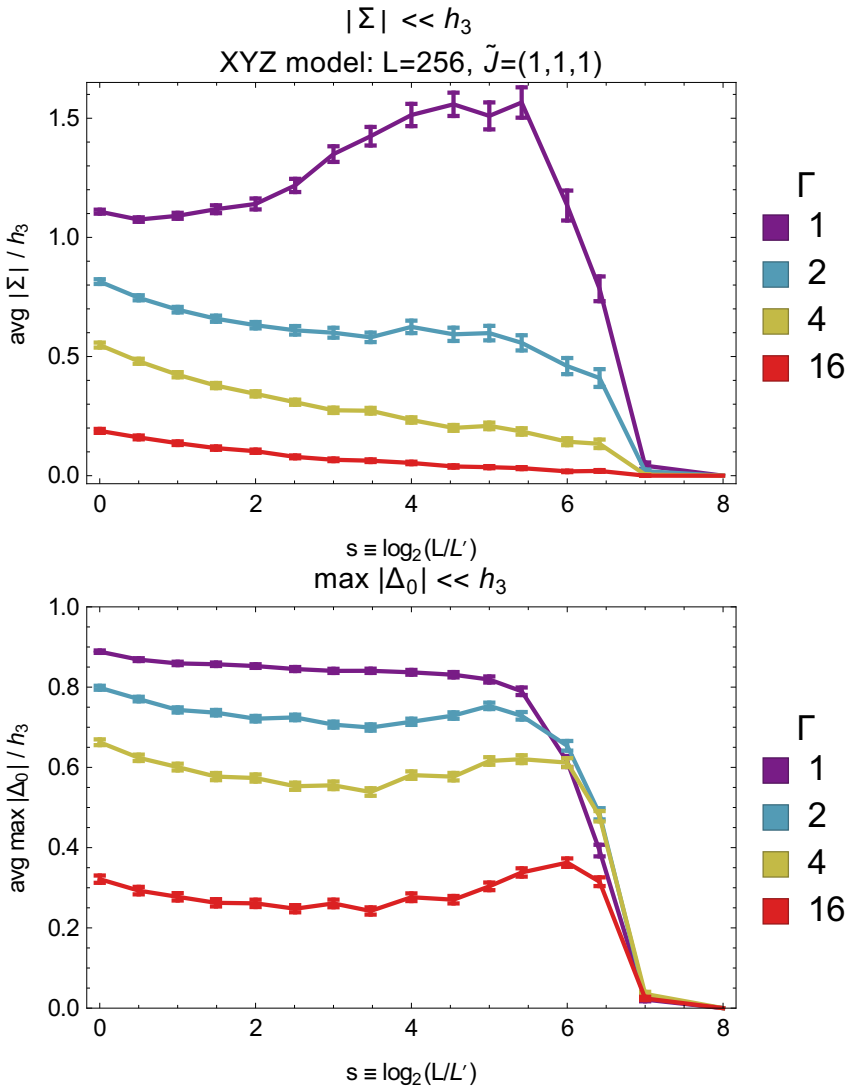

Figure 5.8: Disorder average of $|\Sigma|/h_3$ (Eq. 5.14) (top) and $\max|\Delta_0|/h_3$ (Eq. 5.15) (bottom) vs amount of RG flow $s \equiv \log_2(L/L')$ for different amounts of disorder Γ where $L = 256$ is the system size and L' is the number of remaining spins. These are the small parameters used in the approximations Eq. 5.14 and 5.15. Data is shown at the critical point $\tilde{J}_x = \tilde{J}_y = \tilde{J}_z = 1$; away from this point, these approximations are even better. As the disorder Γ increases, the plotted values get arbitrarily small, suggesting that these approximations can be controlled by Γ. In addition, the first approximation (top) gets better under RG flow (for large Γ); the second (bottom) does not show a clear trend. Similar to Fig. 5.3, the large Γ data in this plot can also be collapsed to a single curve if $f(y) = y^{1/\Gamma}$ is applied to the data, which shows that $|\Sigma| \sim \max|\Delta_0| \sim e^{-\Gamma}$ decreases exponentially as Γ increases. (error bar details: [166])

Q:

$$\text{avg}\,\langle Q\rangle^2 \equiv \frac{1}{N_E}\sum_E \langle E|Q|E\rangle^2 \tag{5.19}$$

To do this, we will apply the Schrieffer-Wolff transformation to both $\sigma^{[\mu]}$ and $|E\rangle$:

$$H \to \tilde{H} \equiv S_{\text{tot}}^\dagger H S_{\text{tot}} \tag{5.20}$$

$$|E\rangle \to |\tilde{E}\rangle \equiv S_{\text{tot}}^\dagger |E\rangle \tag{5.21}$$

$$\begin{aligned} Q \to \tilde{Q} &\equiv S_{\text{tot}}^\dagger Q S_{\text{tot}} \\ &= \sum_{[\mu]} q_{[\mu]}\sigma^{[\mu]} \end{aligned} \tag{5.22}$$

for some set of coefficients $q_{[\mu]}$. Now every $\sigma_j^{[\mu_3]}$ takes a definite value for every energy eigenstate $|\tilde{E}\rangle$ of $\tilde{H}$: $\sigma_j^{[\mu_3]} = \pm 1$. This implies that $\langle\tilde{E}|\sigma^{[\mu]}|\tilde{E}\rangle = \pm 1$ if $\sigma^{[\mu]}$ commutes with all $\sigma_j^{[\mu_3]}$, otherwise it's zero. Thus

$$\begin{aligned} \text{avg}\,\langle Q\rangle^2 &= \frac{1}{N_E}\sum_E \langle\tilde{E}|\tilde{Q}|\tilde{E}\rangle^2 \\ &= \frac{1}{N_E}\sum_E\sum_{[\mu]} \langle\tilde{E}|q_{[\mu]}\sigma^{[\mu]}|\tilde{E}\rangle^2 \\ &= \sum_{[\mu]} \begin{cases} q_{[\mu]}^2 & \sigma^{[\mu]} \text{ commutes with all } \sigma_j^{[\mu_3]} \\ 0 & \text{otherwise} \end{cases} \end{aligned} \tag{5.23}$$

In the second line, we were able to pull the $\sum_{[\mu]}$ out of $\langle\tilde{E}|\cdots|\tilde{E}\rangle^2$ because cross terms cancel after the energy average. Thus, the energy averaged Edwards-Anderson correlator can be calculated from the coefficients $q_{[\mu]}$ of $\tilde{Q}$ (Eq. 5.22).

5.B.3 Algorithm and Implementation Details

Unfortunately, the Schrieffer-Wolff transformation generates an exponentially large number of terms in Σ^2 in Eq. 5.18 and $\tilde{Q}$ in Eq. 5.22. Thus, one must drop terms. In this

work, for each Schrieffer-Wolff transformation, we keep the 256 largest additional terms in Σ^2 and 32 largest additional terms in $\tilde{Q}$.

Most operators $\sigma^{[\mu]}$ in the Hamiltonian will be local. Thus, it is important to make use of this locality when implementing SBRG. With this optimization, the CPU time for an SBRG simulation of a Hamiltonian in an MBL phase scales linearly (up to log corrections) with system size.

For this work, each $L = 256$ disorder realization data point took a couple minutes of CPU time. However, reasonable data is achievable with only 1/8th as many additional terms in Σ^2 and $\tilde{Q}$, for which a simulation only takes several seconds. The SBRG data used in this paper was calculated in roughly two weeks on a quad-core i7-3720QM underclocked to 2GHz. The SBRG data included 1024 disorder realizations for each data point. However, reasonable data was attainable with less (~ 100) disorder realizations and additional terms, for which only a few hours of simulation time is necessary.

For this work, the Haskell programming language was used to implement SBRG in roughly 1000 lines of code, and the implementation has been published to github [171]. Haskell was chosen because it could produce fast code (potentially faster than C++ due to very efficient garbage collection) while requiring the smallest amount of developer time compared to other languages. Development time was minimized using Haskell because Haskell is very good at dealing with complicated data structures, which were necessary for making use of the locality of operators mentioned above. This is a result of Haskell's strong type system, automatic garbage collection, functional programming paradigm, and high amount of expressiveness.

Random numbers were generated using a combined linear congruential generator (System.Random.StdGen in Haskell) with period 2^{61}, which is much larger than the number of random numbers used in this work, which was roughly 2^{29}.

5.C XYZ Model Details

5.C.1 Disorder Distribution

SBRG is a numerical method which relies on large disorder for accuracy. For this reason, it is important that we choose a disorder distribution with very large randomness. For the XY ($J_z = 0$) and XXZ ($J_{i,x} = J_{i,y}$) spin chains, it has been shown that with large disorder, $J_{i,\mu}$ flows to a power law distribution [161, 162] with a probability distribution function (PDF) equal to

$$\mathrm{PDF}(J_{i,\mu}) = \frac{1}{\Gamma J_{i,\mu}} \left(\frac{J_{i,\mu}}{J_\mu} \right)^{1/\Gamma} \quad , \quad J_{i,\mu} > 0 \tag{5.24}$$

where Γ controls the strength of the disorder, with larger Γ corresponding to stronger disorder. It's useful to define $\beta_{i,\mu} \equiv -\ln \frac{J_{i,\mu}}{J_\mu} \geq 0$. With this definition, $\beta_{i,\mu}$ follows an exponential distribution with a mean and standard deviation (as in Eq. 5.1) equal to Γ:

$$\mathrm{PDF}(\beta_{i,\mu}) = \Gamma^{-1} e^{-\beta_{i,\mu}/\Gamma} \quad , \quad \beta_{i,\mu} > 0 \tag{5.25}$$

It's also useful to define $\tilde{J}_{i,\mu}$ by $J_{i,\mu} \equiv \tilde{J}_{i,\mu}^\Gamma$. With this definition, $\tilde{J}_{i,\mu}$ is uniformly distributed in $[0, \tilde{J}_\mu]$ where $J_\mu \equiv \tilde{J}_\mu^\Gamma$:

$$\mathrm{PDF}(\tilde{J}_{i,\mu}) = \tilde{J}_\mu^{-1} \quad , \quad 0 < \tilde{J}_{i,\mu} < \tilde{J}_\mu \tag{5.26}$$

We therefore let $J_{i,\mu}$ follow the above (equivalent) distributions so that we can effectively probe closer to the infinite system size limit while using the same physical system size. (We assume that the disorder becomes stronger under RG in the large disorder limit.) We will show results for $\Gamma = 4$ because this is the smallest Γ for which SBRG agrees well with exact diagonalization on small latices (data not shown in this paper), and for which our approximations appear to be safe (see Appendix 5.B.1 and 5.D, and Sec. 5.3.2).

5.C.2 Tuning Parameters

We use $\tilde{J}_\mu$ as tuning parameters instead of J_μ because $\tilde{J}_\mu$ are better behaved at large disorder Γ. For example, our phase diagram in Fig. 5.1 would depend strongly on Γ if J_μ were used as tuning parameters instead of $\tilde{J}_\mu$. However, when $\tilde{J}_\mu$ are used as tuning parameters, the phase diagram has little dependence on Γ when Γ is large; and this allows the large disorder limit to be well defined.

A simple calculation makes this more transparent. If $P(J_{i,\mu} > J_{i,\nu})$ is the probability that $J_{i,\mu} > J_{i,\nu}$, then $P(J_{i,\mu} > J_{i,\nu}) \to \frac{1}{2}$ as $\Gamma \to \infty$ if J_μ is held constant. Thus large disorder effectively washes out the differences between different J_μ and the $J_1 = J_2 = J_3$ point effectively dominates the phase diagram if J_μ is held constant as $\Gamma \to \infty$. However, if we define $J_\mu \equiv \tilde{J}_\mu^\Gamma$ and hold $\tilde{J}_\mu$ constant instead, then $P(J_{i,\mu} > J_{i,\nu})$ is independent of Γ. This is because

$$\begin{aligned} P(J_{i,\mu} > J_{i,\nu}) &= P(\tilde{J}_{i,\mu} > \tilde{J}_{i,\nu}) \text{ since } J_{i,\mu} \equiv \tilde{J}_{i,\mu}^\Gamma \\ &= \begin{cases} \frac{r}{2} & \text{if } r < 1 \\ 1 - \frac{1}{2r} & \text{if } r > 1 \end{cases} \text{ by Eq. 5.26} \\ &\text{where } r = \frac{\tilde{J}_\mu}{\tilde{J}_\nu} = \left(\frac{J_\mu}{J_\nu}\right)^{1/\Gamma} \end{aligned}$$

5.D Exact Diagonalization Study

We now study the critical point $\tilde{J}_x = \tilde{J}_y = \tilde{J}_z = 1$ using exact diagonalization to check that the critical phase is not thermal. In Fig. 5.9 we show the level statistic r of the XYZ model vs disorder strength Γ. For each disorder realization, the level statistic

$r_n^{(a)}$ is defined as a ratio of level spacings $\delta_n^{(a)}$ [143] in a given symmetry sector (a):

$$r_n^{(a)} \equiv \frac{\min(\delta_n^{(a)}, \delta_{n+1}^{(a)})}{\max(\delta_n^{(a)}, \delta_{n+1}^{(a)})} \tag{5.27}$$
$$\delta_n^{(a)} \equiv E_n^{(a)} - E_{n-1}^{(a)}$$
$$E_{n+1}^{(a)} \geq E_n^{(a)}$$

For our model, there are four symmetry sectors (a) which are labeled by the eigenvalues of the symmetry operators of our model: $\prod_i \sigma_i^x$ and $\prod_i \sigma_i^y$. In Fig. 5.9 we average over disorder realizations, level spacings n, and symmetry sectors (a). We find that with weak disorder Γ, the level statistic approaches (with increasing system size) the GOE (Gaussian orthogonal ensemble) level statistic $r_{\text{GOE}} \approx 0.53$, which is expected for a thermal system. As the disorder strength increases, the level statistic drops below the Poisson level statistic $r_{\text{Poisson}} \approx 0.39$, which suggests that the system is not thermal.

The level statistic continues below the Poisson level statistic because we use a power law distribution of coefficients in the Hamiltonian (Eq. 5.24), instead of a uniform or Gaussian distribution. This can be understood most easily in the $\tilde{J}_x = \tilde{J}_y = 0$ and $\tilde{J}_z = 1$ limit (see Fig. 5.9), where the Hamiltonian is already diagonal. When $\Gamma = 1$, we exactly reproduce the Poisson level statistic. However, a simple numerical calculation shows that as Γ increases, the level statistic decays to zero as a power law with increasing Γ: $r \sim 1/\Gamma$.

In Fig. 5.10 we show the how the entanglement scales with subsystem size. When the disorder is weak, the system displays a volume law entanglement, as expected for a thermal system. But for strong disorder, the entanglement increases very slowly with subsystem size, which suggests that the strong disorder results in either a MBL phase with area law entanglement or a marginal MBL phase with log-law entanglement. (In Fig. 5.4 we SBRG and large system sizes to show that the entanglement follows a log-law.) Again we see that for weak disorder Γ, the critical point is thermal, but with strong

disorder the critical point does not appear to be thermal.

It is worth emphasizing that in both ED plots, a disorder strength of $\Gamma = 1$ (which corresponds to uniformly distributed random coefficients J_i) was not sufficient to prevent thermalization of the XYZ model's critical point. Therefore, considering disordered systems with only Gaussian (with $\Gamma \approx 1.1$ via Eq. 5.1) or uniform disorder distributions may not always be sufficient if one is interested in observing marginal MBL critical phases. That is, similar to the XYZ model's critical point, other models may also require large Γ (defined by Eq. 5.1) in order to prevent thermalizaion.

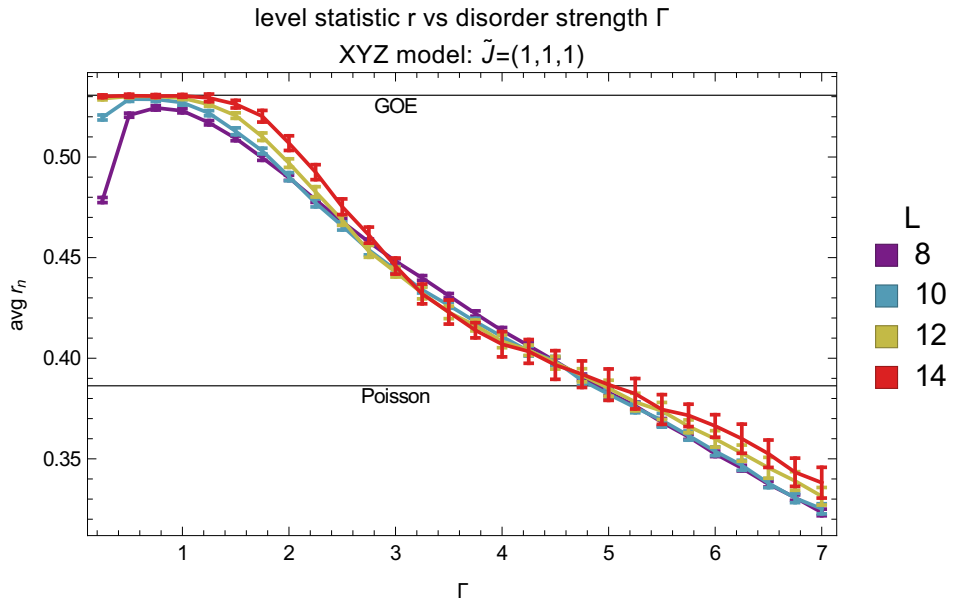

Figure 5.9: Disorder and energy averaged level statistic r (Eq. 5.27) vs disorder strength Γ for different system sizes L in the XYZ spin chain with $\tilde{J}_x = \tilde{J}_y = \tilde{J}_z = 1$. With weak disorder, the system approaches GOE level statistics with increasing system size, which indicates that the system is thermal. As the disorder strength increases, the level statistic drops below the Poisson level statistic, which suggests that the system is not thermal with strong disorder. (error bar details: [166])

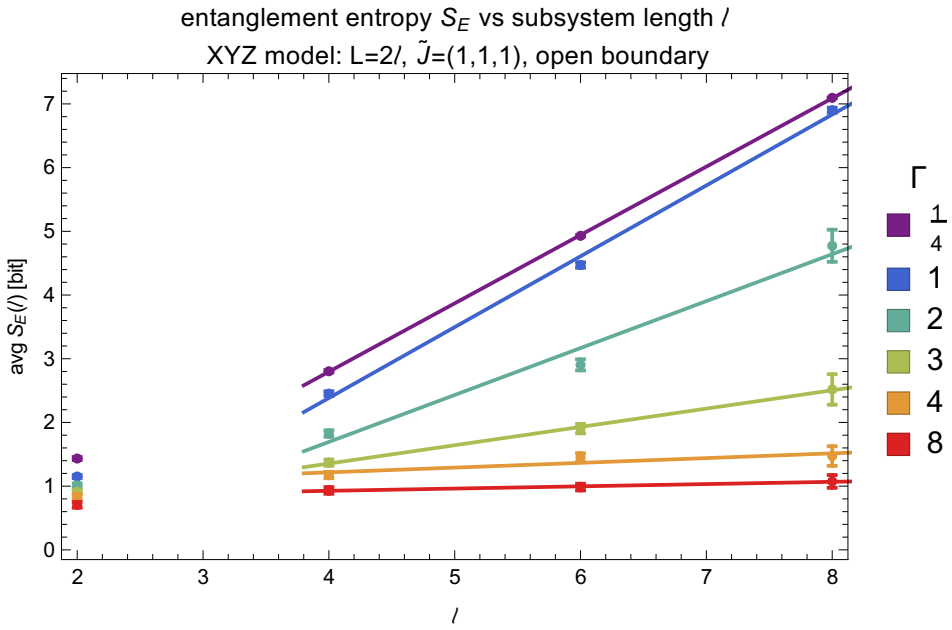

Figure 5.10: Disorder and energy averaged entanglement entropy S_{E} [bit] ($\equiv S_{\mathrm{E}}/\ln 2$) (Eq. 5.6) vs subsystem length ℓ for different disorder strengths Γ in the XYZ spin chain with $\tilde{J}_x = \tilde{J}_y = \tilde{J}_z = 1$ and system size $L = 2\ell$ with open boundary conditions. Each entanglement subsystem splits the system in half. We only show even ℓ in order to avoid an even-odd effect. As the disorder strength Γ increases, the slope of the data decreases to roughly zero. This suggests a transition from a thermal phase with volume law entanglement to a non-thermal phase. (error bar details: [166])

5.E Spin Glass Entanglement Entropy Calculation

Here we calculate the entanglement entropy of a subsystem A in the spin glass phase using the stabilizer rank algorithm in [138]. Deep in the spin glass phase where J^z dominates, the LIOM are given by:

$$\tau_i^z = \sigma_i^z \sigma_{i+1}^z \text{ with } i = 1, 2, \dots L-1 \tag{5.28}$$
$$\tau_L^z = \prod_{i=1}^{L} \begin{cases} \sigma^x & \text{if } J_x > J_y \\ \sigma^y & \text{if } J_y > J_x \end{cases}$$

Assuming $i < j$. We can see that in this case indeed $\sigma_i^z \sigma_j^z = \prod_{k=i}^{j-1} \tau_k^z$ is a product of the LIOM. Only three of the LIOM will be cut by the subsystem A, which we will take to be the sites $i, i+1, \dots j$ where $j = i - 1 + \ell$. These LIOM are $\tau_{i-1}^z, \tau_j^z, \tau_L^z$. We then "trace out degrees of freedom not in A" by removing σ-matrices not in A:

$$\begin{array}{ccc} \tau_{i-1}^z = \sigma_{i-1}^z \sigma_i^z & \tau_j^z = \sigma_j^z \sigma_{j+1}^z & \tau_L^z = \prod_{i'} \sigma_{i'}^x \\ \downarrow & \downarrow & \downarrow \\ \hat{\tau}_{i-1}^z \to \sigma_i^z & \hat{\tau}_j^z \to \sigma_j^z & \hat{\tau}_L^z \to \prod_{i'=i}^{j} \sigma_{i'}^x \end{array}$$

We then consider the 3x3 anticommutivity matrix of these three $\hat{\tau}$ operators:

$$M = \begin{pmatrix} 0 & 0 & 1 \\ 0 & 0 & 1 \\ 1 & 1 & 0 \end{pmatrix}$$

where a 1 denotes anticommutivity while a 0 denotes commutivity. The entanglement entropy S_{E} is then given by

$$\begin{aligned} S_{\text{E}} &= \frac{\ln 2}{2} \text{rank} M \text{ (over } \mathbb{Z}_2) \\ &= \ln 2 \end{aligned} \tag{5.29}$$

where the matrix rank is calculated over the field $\mathbb{Z}_2$. When one isn't deep in the spin glass phase, the LIOM become more complicated (as in Fig. 5.12); more LIOM are cut by A; and the entanglement entropy increases slightly due to additional boundary contributions which don't depend significantly on the size of the subsystem A.

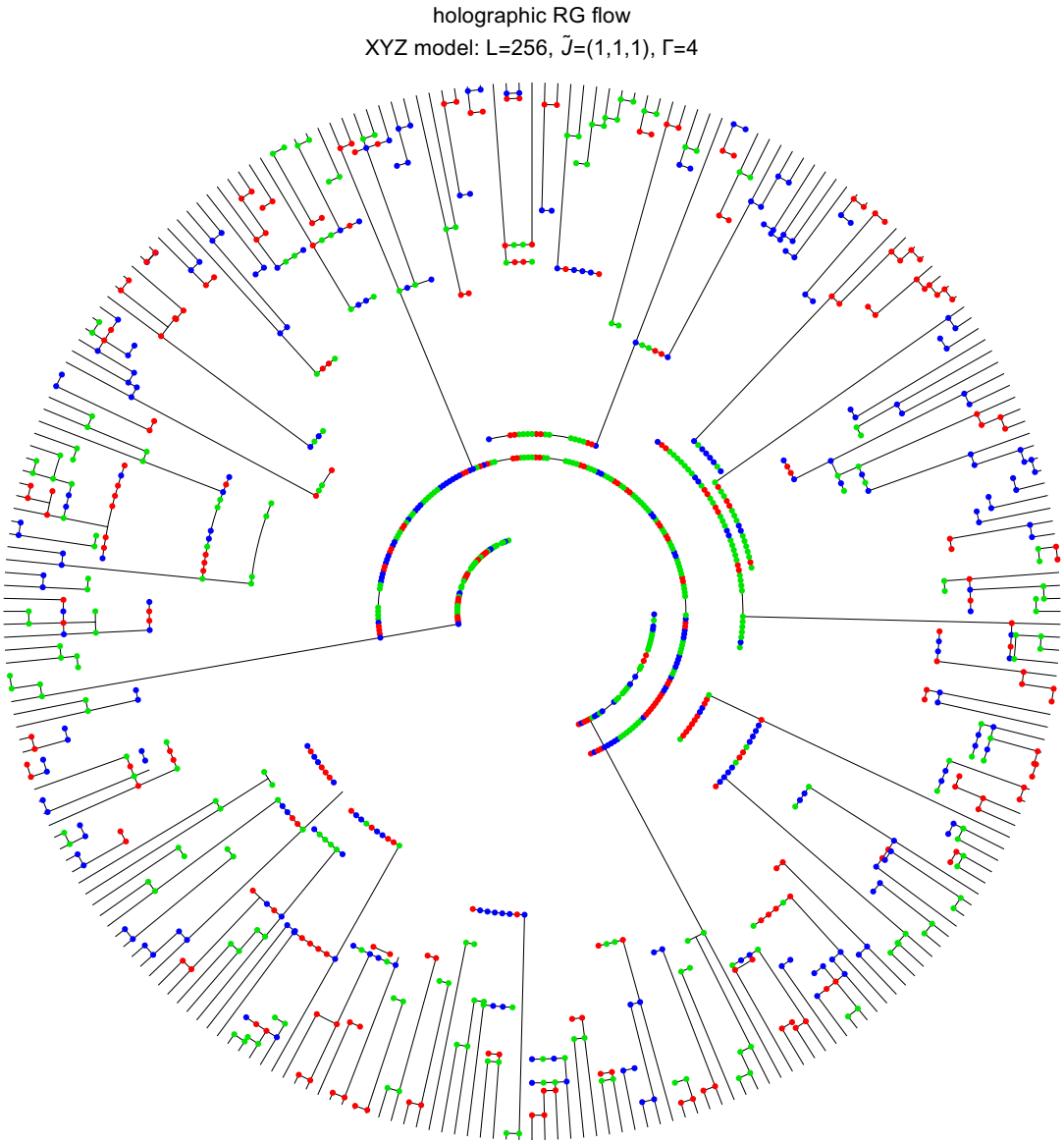

Figure 5.11: Approximate RG flow and LIOM for the XYZ spin chain at the critical point $\tilde{J}_x = \tilde{J}_y = \tilde{J}_z = 1$. The initial Hamiltonian starts at the boundary of the disk, with a spin living at the end of each radial line at the edge of the disk. SBRG then performs an RG which identifies a LIOM at each step of the RG (see Appendix 5.B.1). In the limit of large disorder, the LIOM can be approximated as a product of σ^x (red), σ^y (green), and σ^z (blue) matrices (dots connected by an arc line in the figure). Each LIOM in the figure also marks the end of a radial line to denote that a degree of freedom has been diagonalized (cf. "integrated out") at this RG step. Because we are in a marginal MBL phase, LIOM exist with sizes at every length scale, which results in the critical properties of this phase: diverging entanglement entropy (Fig. 5.4), power-law Edwards-Anderson correlators (Fig. 5.5), and long power-law range mutual information (Fig. 5.7).

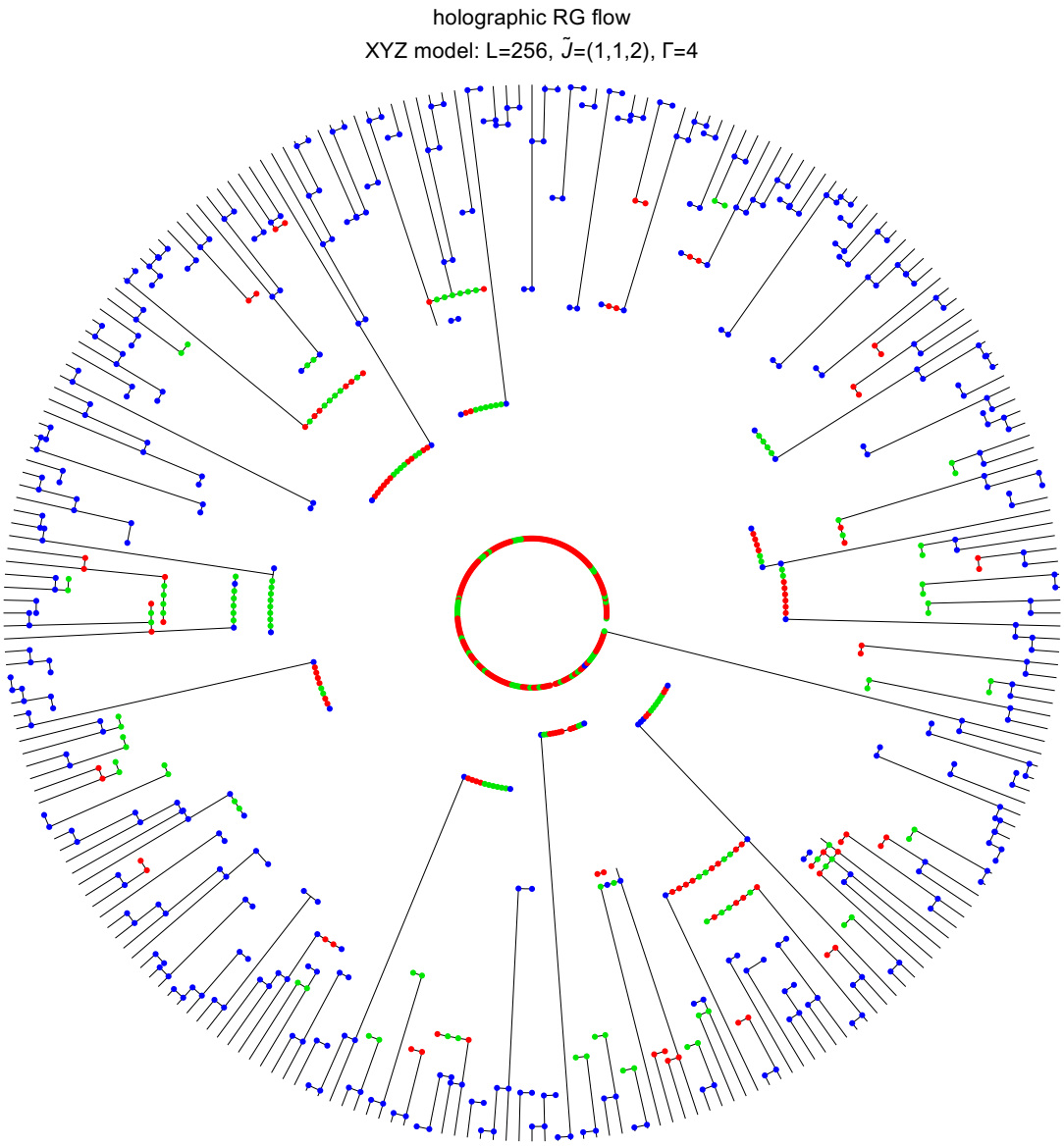

Figure 5.12: Approximate RG flow and LIOM for the XYZ spin chain in the spin glass phase with $\tilde{J} = (1, 1, 2)$. (See the caption of Fig. 5.11.) Because we are in the spin glass phase, the LIOM are dominated by blue $\sigma^z\sigma^z$ operators. The very large integral of motion in the center is just the Z_2 spin flip symmetry $\prod_i \sigma_i^x$, which is a little messy in the figure because it has been multiplied by some of the other LIOM to obtain an operator which is still an integral of motion. This center operator is essential for the spin glass properties of this phase: finite long range Edwards-Anderson correlators (Fig. 5.5) and finite long range mutual information (Fig. 5.7).

Chapter 6

Conclusion

In this thesis we have studied a number of exotic, topological, and many body localized quantum phase transitions in detail.

In Chapter 2 we studied the quantum phase transition between the Z_2 liquid and columnar VBS orders on both the isotropic and distorted triangular lattices. Fig. 2.5 summarizes our most important predictions for the isotropic case, such as the possibility of a nematic Z_2 spin liquid phase [1] with a continuous $3d$ XY* transition to the VBS phase. For a distorted triangle lattice, the nematic spin liquid intermediate phase is no longer necessary, and a direct continuous $3d$ XY* transition is possible between the spin liquid and VBS phases. The critical theories proposed can be checked by future numerical simulations.

It would also be interesting to study the direct quantum phase transition from the magnetic order to the columnar VBS orders on the triangular lattice, which can be viewed as a triangular lattice generalization of the deconfined quantum critical point [8, 9]. This transition would be driven by condensation of skyrmions or vortices of the magnetic order. It would also be interesting to understand the global phase diagram around the Z_2 spin

[1] Recent possible DMRG numerical evidence for a nematic spin liquid is given in [14].

liquid, which probably involves a noncollinear spiral spin order, the columnar/plaquette VBS order discussed in this current paper, and a collinear spin order. A similar global phase diagram was studied in [12] for the case with four vison minima in the BZ.

In Chapter 3 we demonstrated that there exist two novel continuous quantum phase transitions for 16 copies of $(2+1)d$ Majorana fermions. We show that the phase transition between the QSH to the trivial phase is naturally described by a nonlinear sigma model with a topological Θ-term (Eq. 1.4). We also show that this model hosts a new exotic quantum phase transition between a weakly interacting gapless Dirac fermion phase and a strongly interacting fully gapped and symmetric trivial phase; a field theory description of this phase transition is currently unknown. Both of these transitions are very different from the Standard Gross-Neveu model and Ginzburg-Landau theory. A controlled analytical field theory calculation for the critical exponents is not known yet; we will leave this to future studies.

In Chapter 4 we proposed a simple rule to determine whether a local Hamiltonian with symmetry can be many-body localized (MBL): If the ground and top state of a Hamiltonian belong to different SPT phases, then most likely there are some finite energy density states which can not be fully localized. Our argument is general enough that it can be applied to both free and interacting systems, and bosonic and fermionic SPT systems. And counterintuitively, we found that because interactions change the classification of fermionic topological insulators and topological superconductors, in some cases interactions actually assists localization, rather than delocalization.

In Chapter 5 we studied the XYZ spin chain with independently random XX, YY, and ZZ couplings on each bond. Unlike the random XXZ or Heisenberg models, the XYZ model breaks the continuous spin rotational symmetry down to the discrete Z_2^2 symmetry, which allows the quantum phase transitions between the different symmetry-breaking spin glass phases to persist to finite energy density as marginal MBL critical lines. We

used the SBRG [138] numerical method to calculate the entanglement entropy, Edwards-Anderson correlator, and long-range mutual information. In the MBL spin glass phase, the entanglement entropy follows the area-law scaling and quickly saturates to a value of $S_{\mathrm{E}} \geq \ln 2$. Both the Edwards-Anderson correlator and the long-range mutual information exhibit long-range behavior, demonstrating spin glass order. Along the marginal MBL critical lines, the entanglement entropy follows the logarithmic scaling $S_{\mathrm{E}}(\ell) = (c'/3) \ln \ell$ with a fixed effective central charge $c' = \ln 2$. Both the Edwards-Anderson correlator and the long-range mutual information decay via a power-law with critical exponents that vary continuously along the marginal MBL line.

Bibliography

[1] L. Landau, *On the theory of phase transitions*, *Zh. Eksp. Teor. Fiz.* **7** (1937) 19–32.

[2] L. D. Landau and E. M. Lifshitz, *Statistical Physics, Third Edition, Part 1: Volume 5*. Butterworth-Heinemann, Oxford England, 3 edition ed., Jan., 1980.

[3] K. G. Wilson and J. Kogut, *The renormalization group and the expansion*, *Physics Reports* **12** (Aug., 1974) 75–199.

[4] C.-M. Jian, I. H. Kim, and X.-L. Qi, *Long-range mutual information and topological uncertainty principle*, *arXiv:1508.07006* (Aug., 2015).

[5] M. Hermele, M. P. A. Fisher, and L. Balents, *Pyrochlore photons: The $u(1)$ spin liquid in a $s = \frac{1}{2}$ three-dimensional frustrated magnet*, *Phys. Rev. B* **69** (Feb, 2004) 064404.

[6] A. Rasmussen, Y.-Z. You, and C. Xu, *Stable Gapless Bose Liquid Phases without any Symmetry*, *arXiv:1601.08235 [cond-mat]* (Jan., 2016) [arXiv:1601.0823].

[7] J. Kelly, R. Barends, A. G. Fowler, A. Megrant, E. Jeffrey, T. C. White, D. Sank, J. Y. Mutus, B. Campbell, Y. Chen, Z. Chen, B. Chiaro, A. Dunsworth, I.-C. Hoi, C. Neill, P. J. J. O'Malley, C. Quintana, P. Roushan, A. Vainsencher, J. Wenner, A. N. Cleland, and J. M. Martinis, *State preservation by repetitive error detection in a superconducting quantum circuit*, *Nature* **519** (Mar., 2015) 66–69.

[8] T. Senthil, A. Vishwanath, L. Balents, S. Sachdev, and M. P. A. Fisher, *Deconfined quantum critical points*, *Science* **303** (2003) 1490.

[9] T. Senthil, L. Balents, S. Sachdev, A. Vishwanath, and M. P. A. Fisher, *Quantum criticality beyond the* Landau-Ginzburg-Wilson *paradigm*, *Physical Review B* **70** (2004) 144407.

[10] A. W. Sandvik, *Evidence for deconfined quantum criticality in a two-dimensional heisenberg model with four-spin interactions*, *Phys. Rev. Lett.* **98** (Jun, 2007) 227202.

[11] R. G. Melko and R. K. Kaul, *Scaling in the fan of an unconventional quantum critical point*, *Phys. Rev. Lett.* **100** (Jan, 2008) 017203.

[12] C. Xu and S. Sachdev *Phys. Rev. B* **79** (2009) 064405.

[13] E.-G. Moon and C. Xu, *Exotic continuous quantum phase transition between F_2 topological spin liquid and néel order*, *Phys. Rev. B* **86** (Dec, 2012) 214414.

[14] Z. Zhu and S. R. White, *Spin liquid phase of the $s = \frac{1}{2}$ $J_1 - J_2$ heisenberg model on the triangular lattice*, *Phys. Rev. B* **92** (Jul, 2015) 041105.

[15] Z.-C. Gu and X.-G. Wen, *Tensor-entanglement-filtering renormalization approach and symmetry-protected topological order*, *Phys. Rev. B* **80** (Oct, 2009) 155131, [arXiv:0903.1069].

[16] D. V. Else and C. Nayak, *Classifying symmetry-protected topological phases through the anomalous action of the symmetry on the edge*, *Phys. Rev. B* **90** (Dec, 2014) 235137.

[17] X. Chen, Z.-C. Gu, Z.-X. Liu, and X.-G. Wen *arXiv:1106.4772* (2011).

[18] X. Chen, Z.-C. Gu, Z.-X. Liu, and X.-G. Wen *Science* **338** (2012) 1604.

[19] Y.-M. Lu and A. Vishwanath *Phys. Rev. B* **86** (2012) 125119.

[20] Z. Bi, A. Rasmussen, K. Slagle, and C. Xu, *Classification and description of bosonic symmetry protected topological phases with semiclassical nonlinear sigma models*, *Phys. Rev. B* **91** (Apr, 2015) 134404.

[21] A. Kapustin, *Bosonic Topological Insulators and Paramagnets: a view from cobordisms*, *arXiv:1404.6659 [cond-mat, physics:hep-th]* (Apr., 2014) [arXiv:1404.6659].

[22] C. Xu and A. W. W. Ludwig *arXiv:1112.5303* (2011).

[23] D. M. Basko, I. L. Aleiner, and B. L. Altshuler, *Metal insulator transition in a weakly interacting many-electron system with localized single-particle states*, *Annals of Physics* **321** (May, 2006) 1126–1205, [cond-mat/0506617].

[24] M. Srednicki, *Chaos and quantum thermalization*, *Phys. Rev. E* **50** (Aug, 1994) 888–901.

[25] R. Nandkishore and D. A. Huse, *Many-Body Localization and Thermalization in Quantum Statistical Mechanics*, *Annual Review of Condensed Matter Physics* **6** (Mar., 2015) 15–38, [arXiv:1404.0686].

[26] M. Serbyn, Z. Papić, and D. A. Abanin, *Universal Slow Growth of Entanglement in Interacting Strongly Disordered Systems*, *Physical Review Letters* **110** (June, 2013) 260601, [arXiv:1304.4605].

[27] J. H. Bardarson, F. Pollmann, and J. E. Moore, *Unbounded Growth of Entanglement in Models of Many-Body Localization*, *Physical Review Letters* **109** (July, 2012) 017202, [arXiv:1202.5532].

[28] M. Žnidarič, T. Prosen, and P. Prelovšek, *Many-body localization in the Heisenberg XXZ magnet in a random field*, *Phys. Rev. B* **77** (Feb., 2008) 064426, [arXiv:0706.2539].

[29] S. Yan, D. A. Huse, and S. R. White *Science* **332** (2011) 1173.

[30] H.-C. Jiang, H. Yao, and L. Balents *Phys. Rev. B* **86** (2012) 024424.

[31] H.-C. Jiang, Z. Wang, and L. Balents *Nature Physics* **8** (2012) 902.

[32] S. V. Isakov, M. B. Hastings, and R. G. Melko *Nature Physics* **7** (2011) 772.

[33] S. V. Isakov, M. B. Hastings, and R. G. Melko *Science* **335** (2012) 193.

[34] A. Kitaev and J. Preskill *Phys. Rev. Lett.* **96** (2006) 110404.

[35] M. Levin and X.-G. Wen *Phys. Rev. Lett.* **96** (2006) 110405.

[36] R. A. Jalabert and S. Sachdev *Phys. Rev. B* **44** (1991) 686.

[37] C. Xu and L. Balents *Phys. Rev. B* **84** (2011) 014402.

[38] Y. Huh, M. Punk, and S. Sachdev *Phys. Rev. B* **84** (2011) 094419.

[39] C. Xu *International Journal of Modern Physics B* **26** (2012) 1230007.

[40] R. Moessner, S. L. Sondhi, and P. Chandra *Phys. Rev. Lett.* **84** (2000) 4457.

[41] R. Moessner and S. L. Sondhi *Phys. Rev. B* **63** (2001) 224401.

[42] R. Moessner and S. L. Sondhi *Phys. Rev. Lett.* **86** (2001) 1881.

[43] G. Misguich and F. Mila *Phys. Rev. B* **77** (2008) 134421.

[44] C. M. Herdman and K. B. Whaley, *Loop condensation in the triangular lattice quantum dimer model*, *New Journal of Physics* **13** (2011), no. 8 085001.

[45] Y. Shimizu, K. Miyagawa, K. Kanoda, M. Maesato, and G. Saito, *Spin liquid state in an organic* Mott *insulator with a triangular lattice*, *Physical Review Letter* **91** (2003) 107001.

[46] Y. Shimizu, K. Miyagawa, K. Kanoda, M. Maesato, and G. Saito, *Emergence of inhomogeneous moments from spin liquid in the triangular-lattice mott insulator* κ-$(ET)_2Cu_2(CN)_3$, *Physical Review B* **73** (2006) 140407(R).

[47] S. Yamashita, Y. Nakazawa, M. Oguni, Y. Oshima, H. Nojiri, Y. Shimizu, K. Miyagawa, and K. Kanoda, *Thermodynamic properties of a spin-1/2 spin-liquid state in a κ-type organic salt*, *Nature Physics* **4** (2008) 459.

[48] M. Yamashita, N. Nakata, Y. Kasahara, T. Sasaki, N. Yoneyama, N. Kobayashi, S. Fujimoto, T. Shibauchi, and Y. Matsuda, *Thermal-transport measurements in a quantum spin-liquid state of the frustrated triangular magnet* κ-$(ET)_2Cu_2(CN)_3$, *Nature Physics* **5** (2009) 44.

[49] F. L. Pratt, P. J. Baker, S. J. Blundell, T. Lancaster, S. Ohira-Kawamura3, C. Baines, Y. Shimizu, K. Kanoda, I. Watanabe, and G. Saito, *Magnetic and non-magnetic phases of a quantum spin liquid*, *Nature* **471** (2010) 612.

[50] T. Itou, A. Oyamada, S. Maegawa, M. Tamura, and R. Kato, ^{13}C NMR *study of the spin-liquid state in the triangular quantum antiferromagnet* $EtMe_3Sb[Pd(dmit)_2]_2$, *Journal of Physics: Conference Series* **145** (2009) 012039.

[51] T. Itou, A. Oyamada, S. Maegawa, M. Tamura, and R. Kato, *Quantum spin liquid in the spin-1/2 triangular antiferromagnet* $EtMe_3Sb[Pd(dmit)_2]_2$, *Physical Review B* **77** (2008) 104413.

[52] Y. Shimizu, H. Akimoto, H. Tsujii, A. Tajima, and R. Kato, *Reentrant* Mott *transition from a* Fermi *liquid to a spin-gapped insulator in an organic spin-1/2 triangular-lattice antiferromagnet*, *Journal of Physics: Condensed Matter* **19** (2007) 145240.

[53] S. Yamashita, T. Yamamoto, Y. Nakazawa, M. Tamura, and R. Kato, *Gapless spin liquid of an organic triangular compound evidenced by thermodynamic measurements*, *Nature Communications* **2** (2011) 275.

[54] M. Yamashita, N. Nakata, Y. Senshu, M. Nagata, H. M. Yamamoto, R. Kato, T. Shibauchi, and Y. Matsuda, *Highly mobile gapless excitations in a two-dimensional candidate quantum spin liquid*, *Science* **328** (2010) 1246.

[55] R. Kato, A. Tajima, A. Nakao, and M. Tamura *J. Am. Chem. Soc.* **128** (2006) 10016.

[56] C. de la Cruz, Q. Huang, J. W. Lynn, J. Li, W. R. Ii, J. L. Zarestky, H. A. Mook, G. F. Chen, J. L. Luo, N. L. Wang, and P. Dai, *Magnetic order close to superconductivity in the iron-based layered LaO1-xFxFeAs systems*, *Nature* **453** (June, 2008) 899–902.

[57] C. Fang, H. Yao, W.-F. Tsai, J. Hu, and S. A. Kivelson, *Theory of electron nematic order in lafeaso*, *Phys. Rev. B* **77** (Jun, 2008) 224509.

[58] C. Xu, M. Müller, and S. Sachdev, *Ising and spin orders in the iron-based superconductors*, *Phys. Rev. B* **78** (Jul, 2008) 020501.

[59] Y. Qi and C. Xu, *Global phase diagram for magnetism and lattice distortion of fe-pnictide materials*, *Phys. Rev. B* **80** (2009) 094402.

[60] C. Xu and J. Hu *arXiv:0903.4477* (2006).

[61] F. Wang and A. Vishwanath *Phys. Rev. B* **74** (2006) 174423.

[62] X.-G. Wen *Phys. Rev. B* **65** (2002) 165113.

[63] R. Coldea, D. A. Tennant, A. M. Tsvelik, and Z. Tylczynski *Phys. Rev. Lett.* **86** (2001) 1335.

[64] R. Coldea, D. A. Tennant, and Z. Tylczynski *Phys. Rev. B* **68** (2003) 134424.

[65] J. M. Carmona, A. Pelissetto, and E. Vicari *Phys. Rev. B* **61** (2000) 15136.

[66] J. Lou, A. W. Sandvik, and L. Balents *Phys. Rev. Lett.* **99** (2007) 207203.

[67] K. Slagle and C. Xu, *Quantum phase transition between the Z_2 spin liquid and valence bond crystals on a triangular lattice*, *Phys. Rev. B* **89** (Mar, 2014) 104418.

[68] L. Fidkowski and A. Kitaev *Phys. Rev. B* **81** (2010) 134509.

[69] L. Fidkowski and A. Kitaev *Phys. Rev. B* **83** (2011) 075103.

[70] X.-L. Qi *New J. Phys.* **15** (2013) 065002.

[71] H. Yao and S. Ryu *Phys. Rev. B* **88** (2013) 064507.

[72] Z.-C. Gu and M. Levin, *Effect of interactions on two-dimensional fermionic symmetry-protected topological phases with z2 symmetry*, *Phys. Rev. B* **89** (May, 2014) 201113(R).

[73] S. Ryu and S.-C. Zhang *Phys. Rev. B* **85** (2012) 245132.

[74] C. Wang and T. Senthil, *Interacting fermionic topological insulators/superconductors in three dimensions*, *Phys. Rev. B* **89** (May, 2014) 195124.

[75] L. Fidkowski, X. Chen, and A. Vishwanath *Phys. Rev. X* **3** (2013) 041016.

[76] Y.-Z. You and C. Xu *arXiv:1409.0168* (2014).

[77] A. P. Schnyder, S. Ryu, A. Furusaki, and A. W. W. Ludwig *AIP Conf. Proc.* **1134** (2009) 10.

[78] S. Ryu, A. Schnyder, A. Furusaki, and A. Ludwig *New J. Phys.* **12** (2010) 065010.

[79] K. A. Yu *AIP Conf. Proc* **1134** (2009) 22.

[80] D. J. Gross and A. Neveu *Phys. Rev. D* **10** (1974) 3235.

[81] C. L. Kane and E. J. Mele, *Quantum spin hall effect in graphene*, *Physical Review Letter* **95** (2005) 226801.

[82] A. J. Heeger, S. Kivelson, J. R. Schrieffer, and W. P. Su, *Solitons in conducting polymers*, *Rev. Mod. Phys.* **60** (Jul, 1988) 781–850.

[83] F. F. Assaad, *Phase diagram of the half-filled two-dimensional SU(N) Hubbard-Heisenberg model: A quantum Monte Carlo study*, *Phys. Rev. B* **71** (Feb., 2005) 075103, [cond-mat/0406074].

[84] V. Ayyar and S. Chandrasekharan *arXiv:1410.6474* (2014).

[85] T. Yoshida, R. Peters, S. Fujimoto, and N. Kawakami, *Characterization of a topological mott insulator in one dimension*, *Phys. Rev. Lett.* **112** (May, 2014) 196404.

[86] A. G. Abanov and P. B. Wiegmann *Nucl. Phys. B* **570** (2000) 685.

[87] H. Levine, S. B. Libby, and A. M. M. Pruisken *Phys. Rev. Lett.* **51** (1983) 1915.

[88] H. Levine, S. B. Libby, and A. M. M. Pruisken *Nucl. Phys. B* **240** (1984) 30, 49, 71.

[89] A. M. M. Pruisken, M. A. Baranov, and M. Voropaev *arXiv:cond-mat/0101003* (2001).

[90] Z. Bi, A. Rasmussen, and C. Xu *arXiv:1309.0515* (2013).

[91] Y. Ran, A. Vishwanath, and D.-H. Lee *Phys. Rev. Lett.* **101** (2008) 086801.

[92] X.-L. Qi and S.-C. Zhang *Phys. Rev. Lett.* **101** (2008) 086802.

[93] D. J. Thouless, M. Kohmoto, M. P. Nightingale, and M. den Nijs *Phys. Rev. Lett.* **49** (1982) 405.

[94] Q. Niu, D. J. Thouless, and Y. S. Wu *Phys. Rev. B* **31** (1985) 3372.

[95] K. Ishikawa and T. Matsuyama *Z. Phys. C.* **33** (1986) 41.

[96] G. E. Volovik, *The Universe in a Helium Droplet.* Clarendon Press, 2003.

[97] Z. Wang, X.-L. Qi, and S.-C. Zhang *Phys. Rev. Lett.* **105** (2010) 256803.

[98] Z. Wang, X.-L. Qi, and S.-C. Zhang *Phys. Rev. B* **85** (2012) 165126.

[99] Z. Wang and S.-C. Zhang *Phys. Rev. X* **2** (2012) 031008.

[100] Z. Wang and S.-C. Zhang *Phys. Rev. B* **86** (2012) 165116.

[101] Y.-Z. You, Z. Wang, J. Oon, and C. Xu, *Topological number and fermion Green's function for strongly interacting topological superconductors*, *Phys. Rev. B* **90** (Aug., 2014) 060502, [arXiv:1403.4938].

[102] K. Slagle, Y.-Z. You, and C. Xu, *Exotic quantum phase transitions of strongly interacting topological insulators*, *Phys. Rev. B* **91** (Mar, 2015) 115121.

[103] F. Assaad and H. Evertz, *World-line and Determinantal Quantum Monte Carlo Methods for Spins, Phonons and Electrons*, vol. 739 of *Lecture Notes in Physics*. Springer Berlin Heidelberg, 2008.

[104] M. Hohenadler, Z. Y. Meng, T. C. Lang, S. Wessel, A. Muramatsu, and F. F. Assaad, *Quantum phase transitions in the Kane-Mele-Hubbard model*, *Phys. Rev. B* **85** (Mar., 2012) 115132, [arXiv:1111.3949].

[105] Z. Y. Meng, T. C. Lang, S. Wessel, F. F. Assaad, and A. Muramatsu, *Quantum spin liquid emerging in two-dimensional correlated Dirac fermions*, *Nature* **464** (Apr., 2010) 847–851, [arXiv:1003.5809].

[106] B. Bauer and C. Nayak, *Area laws in a many-body localized state and its implications for topological order*, *Journal of Statistical Mechanics: Theory and Experiment* **9** (Sept., 2013) 5, [arXiv:1306.5753].

[107] P. Anderson *Phys. Rev.* **109** (1958) 1492.

[108] D. Basko, I. Aleiner, and B. Altshuler *Annals of Physics* **321** (2006) 1126.

[109] I. V. Gornyi, A. D. Mirlin, and D. G. Polyakov *Phys. Rev. Lett.* **95** (2005) 206603.

[110] D. A. Huse, R. Nandkishore, V. Oganesyan, A. Pal, and S. L. Sondhi *Phys. Rev. B* **88** (2013) 014206.

[111] A. Chandran, V. Khemani, C. R. Laumann, and S. L. Sondhi *Phys. Rev. B* **89** (2014) 144201.

[112] Y. Bahri, R. Vosk, E. Altman, and A. Vishwanath *arXiv:1307.4092* (2013).

[113] S. K. Ma, C. Dasgupta, and C. K. Hu *Phys. Rev. Lett.* **43** (1979) 1434.

[114] C. Dasgupta and S. K. Ma *Phys. Rev. B* **22** (1980) 1305.

[115] D. S. Fisher *Phys. Rev. B* **50** (1994) 3799.

[116] D. S. Fisher *Phys. Rev. B* **51** (1995) 6411.

[117] G. Refael and J. E. Moore *Phys. Rev. Lett.* **93** (2004) 260602.

[118] R. Vasseur, A. C. Potter, and S. A. Parameswaran *Phys. Rev. Lett.* **114** (2015) 217201.

[119] R. Vosk and E. Altman, *Many-Body Localization in One Dimension as a Dynamical Renormalization Group Fixed Point*, *Physical Review Letters* **110** (Feb., 2013) 067204, [arXiv:1205.0026].

[120] D. Pekker, G. Refael, E. Altman, E. Demler, and V. Oganesyan, *Hilbert-Glass Transition: New Universality of Temperature-Tuned Many-Body Dynamical Quantum Criticality*, *Physical Review X* **4** (Jan., 2014) 011052, [arXiv:1307.3253].

[121] A. M. Turner, Y. Zhang, and A. Vishwanath *Phys. Rev. B* **82** (2010) 241102R.

[122] R. Nandkishore and A. C. Potter *Phys. Rev. B* **90** (2014) 195115.

[123] Y. Bar Lev, G. Cohen, and D. R. Reichman, *Absence of diffusion in an interacting system of spinless fermions on a one-dimensional disordered lattice*, *Phys. Rev. Lett.* **114** (Mar, 2015) 100601.

[124] V. P. Michal, I. L. Aleiner, B. L. Altshuler, and G. V. Shlyapnikov, *Finite-Temperature Fluid-Insulator Transition of Strongly Interacting 1D Disordered Bosons*, *ArXiv e-prints* (Feb., 2015) [arXiv:1502.0028].

[125] M. Schreiber, S. S. Hodgman, P. Bordia, H. P. Lüschen, M. H. Fischer, R. Vosk, E. Altman, U. Schneider, and I. Bloch, *Observation of many-body localization of interacting fermions in a quasi-random optical lattice*, *ArXiv e-prints* (Jan., 2015) [arXiv:1501.0566].

[126] Y.-Z. You and C. Xu *In progress* (2015).

[127] M. Levin and Z.-C. Gu *Phys. Rev. B* **86** (2012) 115109.

[128] X. Chen, Z.-X. Liu, and X.-G. Wen *Phys. Rev. B* **84** (2011) 235141.

[129] F. J. Burnell, X. Chen, L. Fidkowski, and A. Vishwanath *arXiv:1302.7072* (2013).

[130] M. Serbyn, Z. Papić, and D. A. Abanin *Phys. Rev. Lett.* **111** (2013) 127201.

[131] F. D. M. Haldane *Phys. Lett. A* **93** (1983) 464.

[132] F. D. M. Haldane *Phys. Rev. Lett.* **50** (1983) 1153.

[133] B. I. Halperin *Phys. Rev. B* **25** (1982) 2185.

[134] M. Onoda, Y. Avishai, and N. Nagaosa *Phys. Rev. Lett.* **98** (2007) 076802.

[135] A. A. Soluyanov and D. Vanderbilt *Phys. Rev. B* **83** (2011) 035108.

[136] Z. Bi, A. Rasmussen, Y.-Z. You, M. Cheng, and C. Xu *arXiv:1404.6256* (2014).

[137] K. Slagle, Z. Bi, Y.-Z. You, and C. Xu, *Many-Body Localization of Symmetry Protected Topological States*, *arXiv:1505.05147 [cond-mat]* (May, 2015).

[138] Y.-Z. You, X.-L. Qi, and C. Xu, *Entanglement Holographic Mapping of Many-Body Localized System by Spectrum Bifurcation Renormalization Group*, *ArXiv e-prints* (Aug., 2015) [arXiv:1508.0363].

[139] S. Sachdev, *Quantum Phase Transitions*. Cambridge University Press, 2 ed., May, 2011.

[140] J. M. Deutsch, *Quantum statistical mechanics in a closed system*, *Phys. Rev. A* **43** (Feb, 1991) 2046–2049.

[141] M. Rigol, V. Dunjko, and M. Olshanii, *Thermalization and its mechanism for generic isolated quantum systems*, *Nature* **452** (Apr., 2008) 854–858, [arXiv:0708.1324].

[142] I. V. Gornyi, A. D. Mirlin, and D. G. Polyakov, *Interacting Electrons in Disordered Wires: Anderson Localization and Low-T Transport*, *Physical Review Letters* **95** (Nov., 2005) 206603, [cond-mat/0506411].

[143] V. Oganesyan and D. A. Huse, *Localization of interacting fermions at high temperature*, *Phys. Rev. B* **75** (Apr., 2007) 155111, [cond-mat/0610854].

[144] J. Z. Imbrie, *On Many-Body Localization for Quantum Spin Chains*, *ArXiv e-prints* (Mar., 2014) [arXiv:1403.7837].

[145] G. Refael and E. Altman, *Strong disorder renormalization group primer and the superfluid-insulator transition*, *Comptes Rendus Physique* **14** (Oct., 2013) 725–739, [arXiv:1402.6008].

[146] D. A. Huse, R. Nandkishore, V. Oganesyan, A. Pal, and S. L. Sondhi, *Localization-protected quantum order*, *Phys. Rev. B* **88** (July, 2013) 014206, [arXiv:1304.1158].

[147] D. Pekker, G. Refael, E. Altman, E. Demler, and V. Oganesyan, *Hilbert-Glass Transition: New Universality of Temperature-Tuned Many-Body Dynamical Quantum Criticality*, *Physical Review X* **4** (Jan., 2014) 011052, [arXiv:1307.3253].

[148] A. Chandran, V. Khemani, C. R. Laumann, and S. L. Sondhi, *Many-body localization and symmetry-protected topological order*, *Phys. Rev. B* **89** (Apr., 2014) 144201, [arXiv:1310.1096].

[149] R. Vasseur, A. C. Potter, and S. A. Parameswaran, *Quantum Criticality of Hot Random Spin Chains*, *Physical Review Letters* **114** (May, 2015) 217201, [arXiv:1410.6165].

[150] K. Slagle, Z. Bi, Y.-Z. You, and C. Xu, *Many-Body Localization of Symmetry Protected Topological States*, *ArXiv e-prints* (May, 2015) [arXiv:1505.0514].

[151] R. Nandkishore and A. C. Potter, *Marginal Anderson localization and many-body delocalization*, *Phys. Rev. B* **90** (Nov., 2014) 195115, [arXiv:1406.0847].

[152] R. Vasseur, A. C. Potter, and S. A. Parameswaran, *Quantum Criticality of Hot Random Spin Chains*, *Physical Review Letters* **114** (May, 2015) 217201, [arXiv:1410.6165].

[153] A. Chandran, I. H. Kim, G. Vidal, and D. A. Abanin, *Constructing local integrals of motion in the many-body localized phase*, *Phys. Rev. B* **91** (Feb., 2015) 085425, [arXiv:1407.8480].

[154] I. H. Kim, A. Chandran, and D. A. Abanin, *Local integrals of motion and the logarithmic lightcone in many-body localized systems*, *ArXiv e-prints* (Dec., 2014) [arXiv:1412.3073].

[155] V. Ros, M. Müller, and A. Scardicchio, *Integrals of motion in the many-body localized phase*, *Nuclear Physics B* **891** (Feb., 2015) 420–465, [arXiv:1406.2175].

[156] R. Vosk and E. Altman, *Many-Body Localization in One Dimension as a Dynamical Renormalization Group Fixed Point*, *Physical Review Letters* **110** (Feb., 2013) 067204, [arXiv:1205.0026].

[157] M. Serbyn, Z. Papić, and D. A. Abanin, *Local Conservation Laws and the Structure of the Many-Body Localized States*, *Physical Review Letters* **111** (Sept., 2013) 127201, [arXiv:1305.5554].

[158] D. A. Huse, R. Nandkishore, and V. Oganesyan, *Phenomenology of fully many-body-localized systems*, *Phys. Rev. B* **90** (Nov., 2014) 174202, [arXiv:1305.4915].

[159] C. Dasgupta and S.-k. Ma, *Low-temperature properties of the random heisenberg antiferromagnetic chain*, *Phys. Rev. B* **22** (Aug, 1980) 1305–1319.

[160] R. N. Bhatt and P. A. Lee, *Scaling studies of highly disordered spin-$\frac{1}{2}$ antiferromagnetic systems*, *Phys. Rev. Lett.* **48** (Feb, 1982) 344–347.

[161] D. S. Fisher, *Random transverse field ising spin chains*, *Phys. Rev. Lett.* **69** (Jul, 1992) 534–537.

[162] D. S. Fisher, *Random antiferromagnetic quantum spin chains*, *Phys. Rev. B* **50** (Aug, 1994) 3799–3821.

[163] D. S. Fisher, *Critical behavior of random transverse-field ising spin chains*, *Phys. Rev. B* **51** (Mar, 1995) 6411–6461.

[164] R. Vasseur, A. J. Friedman, S. A. Parameswaran, and A. C. Potter, *Particle-hole symmetry, many-body localization, and topological edge modes*, *ArXiv e-prints* (Oct., 2015) [arXiv:1510.0428].

[165] A. C. Potter, T. Morimoto, and A. Vishwanath, *Topological classification of interacting 1D Floquet phases*, *arXiv:1602.05194 [cond-mat]* (Feb., 2016).

[166] Error bars denote 1 standard deviation errors. All error estimates include the statistical error due to a finite number of disorder samples. Critical exponent error estimates also include an estimate of the error due to finite system sizes.

[167] S. Gopalakrishnan, M. Mueller, V. Khemani, M. Knap, E. Demler, and D. A. Huse, *Low-frequency conductivity in many-body localized systems*, *ArXiv e-prints* (Feb., 2015) [arXiv:1502.0771].

[168] D. Fattal, T. S. Cubitt, Y. Yamamoto, S. Bravyi, and I. L. Chuang, *Entanglement in the stabilizer formalism*, *eprint arXiv:quant-ph/0406168* (June, 2004) [quant-ph/0406168].

[169] G. Refael and J. E. Moore, *Entanglement Entropy of Random Quantum Critical Points in One Dimension*, *Physical Review Letters* **93** (Dec., 2004) 260602, [cond-mat/0406737].

[170] K. Slagle, Y.-Z. You, and C. Xu, *Disordered XYZ Spin Chain Simulations using the Spectrum Bifurcation Renormalization Group*, *arXiv:1604.04283 [cond-mat]* (Apr., 2016).

[171] K. Slagle, "SBRG." `https://github.com/kjslag/SBRG`, 2016.